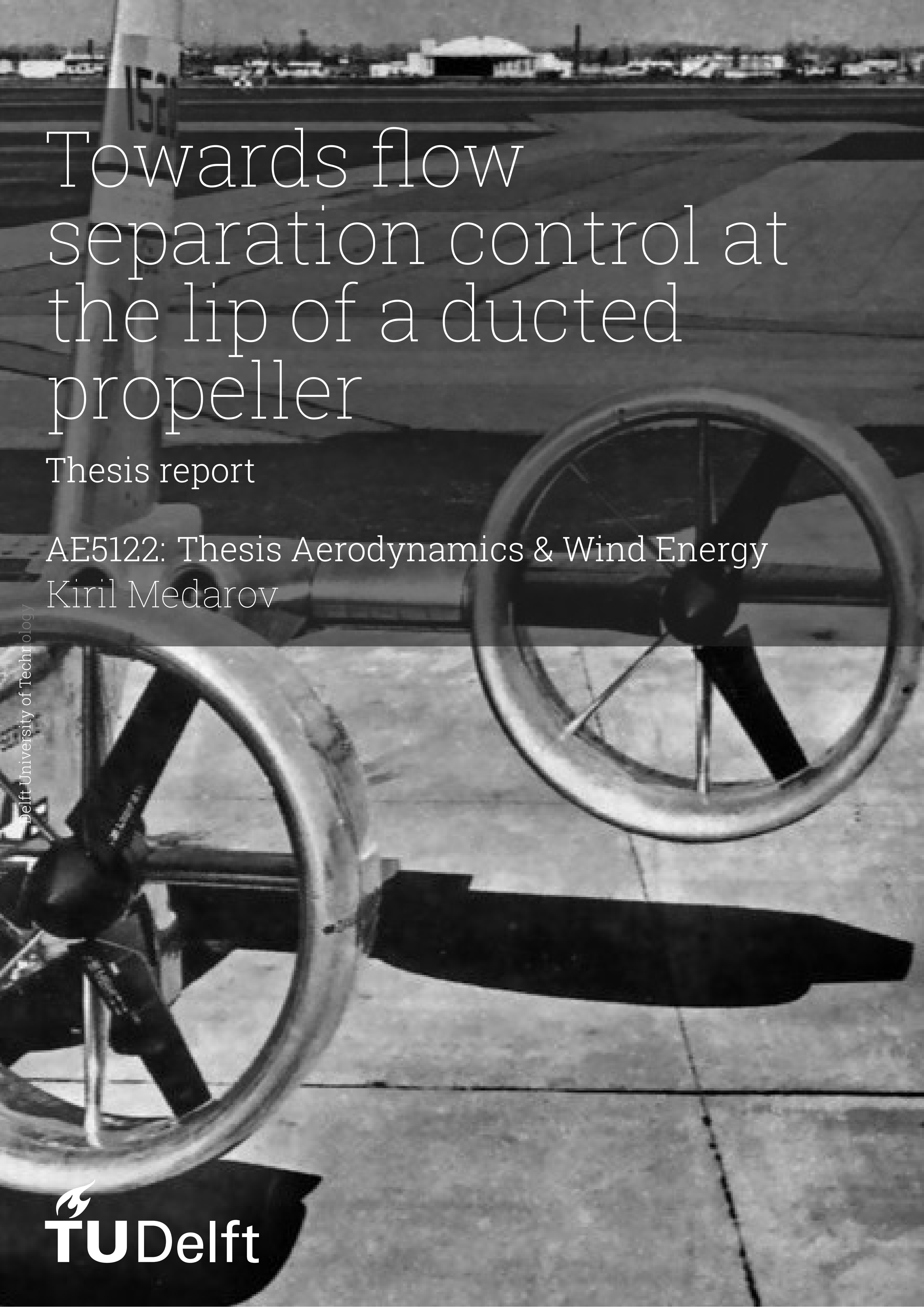

Towards flow separation control at the lip of a ducted propeller

Thesis report

AE5122: Thesis Aerodynamics & Wind Energy

Kiril Medarov

Delft University of Technology

Towards flow separation control at the lip of a ducted propeller

Thesis report

by

Kiril Medarov

Student Name	Student Number
Kiril Medarov	5633338

Thesis committee:	Prof.dr.ir. L.L.M. Veldhuis,	Thesis supervisor
	Prof.dr.ing. Georg Eitelberg,	Chair
	Dr. L. T. Lima Pereira,	Examiner
Project duration:	December, 2024 - September, 2025	
Faculty:	Faculty of Aerospace Engineering, Delft	

Cover: ”1966 ... Bell VTOL X-22” by James Vaughan [1], under CC BY-NC-SA 2.0 (Modified).

TU Delft

Preface

This thesis project represents the final stage of my MSc Aerospace Engineering study in TU Delft. It allowed me to solidify and extend my knowledge and skills in aerodynamic analysis as it involved numerical and experimental work relevant to flight performance optimization, which is an area which truly sparks my interest.

I would like to thank my supervisor Prof.dr.ir. L.L.M. Veldhuis for his support and guidance throughout the project. Additionally, I am thankful to the PhD candidate Aaron Sequeira who provided me with crucial assistance in performing the wind-tunnel tests involving 2D PIV visualization technique and propeller drive setup. Thanks should also go to everyone who provided their assistance for the intended wind-tunnel test setup to be realizable.

I would like to thank my family for the ultimate support throughout my studies from day one as well as my friends and colleagues that I met here who made this journey even more enjoyable and memorable.

Kiril Medarov
Delft, September 2025

Contents

List of Figures

List of Tables

Nomenclature

Abbreviations

Abbreviation	Definition
2D	Two-dimensional
3D	Three-dimensional
AoA	Angle of attack
AoB	Angle of blowing
BEM	Blade Element Momentum
CFD	Computational Fluid Dynamics
DUUC	Delft University Unconventional Configuration
NACA	National Advisory Committee for Aeronautics
PIV	Particle Image Velocimetry
RANS	Reynolds-Averaged Navier-Stokes
ROI	Region of interest
SST	Shear Stress Transport
S-A	Spalart-Allmaras
URANS	Unsteady Reynolds-Averaged Navier-Stokes
VTOL	Vertical Take-Off and Landing

Symbols

Symbol	Definition	Unit
A	Area	[m^2]
B	Number of blades	[-]
δ_{tip}	Tip clearance	[mm]
c	Chord length	[m]
C_f	Skin friction coefficient	[-]
C_t	Propeller coefficient of thrust	[-]
C_p	Propeller coefficient of power	[-]
C_L	Coefficient of lift	[-]
C_D	Coefficient of drag	[-]
C_μ	Blowing coefficient	[-]
D	Propeller diameter	[m]
η	Propeller efficiency	[-]
ϵ_d	Expansion ratio	[-]
J	Advance ratio	[-]
$\dot{m}$	Mass-flow	[kg/s]
μ	Dynamic viscosity	[kg/m·s]
n	Propeller rotational speed	[RPS]
o	Polynomial order	[-]
P	Propeller power	[W]
p_s	Static pressure	[Pa]
p_t	Total pressure	[Pa]
q	Dynamic pressure	[Pa]
ρ	Air density	[kg/m^3]
r	Radial coordinate	[m]
r	Power coefficient ratio	[-]
dr	Blade element thickness	[m]

Symbol	Definition	Unit
R	Propeller radius	[m]
Re	Reynolds number	[-]
S	Reference area	[m^2]
S	Sutherland constant	[K]
T	Propeller thrust	[N]
T	Static temperature	[K]
τ_w	Wall shear stress	[Pa]
v_∞	Freestream velocity	[m/s]
v_t	Tangential velocity	[m/s]
w	Filter width	[-]
w	Blowing slot width	[mm]
x/c	Non-dimensional chordwise position	[-]
y^+	Non-dimensional cell height	[-]

Summary

This document is a technical report of a master thesis project relevant to flight performance optimization strategy. The project is titled as ”Towards flow separation control at the lip of a ducted propeller”. The project might be applicable to both ducted propeller or propeller over-the-wing configuration under high angle of attack. Flow separation occurs due to strong adverse pressure gradients caused by the viscous interaction between a moving fluid and the surface of a body immersed in the flow. The larger the separation region is, the larger the pressure drag on the body. The goal of the project is to investigate the effectiveness of a near-wall blowing jet method to reduce, or even completely prevent, the flow separation region at the lip of a ducted propeller. The blowing jet is investigated based on an active and passive air supply approach. The analysis has been performed on a rotating propeller in close proximity to a uniform cross-section wing model. The propeller-wing configuration is designed such that the closest proximity is achieved at the mid-span of the wing. This choice is made to minimize the 3D-effects of the flow such as wingtip vortices and boundary layer influence developing on the mounting parts and the wind-tunnel walls. Hence, the representation of a ducted propeller condition is approximated only at the mid-span of the wing.

The propeller performance has been estimated by Blade Element Momentum theory (BEM) analysis. As the proximity of the propeller tip to the wing surface suppresses the blade tip vortices, and hence, increases the loading of the propeller towards the tip, the Prandtl tip loss correction is ignored to obtain the resulting pressure jump. Numerical simulations are then performed to estimate the separation point at different angles of attack. The computational domain approximates the intended experimental setup to validate the results. The freestream velocity has been selected to be 20 m/s, while the advance ratio of propeller is set to be 1.4. Compared were the results of the SST $k-\omega$ and Spalart-Allmaras turbulent models.

Experimental validation of the results has been performed in the SLT wind-tunnel facility of the Low-Speed Laboratory of TU Delft. The effectiveness of the blowing jet has been analyzed in terms of the blowing coefficient which is a measure of the momentum of the blown air. The influence of the blowing coefficient on the flow field has been evaluated while the propeller is active and inactive at freestream velocity of 10 and 20 m/s. Total pressure probe readings and tufts flow visualization were considered for estimation the resulting velocity development under various blowing coefficients. Additionally, the flow field has been experimentally quantitatively visualized by using planar Particle Image Velocimetry (PIV) technique showing the impact on the blowing coefficient on the velocity field region upstream the propeller.

The results of the project match with found literature that the low-blowing coefficient increases the separation region, rather than suppressing it. The exact mechanism description behind this is still unknown to the found literature, but it is suggested that the addition of low air momentum near the wall reduces the boundary layer’s momentum, inducing thickness growth and destabilization of the boundary layer, making it more susceptible to earlier separation. Based on the obtained data, the threshold where the blowing switches from detrimental to beneficial for flow separation is found to decrease with decreasing either the angle of attack or the freestream velocity. This is suggested to occur as the adverse pressure gradient over the lip under these conditions is weakened, reducing the momentum required from the blown jet to suppress flow separation. The passive air supply of the blowing jet was attempted to be provided by a flow channel collecting mass-flow downstream of the propeller and recirculating it back to the blowing slot. However, the designed channel showed no capability of flow separation suppression, indicating that the inflow velocity is highly disturbed by the flow development at the inlet location. Hence, no effective solution for a passive flow control could be found.

Several recommendations are provided aiming for increasing the accuracy of future research. They concern both the numerical and experimental approach in this project, along with the propeller performance estimation.

1

Introduction

This document serves a technical report of a master thesis project of the MSc Aerospace Engineering program in TU Delft. The project represents a research focusing on analysis of the effectiveness of a flow control method for mitigation of the aerodynamic disadvantages due to occurrence of flow separation region at the lip of a ducted propeller. Such disadvantages are reduction of thrust, increase of the required power and noise during the operation of the propeller. More specifically, the flow control method is applying a blowing jet near the surface of the duct's lip such that the flow separation point is pushed downstream, benefiting the ducted propeller's performance at high angles of attack in forward flight. Figure 1.1 shows a numerical study of the potential of the blowing jet method for flow separation region size mitigation.

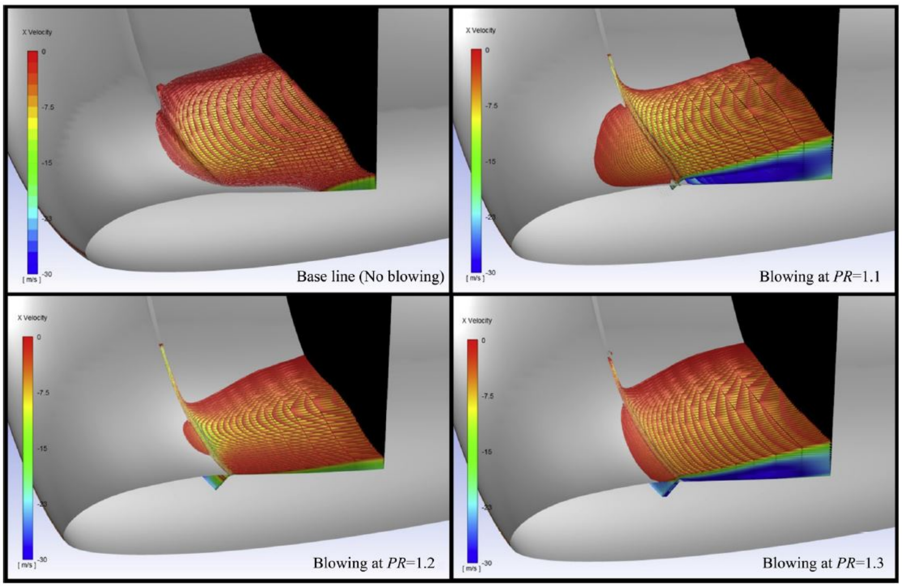

Figure 1.1: Visualization of a flow separation size mitigation at the lip of a ducted propeller using blowing jet. The figure compares the unblown with active control cases, indicating the potential of the method to suppress flow separation [2]

The research outcome in this project is based on performed literature survey, numerical- and experimental analysis on the flow behavior affected by the application of blowing jet near the duct's surface at a selected freestream velocity and propeller operational setting. A limitation of the research is that the flow analysis is based solely on a planar flow domain between a straight wing and an isolated propeller, preventing an accurate recreation of a ducted propeller geometry and hence, accounting for the 3D flow characteristics. Therefore, the title of the project is formulated as "Towards flow separation control at the lip of a ducted propeller". The project findings can be not only relevant to flow behavior studies in a ducted propeller, but also over-the-wing propeller configuration involving flow control such as near-wall blowing jet.

The conducted literature survey is based on academic research papers related to flow control by employing a blowing jet. The objective is to obtain synthesized information for answering the sub-research questions, contributing to finding the answer of the main research question of the project. The design of the blowing jet is selected to maximize the use of Coanda effect allowing for minimizing the deterioration of the aerodynamic characteristics of the duct's surface when the blowing slot is not active. The propeller performance is then estimated based on Blade Element Momentum Theory (BEM) analysis allowing for first-order accurate prediction of the pressure jump at the propeller plane. The numerical analysis involves performing Computational Fluid Dynamics (CFD) simulations with the purpose of approximation of the flow development at a close similarity to the experimental setup conditions. The propeller is modeled as an actuator line, while the duct is represented by its airfoil cross-section. The flow behavior is validated experimentally by flow visualization at the minimum tip clearance region between the wing and propeller using 2D Particle Image Velocimetry (PIV) technology, tufts, and total pressure probe readings. The analysis is based on several blowing velocities, resulting from variation of the blowing coefficients and the width of the blowing jet.

1.1. Research definition

The conducted research is defined in several points. They are as follows:

1.1.1. Research problem

The problem which this research project is dedicated to investigate is related to the flow control at the lip of a ducted propeller. More specifically, the increase of the angle of attack causes high suction peaks at the lip of the duct leading to flow separation, disturbing the flow in the duct. The affected flow has several performance deterioration effects such as reduced thrust and increase in power required for the engine to perform a required operational task. Hence, maximizing the performance of the ducted propeller especially at high angle of attack, would benefit from minimizing flow separation at the lip.

1.1.2. Research scope

The research scope involves the investigation of flow behavior around the flow separation point at the lip of a duct's geometry by applying a near-wall-blowing jet method. The analysis is based on a 2D planar approximation of the airflow. The plane of investigation is defined by the propeller rotational axis and the point of minimum tip clearance with the propeller. The project scope involves 2D numerical and experimental analysis of the airflow. The numerical simulations do not consider the unsteady flow behavior, but the averaged steady-state condition. The project is limited to purely aerodynamic analysis between the wing shape and the propeller without other considerations such as power consumption, structural effects, noise or others. The analyzed geometries are selected with the goal of demonstration of a general phenomenon valid for different designs, instead of focusing on a specific duct and propeller.

1.1.3. Research objectives

The main research objective of this project is to explore the capabilities of improving the aerodynamic characteristics of a duct surface at a high angles of attack by a near-wall blowing jet method for flow separation prevention at the lip of a ducted propeller. This method is expected to push the flow separation point downstream compared to the unblown case, increasing the attached flow area over the lip of the duct. This is expected to be beneficial for enhancing the flow control at high angles of attack, resulting in a better propeller performance. The focus is to analyze the blowing jet near the wall of the duct's lip such that the adverse pressure gradients causing flow separation at high angles of attack are mitigated, postponed to a higher angle of attack or even completely prevented. Moreover, this project aims at gaining understanding through analysis of numerical and experimental results, comparing the observed results with literature findings, and drawing conclusions on the feasibility of non-powered flow control for separation region reduction.

1.1.4. Research questions

Considering the main objective of this project, the main research question is formulated as follows:

How effective is a near-wall blowing jet method for preventing flow separation at the lip of a ducted propeller?

Provided below is a list of formulated sub-research questions. Their role is to break down the main research question into several smaller research topics which contribute to finding an answer for more general and fundamental aspects of the main research question.

- How is the ducted propeller performance affected by the duct's geometry?
- How is the propeller's advance ratio affecting the performance of the duct?
- How does the tip clearance affect the propeller loading?
- How should the flow control performance be experimentally analyzed?
- How is the range of angle of attack of interest limited?
- How can the separation point be reasonably approximated?
- What is the blowing coefficient's influence on the flow separation with variation of the angle of attack and freestream velocity?
- How should a passive flow control method such as a flow channel be implemented to contribute to separation prevention at the lip for the entire investigated range of angle of attack?

The report begins with theoretical background regarding ducted propellers and blowing jet principle. Then, the propeller geometry and performance estimation procedure is discussed, followed by the methodology and results from the conducted numerical analysis on the propeller-wing configuration in the represented experimental setup. Consequently, the experimental analysis procedure is described differentiating between presence- and no presence of the propeller effect. Finally, conclusions are drawn based on the obtained results, followed by recommendations for future research.

2

Theoretical background

2.1. Propeller aerodynamics

A propeller is a complex aerodynamic system with the purpose of addition of momentum to the freestream flow and hence, generating thrust force. The common description of a propeller is that of rotating wings, called blades, mounted on a central hub. The flow field behind a spinning propeller is typically characterized by increased dynamic pressure and a swirl component due to the added rotational kinetic energy to the fluid by the rotating blades. This is illustrated in Figure 2.1 showing a representation of the propeller as an advancing rotating wing producing a helical vortex system resulting in a slipstream tube which contracts downstream. Figure 2.2 shows the effect on the radial velocity and pressure distribution behind a propeller. A good description of a slipstream tube is provided by L.L.M.Veldhuis [3].

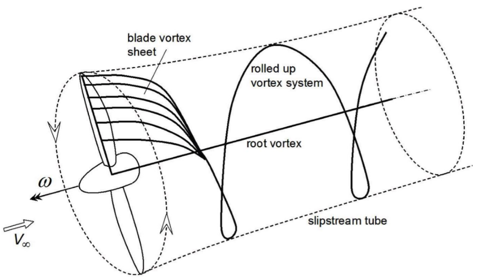

Figure 2.1: Sketch of a propeller slipstream and helical vortex system [3]

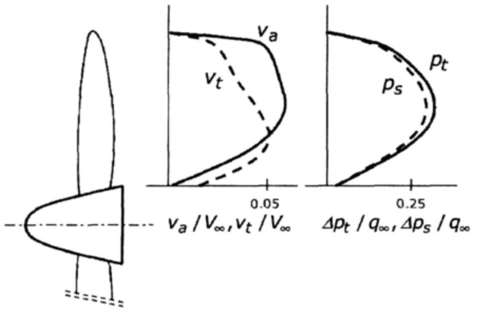

Figure 2.2: Radial distribution of velocity and pressure profiles behind a lightly loaded propeller [3]

A representation of the axial velocity v_a and pressure development in the slipstream tube is provided in Figure 2.3. The propeller's rotation causes a jump in total pressure p_t at the rotor plane, while static pressure p_s decreases towards the propeller, jumps at the rotor plane, and then returns to ambient levels in the far wake. To maintain mass flow continuity, the slipstream cross-section shrinks as velocity increases downstream, with greater contraction occurring under higher propeller loading [3].

A simplification of the propeller is a zero-thickness actuator disc producing a pressure jump, representing the average effect of the rotating blades. This model assumes irrotational and inviscid flow, constant air density, no tangential velocity component and a constant pressure jump at the disc area. [4] [5] The classical Momentum Theory, which considers the rotor as an actuator disc and the conservation laws of fluid dynamics, predicts that the increase of the velocity in the far-downstream plane is twice the induced velocity at the rotor plane. Due to mass-conservation, the slipstream cross-section area contracts inversely proportional to the velocity. In case the rotor is at hover, the area of the slipstream at the far-downstream plane is a 1/2 of the rotor disc area. [6]

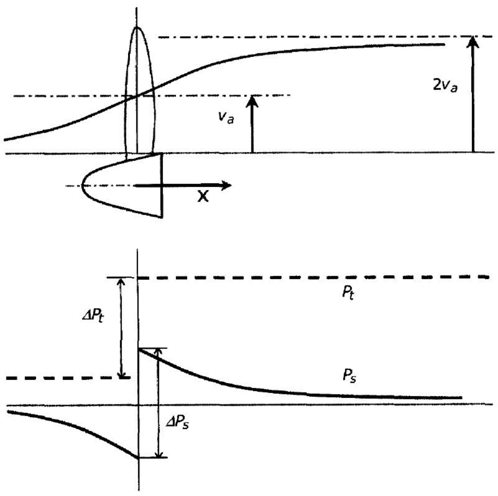

Figure 2.3: Sketch of the streamwise development of axial velocity, static pressure and total pressure according to an actuator disk model of a propeller. [3]

A non-dimensional parameter which a propeller's performance is dependent on is the advance ratio (J). It relates the axial to the rotational velocity which affects the local blade section pitch angle [7]. As the ratio increases this angle decreases and hence, the generated thrust. The ratio is expressed as:

$$J = \frac{v_\infty}{n \cdot D} \tag{2.1}$$

Where v_∞ is the freestream velocity, *n* is the rotations per second and *D* is the propeller's diameter. The advance ratio affects other basic non-dimensional parameters determining the propeller performance such as the coefficient of thrust (C_t), coefficient of power (C_p) and efficiency η. Their definitions are as follows:

$$C_T = \frac{T}{\rho n^2 D^4} \tag{2.2}$$

$$C_P = \frac{P}{\rho n^3 D^5} \tag{2.3}$$

$$\eta = J \frac{C_T}{C_P} \tag{2.4}$$

Figure 2.4 shows an example of a typical performance effect by variation of J on the thrust, power coefficient, and efficiency of the propeller. It can be observed that with decrease in J, the thrust and power production increases, while the efficiency reaches maximum at a specific condition. The flattening of the thrust and power coefficient curves at lower advance ratios could be explained by boundary layer growth causing eventual flow separation [7].

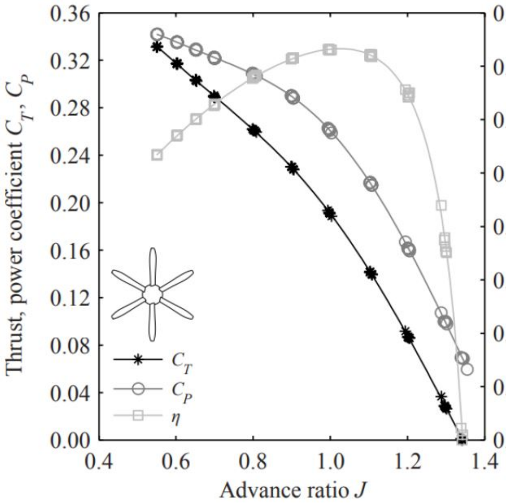

Figure 2.4: Propeller performance parameters versus advance ratio [7]

2.2. History of ducted propeller

The ducted propeller represents a propeller enshrouded typically by a cylindrical wing. In case the chord of the duct is larger than the propeller diameter, the system is called *shrouded propeller*, while if the chord is less than the propeller's diameter, the system is *ducted fan*. [8] The concept of ducted propeller traces back to the year of 1910 when the Bertrand Monoplane was created, which made use of both tractor and pusher propellers in a single duct. The advantage of the duct's potential of increasing the propeller's efficiency has been observed in 1933. A popular science magazine has stated that the flight velocity might be increased between 39 and 140 percent by surrounding the propeller with a shroud. However, this statement seems to be overestimate the true potential of the duct. Considering that an aircraft's drag increases approximately with the square of its velocity (within the subsonic range), doubling the velocity would lead to a quadruple increase in drag. Consequently, four times more thrust would be needed to maintain that speed. [9]

An interesting patent by Carl E. Hall represents the use of adjustable vanes inside the duct with the purpose of increasing the drag during landing stage. The ducted propellers appeared in 1950s in the design of vertical take-off and landing (VTOL) vehicle, namely the Hiller 1301 flying platform. The system relied on the duct for producing nearly 40% of the total thrust. This was primarily achieved through the design of the duct's lip, which accelerated incoming air and created a low-pressure region that contributed to the overall thrust. The Hiller flying platform, however, suffered from excessive stability, making horizontal movement difficult and ultimately leading to the project's abandonment. Nonetheless, modern ducted designs continue to exploit inlet-generated thrust resulting from low-pressure regions. [9]

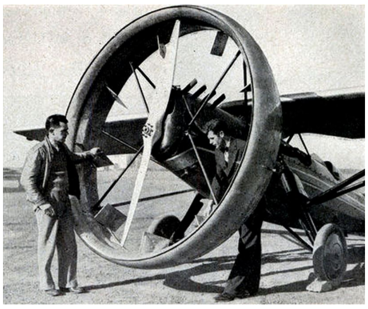

Figure 2.5: Aircraft cowling patented by Carl E. Hall [9]

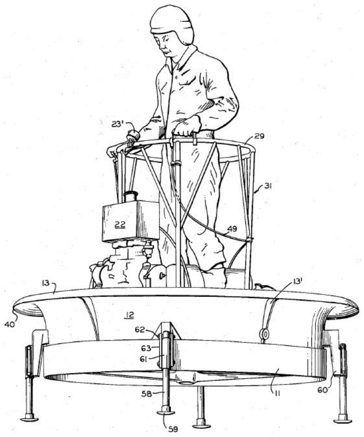

Figure 2.6: Hiller 1031 flying platform [9]

The first known aircraft to incorporate such a system was the Stipa-Caproni (1932). This design featured a piston engine and propeller enclosed within a converging-diverging, tube-shaped fuselage. The goal was to accelerate the airflow through the tube via the Venturi effect, thereby increasing thrust compared to an unducted configuration. Initial test flights confirmed that the aircraft achieved lift-off sooner than anticipated. However, the ducted fuselage also introduced excessive aerodynamic stability, which significantly hindered maneuverability. Furthermore, the long duct increased the wetted surface area, resulting in higher profile drag, ultimately limiting the aircraft's top speed to just 81 mph. Further research into fuselage-mounted ducted fan engines took place during the 1960s. One example is the XAZ-1 Marvelette, which incorporated control vanes within the duct to enable pitch and yaw control. In parallel, a separate research program focused on vertical take-off and landing (VTOL) capabilities led to the development of the Bell X-22. This aircraft was equipped with four ducted fan units capable of rotating 90 degrees, allowing for both VTOL and forward flight. The X-22 later served as a baseline for the design of the Bell-Boeing V-22 Osprey tilt-rotor aircraft. Despite promising test results, the U.S. military eventually has lost interest in the X-22 program. In more recent years, Airbus has pursued research into hybrid-electric propulsion, leading to the successful demonstration of the E-Fan prototype in 2014. This aircraft featured fully electric ducted fans, showcasing the potential of electric-powered flight.[10] Some other examples of fixed-wing aircraft implementing the ducted propeller are Cessna XMC, Edgley Optica, MS State University's XAZ-1 and XV-11, Rhein-Flugzeugbau RF-1, Fantrainer 400, and 600. [8]

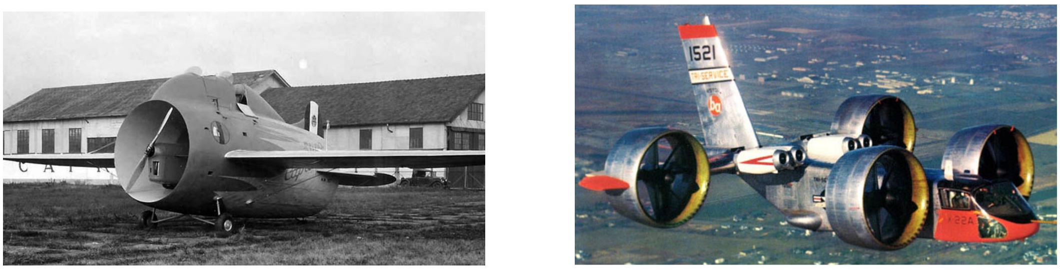

(a) Stipa Caproni (1932) [10]

(b) Bell X-22 (1966) [10]

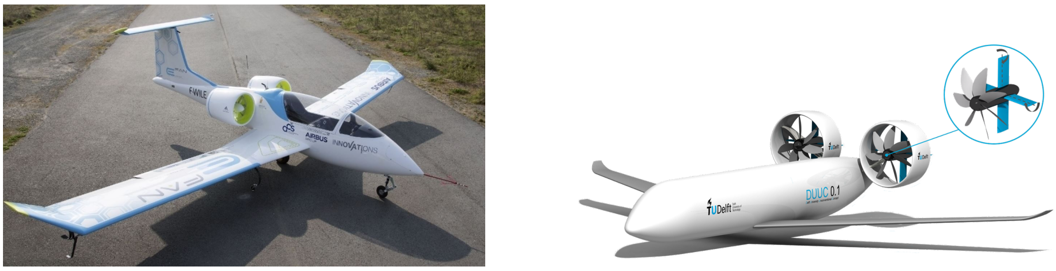

(c) Airbus E-Fan (2014) [10]

(d) DUUC: TU Delft concept [11]

Figure 2.7: Examples of aircraft implementing the ducted propeller

In recent years, significant research has been devoted to the study of shrouded propellers. A notable example is the Delft University Unconventional Configuration (DUUC) aircraft concept, implementing two ducted propellers located at the aft end of the fuselage. This configuration allows the integration of control surfaces within the duct itself, eliminating the need for conventional horizontal and vertical tails. In the tested scaled model, these control surfaces are positioned inside the duct, downstream of the propeller. However, future iterations of the design plan to alter this feature by incorporating the control surfaces directly into the duct wall. [9] History shows that numerous attempts have been made to develop successful aircraft incorporating ducted fans. However, to date, no aircraft has exclusively utilized a tandem DFS configuration functioning simultaneously as both horizontal and vertical stabilizers with integrated control surfaces. This makes the ducted-fan propulsive empennage a distinctive feature of the DUUC, setting it apart as a unique aircraft concept. [10]

2.3. Ducted vs isolated propeller

The ducted propeller represents a propeller enshrouded typically by a circular duct. It may be considered as a hybrid between a propeller and a turbofan engine. The duct is commonly considered as an annular wing. [12] A duct optimized for most efficient production of maximum static thrust, generally does not perform well in a forward flight. This is true vice versa as well. Hence, a good balance should be found between forward flight and static thrust performance of such engine depending on an aircraft design requirements. The ducted propeller inlet design can be split in two types - flow accelerating and decelerating. For a vertical thrust production optimization the duct features a bell mouth inlet allowing the flow to be accelerated at the face of the fan by the circulation of the shroud. This type of duct, however, leads to a high drag penalties in forward flight. The better suited type for forward flight applications is the decelerating inlet leading to lower airflow velocity at the fan face due to a lower circulation of the duct. This is detrimental for the static thrust production, however, ”net thrust is developed on the shroud while the benefits of finite blade loading are retained. With judicious shroud design for intended flight speeds, a net increase in efficiency can be obtained over an open propeller.” [13] The ducted propeller has several advantages and disadvantages compared to the isolated propeller and are summarized below.

2.3.1. Advantages

- **Greater static thrust:** The ducted fan can produce greater static thrust for the same rotor area. [14][15]
- **Increased propeller efficiency:** Depending on the duct lip geometry and inflow velocity, the duct

can significantly reduce the loading on the propeller, allowing for an increased propeller operation efficiency. The duct's inlet lip accelerates the flow forming a region of low static pressure upstream of the lip, contributing to the total thrust force production [15] [16]

- **Increased blade loading towards the tip:** A small tip clearance allows for the suppression of the adverse tip losses effects and hence, the loading of propeller blades to be increased towards the tips. [15]
- **Significant thrust contribution from duct:** Despite that specifically the propeller thrust is lower, the combined thrust produced by the duct and propeller is capable of exceeding the one of an identical isolated propeller. [15][17]
- **Less power required:** The pressure at the duct exit is nearly atmospheric leading to a reduction of the slipstream contraction compared to an isolated propeller case. [15][6] The exit area of the duct may be larger than the propeller, reducing the exit velocity and increasing the required mass-flow to produce the same thrust. Hence, the ducted fan requires less power compared to an isolated propeller to produce the same thrust. [8]

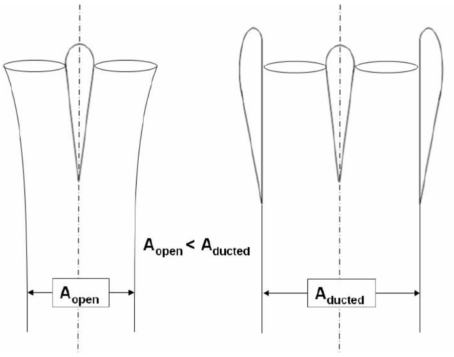

Figure 2.8: Slipstream contraction comparison between open (left) and ducted propeller (right) [15]

Figure 2.9 shows the static pressure distribution in the streamtube of a ducted- compared to free propeller.

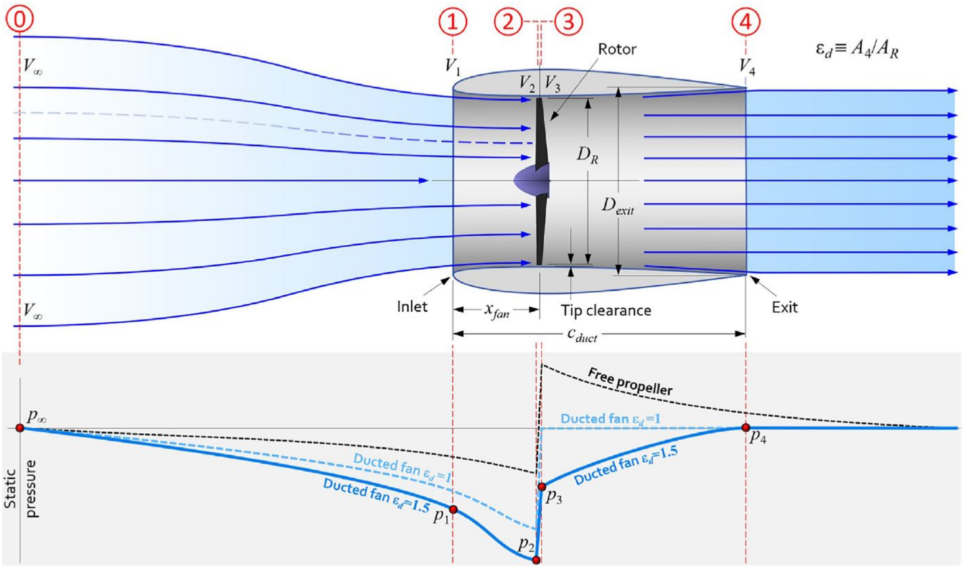

Figure 2.9: Sketch of a ducted fan streamtube with corresponding static pressure development [8]

The equation relating the power required by the ducted propeller to the free propeller is [8]:

$$\frac{P_{ducted}}{P_{free}} = \frac{1}{\sqrt{2}} \left(\frac{T_{ducted}}{T_{free}} \right)^{1.5} \sqrt{\frac{1}{\varepsilon_d}} \tag{2.5}$$

Considering the same exit- and rotor disc area (expansion ratio: $\varepsilon_d = 1$), the ducted fan would require 71% of the required power of the free propeller to produce the same static thrust. In case the same power is provided, the ducted fan would produce 26% higher thrust. [8]

- **Lower diameter required for same static thrust:** The open propeller relies on pressure difference across the rotor for thrust production while the ducted propeller - on the mass-flow through the duct. Due to the increased mass-flow, a ducted fan can achieve the same static thrust as an open rotor with an inner diameter that is only 50% to 60% of that required by the open rotor. [15]
- **Physical protection:** The duct increases the physical protection of objects and personnel from the spinning blades of the propeller. [15]
- **Noise level reduction:** Reduction of tip losses contributes to a reduction in radiated noise levels of the propeller. [15] [8]

2.3.2. Disadvantages

- **Flow separation at high AoA:** The ducted fan onsets the promotion of a flow separation at high angles of attack at the lip of the duct. This causes a deterioration of the propeller's inlet flow, especially at the leading edge and the tip clearance region. [18]
- **Reduced controllability at descend:** At low horizontal speeds, pronounced lip separation can significantly limit the rate of descent and reduce vehicle controllability. The lower power demand typical of descent leads to decreased disk loading, which further intensifies lip separation. [18]
- **Minimum RPM required** Due to the dominating viscous forces of the duct's internal flow at low RPM, the duct becomes disadvantageous for net total thrust production by the ducted compared to an isolated propeller. [19]
- **Momentum (Ram) drag:** Specially applicable to ducted propeller of Vertical Take-Off and Landing (VTOL) aircraft, the momentum drag results from the change of the direction and hence, momentum, of the freestream air exerted by the ducted propeller as illustrated in the following figure:

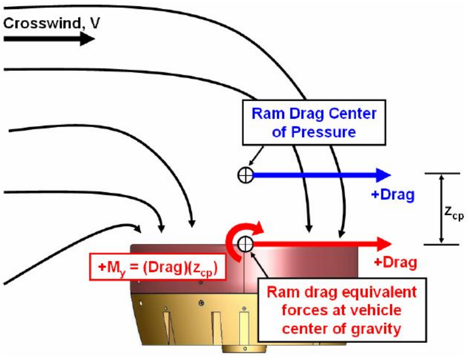

Figure 2.10: Change in freestream direction by a VTOL engine [15]

To conserve momentum, a force must be applied at the center of pressure of the turning airstream. The center of pressure for ram drag is typically located above the vehicle's center of gravity, which is usually at or just below the duct lip, resulting in a positive pitching moment. Minimizing this component of total drag is crucial, as it constitutes a significant portion of the vehicle's overall drag. Additionally, the positive pitching moment from the momentum drag force causes the duct to rotate, aligning the thrust vector with the wind direction and reducing the UAV's ability to hold position in windy conditions. This issue is less pronounced with open rotors, as they lack a duct to constrain the airflow. [15]

- **Asymmetric lift:** During a crosswind or forward flight, the forces needed to redirect the airflow into the duct create a region of lower pressure on the windward side compared to the leeward side. This pressure difference results in greater lift on the windward side of the duct. The asymmetric lift can also be seen as the physical mechanism of the momentum drag effect. [15]
- **Prone to instability in forward flight:** The asymmetric lift and ram drag both result in adverse pitching moment which could have destabilizing effect during steady forward flight. [18]

- **Increased drag:** Increased wetted area, causing increase in airplane drag. [8]
- **Increased costs:** Increased component manufacturing and maintenance costs. Also, a tight tip clearance would additionally contribute to the high precision manufacturing costs. [8]
- **Speed application limitation:** The ducted fans are more suitable for lower freestream velocity than an isolated propeller. A turbofan engine, however, is best performing at high Mach numbers, while the thrust at low velocities is produced mainly by the hot section. A turbofan combines a fan with a core engine, meaning that both the thermal cycle and the mass flow of air must be considered. While efficiency can be increased at higher airspeeds, this typically comes at the cost of reduced performance at lower speeds unless variable-pitch mechanisms are used. [8]

2.4. Flow separation

The flow separation is a phenomenon occurring due to the viscosity effects between a fluid in motion and a wall surface. The boundary layer velocity profile shape is characterized at the different flow conditions. Figure 2.11 shows the attached flow and separation onset velocity profiles.

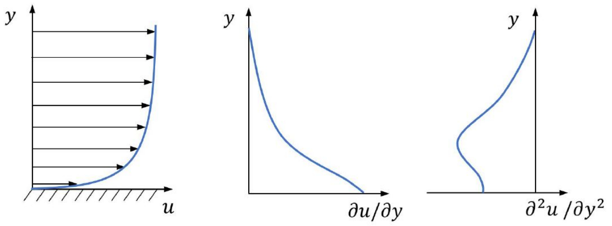

(a) Attached flow

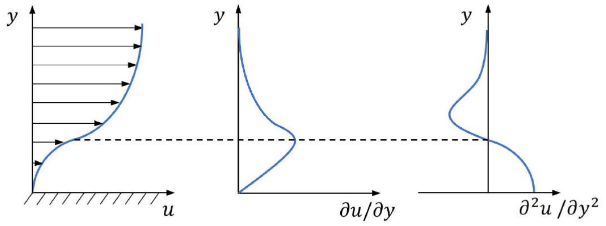

(b) Separation onset

Figure 2.11: Velocity profile of attached flow and separation onset condition [20]

The attached flow is characterized by a concave velocity profile with positive velocity gradient $\partial u/\partial y$ with only $\partial^2 u/\partial y^2 < 0$ being sufficient requirement for a boundary layer to be attached. [21] The separation onset point is characterized by $\partial u/\partial y = 0$ at the wall and an inflection point of the profile near the wall. This inflection point is defined where $\partial^2 u/\partial y^2$ switches from positive to negative sign. In case $\partial u/\partial y < 0$ at the wall, the flow near the wall propagates in a reverse direction of the main flow, causing the so called *boundary layer separation*. Hence, the condition for flow separation is:

$$\left(\frac{\partial u}{\partial y}\right)_{wall} < 0 \tag{2.6}$$

According to Prandtl [22] the 2D general differential equation describing the boundary layer at a wall (y=0) where the tangential and normal component of the velocity are zero is:

$$\left.\frac{\partial p}{\partial x}\right|_{y=0} = \mu \left.\frac{\partial^2 u}{\partial y^2}\right|_{y=0} \tag{2.7}$$

It is indicated that for curvatures that is for which $\partial^2 u/\partial y^2 > 0$, the pressure is required to increase for the flow separation to occur. [22] The pressure gradient $\partial p/\partial x$ along a body is favorable if it is negative, accelerating the flow along the surface. In case the flow is decelerated, the pressure gradient is positive (adverse pressure gradient) where viscous stress and pressure forces prevail, leading to a rapid boundary layer thickness growth. [23] [24] Due to pressure and friction dominance, the momentum and energy of the fluid are decreased downstream. This leads to a point where the fluid particles reach a state of rest and begin leaving the surface. Further downstream the flow propagates in a reverse direction to the main flow forming a separation region in the stream-line diagram, typically filled with a low velocity vortices. [25] This region significantly differs from the inviscid theory predictions. It results in a strong pressure drag on the body that is much greater than the viscous drag exerted by the boundary layer. The location where flow reversal occurs is called *boundary layer separation point* and is found typically a short distance after the point where the pressure gradient sign changes. [23] The flow separation phenomenon is depicted in Figure 2.12 along with the two general types of attached flow - laminar and turbulent boundary layer.

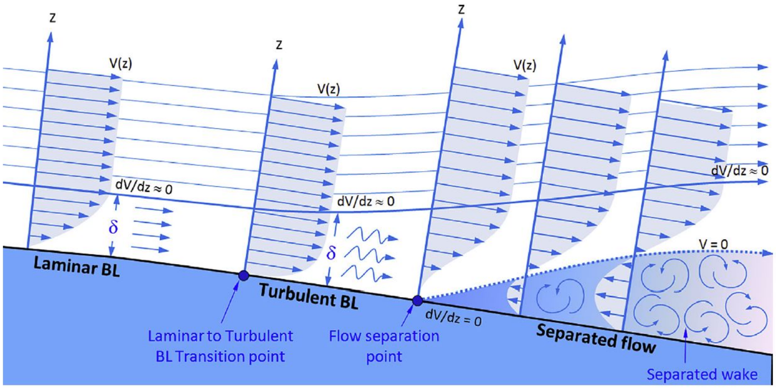

Figure 2.12: Flow velocity in laminar and turbulent boundary layer vs separated flow [24]

2.5. Lip flow separation effect on performance

The inlet airflow is directly affected by the freestream velocity, propeller operating setting, angle of attack and lip geometry. Depending on the specific lip geometry, a suction peak is present at this area promoting adverse pressure gradients leading to a tendency of the flow to separate from the lip's contour.

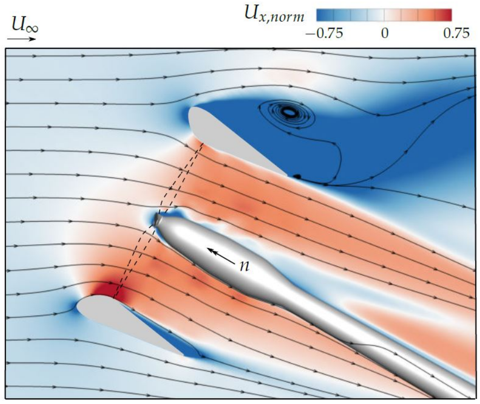

Figure 2.13: CFD study of normalized induced axial velocity at 30 degrees angle of attack of a ducted propeller engine showing the suction peak at the windward side of the duct [16]

The detrimental effects of the airflow separation at the lip of the ducted propeller are listed as follows [18]:

- **Reduction of thrust:** A lip separation causes a low momentum and recirculatory turbulent airflow at the engine's inlet leading to reduction of the produced thrust.
- **Flow instability:** The interaction of the distorted inlet flow with the tip clearance gap, causes an increase in aerodynamic losses and temporal flow instability at the rotor face. This deteriorates the energy addition capability or the propeller.
- **Static pressure imbalance:** Imbalance of the inner static pressure occurs due to the low momentum at the inlet of the duct, while the outlet fluid becomes excessively energized. The trailing edge total pressure is typically much higher compared to the case at the leading edge.

- **Increase in power required:** The lip separation leads to an increase in power required and fuel consumption for given operational task.
- **Noise increase:** The distorted inlet flow causes the radiated noise levels from the operation propeller to increase.
- **Greater effect on control surfaces:** The interaction of the flow at the duct's exit with the control surfaces becomes much greater.

The flow separation, however, can not only have detrimental effect on the ducted propeller's performance. The lip separation area can contribute to reducing the adverse pitching moment generated by the momentum drag and asymmetric lift. [15]

2.6. Tip clearance distance

The design of a ducted propeller involves a finite closest distance between the duct's interior wall and the tip of the propeller, called *tip clearance distance*. This distance is defined as a percentage of the duct's throat diameter [6]:

$$\delta^*_{\text{tip}} = \frac{\delta_{tip}}{D_d} \cdot 100 \tag{2.8}$$

The flow field between the wall and the tip has a complex structure due to the interaction of tip leakage flow, the annulus wall boundary layer, and the propeller's wake. The generated pressure difference between the suction and the pressure side at the blade tip allows the formation of a tip leakage flow, which rolls up into a highly three-dimensional tip leakage vortex. This vortex exhibits strong turbulence and unsteady characteristics within each passage. The tip leakage vortex is also one of the dominant noise sources in unsteady interactions in turbo-machinery systems and contributes significantly to energy losses in ducted fans. Therefore, the common design of a ducted propeller aims for minimizing tip clearance such that the tip losses are reduced enhancing the aerodynamic performance. [26] Several studies have been performed on the three-dimensionality of the tip leakage vortex in axial flow fans and compressors in literature [27–31].

The Akturk et al. [26] paper has investigated the effect of the tip clearance distance with respect to the blade height (t/h) on a ducted rotor, indicating that the suppression of the tip losses at the blade tip decreases with increasing this distance. This shows that reduction of the tip leakage flow benefits the increase in the total pressure difference generated by the propeller blade towards the tip as displayed in Figure 2.14:

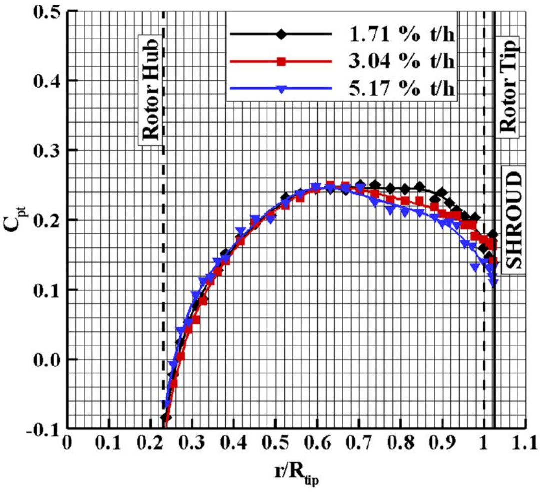

Figure 2.14: Radial distribution of the total pressure coefficient with various tip clearance sizes between an operating propeller and a shroud. The figure shows that the propeller loading increases towards the tip with decreasing the tip clearance size. [26]

This effect is recognizable also for the coefficient of thrust versus power and the rotational speed, where the smallest tip clearance produces the largest thrust, and power coefficient for a given RPM. The paper further reports a numerical visualization of the total pressure change of the flow field with respect to increasing tip clearance distance shown in Figure 2.15. The minimum loss regions are indicated in red, while the maximum losses in blue. It is indicated on the figure that the reduction of the tip clearance size benefits the minimization of the tip leakage flow, leading to maximizing the total pressure jump within the duct's inner diameter.

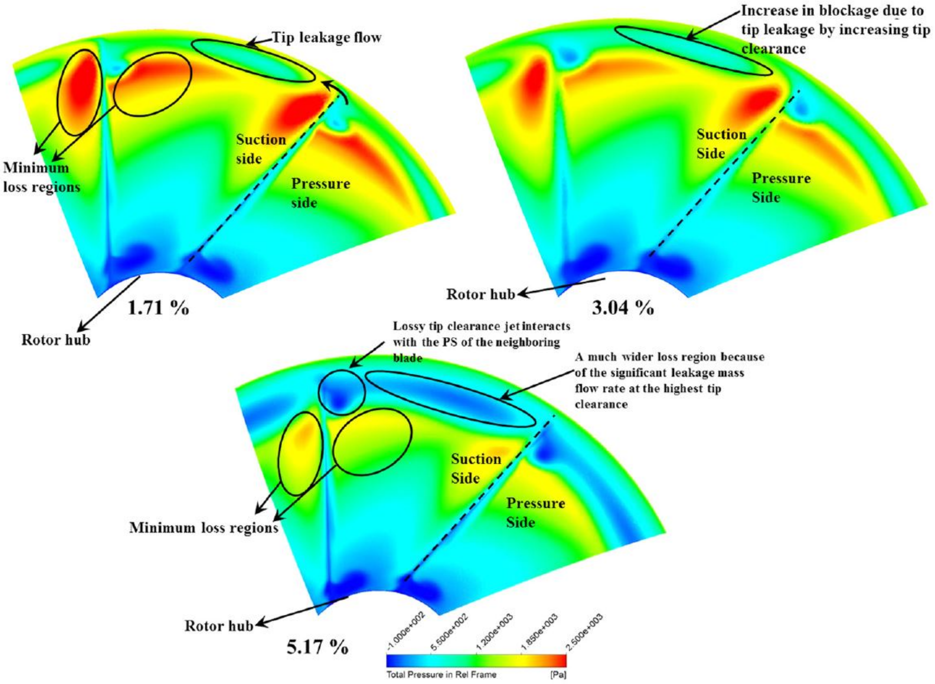

Figure 2.15: Relative total pressure distribution at the rotor exit plane of an operation ducted propeller with various tip clearance sizes. The figure indicates that the tip leakage flow is most optimally suppressed at minimum tip clearance, leading to maximizing the minimum loss regions (in red). [26]

It can be observed that the increase of tip clearance leads to significant aerodynamic loss near the tip due to a stronger tip clearance flow. This flow interacts with the neighbouring blade causing a large local loss region that propagates towards the propeller's mid-span. Furthermore, the blockage flow due to the tip leakage is also increased and the minimum loss regions indicated by red and yellow color are drastically reduced. The corresponding velocity contours in Figure 2.16 comparing two tip clearance distances show the distinctively greater tip leakage at the shroud's wall for the greater tip gap [26]:

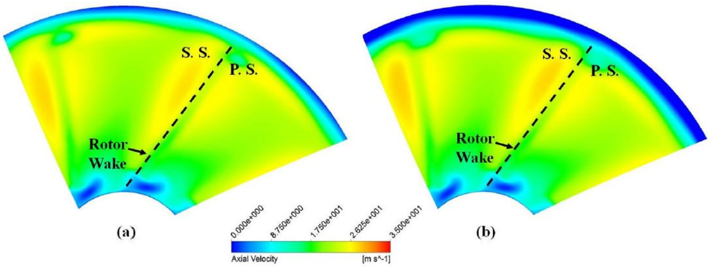

Figure 2.16: Comparison of the axial velocity contour at the rotor exit plane of an operating ducted propeller. The figure indicates that the low momentum flow near the duct's inner surface is reduced at smaller tip clearance [26]

Despite that the tip clearance distance should be as low as possible for maximizing the aerodynamic performance, the minimum tip clearance is limited by prevention measures for damaging the duct's body by the spinning blades. This could happen either due to excessive vibrations or flapping amplitudes of the blades. [6]

The tip clearance distance also affects the aerodynamic properties of the duct. The smaller the gap, the greater difference between the local static pressure at the duct's lip and the freestream pressure. This results in greater thrust production by the geometry of the duct. The effect of the variation of the tip clearance on the aerodynamic performance of a ducted propeller has been studied and indicated that the largest thrust force achieved by the duct is obtained at minimum tip gap distance, while the rotor thrust remains unaffected, as shown on Figure 2.17. [32] [33] This is contradictory finding to Akturk et al. [26], which found that the increasing the tip clearance distance decreases both the rotor and the duct thrust. This difference in the findings might be due to the fact that Akturk et al. [26] used an 8-bladed rotor, while Goudswaard et al. [33] used a 2-bladed rotor in their research. As the number of blades are decreased, the spacing between a rotor blade tip and the vortex shed by the preceding blade increases, which reduces the interaction losses. [32]

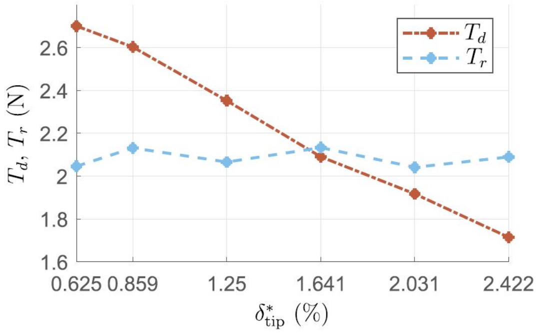

Figure 2.17: Comparison of the thrust produced by the duct versus the propeller for various tip clearance sizes [33]

The Li et al. [34] paper investigates the aerodynamic characteristics of ducted propellers in axial and tilted flow stated based on a numerical study. The analysis is based on a 381 mm in diameter NACA ducted propeller with tip clearances in the range of 0.1-3.0% of the propeller diameter (D) at freestream velocity of 30.48 m/s and propeller rotational speed of 8000 RPM. It is reported that the tip vortex does not change noticeably up to 0.2%D, while increasing it up to 2.0%D the duct's ability to suppress the blade tip vortex is decreased. When increasing the tip clearance beyond 2.0% of the duct's diameter, the tip vortex intensity is no longer observed to be affected significantly.

Hu et al. [35] paper investigates a grooved duct configuration as a method for hovering efficiency improvement under large blade tip clearance. The research compares the performance of multiple cases involving conventional and grooved duct to a baseline configuration of a 381 mm in diameter duct with tip clearance of 0.4% of the duct diameter. The paper reports that the hovering efficiency decreases significantly when the tip clearance is increased to 4 times the baseline clearance. The thrust of the duct is reduced by 60% once the tip clearance exceeds 4 times the baseline case, while the power required by the ducted propellers does not vary noticeably, causing the efficiency to drop. However, the grooved ducted configurations show superior efficiency than the baseline. It is reported that the efficiency can be 5% higher with 6 times larger tip clearance than the baseline for a grooved case. The tip gap is a common subject of research for application in axial fans and compressors. [31][36][37]

2.7. Duct shape effect on performance

The duct's aerodynamic performance is affected by its cross-section airfoil shape. The paper Koç et al. [17] analyzes separately the effect of thickness and camber of a duct's cross-section airfoil on the production of thrust by the duct and the propeller. The studied duct configurations have identical narrowest inner radius where the propeller is installed, aspect ratio, and tip clearance properties. The analysis shows that the greatest benefit for the duct's thrust production is the cambered airfoil case. The thrust data for varying advance ratio *J* is provided in Figure 2.18 where the reference symmetric airfoil Naca 0018 is compared to the thinner Naca 0012, and Naca 4312 serving as representation of a cambered airfoil.

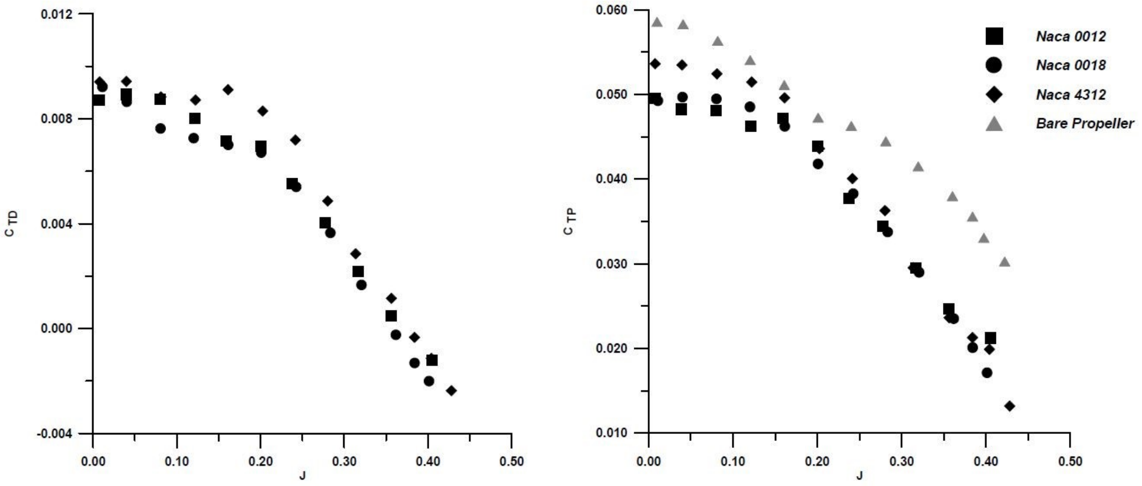

Figure 2.18: Thrust comparison between duct and propeller [17]

It is observed that with increase of advance ratio, the thrust decreases for both duct and propeller. At high *J* the duct leads to generation of negative thrust (drag), while at lower freestream velocities (low *J*) the duct's geometry has a strong influence on the propeller's thrust production. It is reported further by the Koç et al. [17] paper that the cambered airfoil leads to lowest power required for generating the same total thrust and achievable better efficiency of the shrouded than the isolated propeller with increasing the rotational speed of the motor.

Graf [15] paper studies the effect of the lip geometry variation on the separation region at the lip. The baseline geometry is designed with a relatively small leading edge skewed towards the exterior contour of the duct allowing the pressure gradient to change gradually. The other lip designs were selected to be enlarged, elliptical, circular arc, and revised as shown in Figure 2.19.

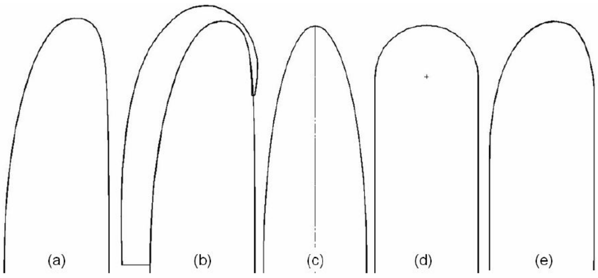

Figure 2.19: Investigated duct lip shapes (a) Baseline, (b) Enlarged, (c) Elliptical, (d) Circular Arc, and (e) Revised. The left side of each lip corresponds to the interior of the duct. [15]

Wind-tunnel tests were performed with a freestream velocity between 3 and 26 m/s and a fan rotational speed of 5000 to 8000 RPM, while the pitch angle is ranges between 0 and 90 degrees with respect to the incoming air. Performed were both static and forward flight tests. The outcome suggests that the baseline, enlarged, and revised lips show the greatest trade-off for both flight conditions with the baseline outperforming the other designs in the forward flight case while does not lead to a large thrust reduction at static conditions. It is further pointed out that the duct shape is one of the main factors for the pitching moment characteristics. In forward flight a smaller radius leading edge and shorter chordlength of the inlet lip would benefit the generation of separation reducing the adverse pitching moment, lateral forces, surface friction and pressure drag, while still being able to prevent the formation of tip vortices. A larger radius would benefit the static condition allowing the flow to be attached and increase the thrust. [15][16]

2.8. 2D vs 3D flow analysis

The flow around a ducted fan has profound three-dimensional effects, especially at high angles of attack. This has been documented by Young [38] who conducts a CFD study on vertical take-off and landing (VTOL) aircraft's ducted fan performance. The study reports the behavior of the flow at transitional flight regime from hover to forward flight where the angle of attack is substantial. The study shows that the flow around a ducted fan in transitional regime is highly three-dimensional. "The high degree of three-dimensionality is a cautionary note to ducted-fan aircraft aerodynamicists and designers to be careful in not relying on oversimplified assumptions and analysis for these vehicles, especially in the transition flight regime." [38]

Cerny et al. [16] reports that the discrepancy between the pressure distribution at the propeller's surface and the 2D polar data is due to the 3D flow effects and the non-axial velocity components at an angle of attack. These effects generate additional local axial and tangential velocity components, leading to changes in both the magnitude and direction of the local inflow velocity. Hence, the pressure gradients and the pressure difference between the suction and pressure sides of the blade are affected. Furthermore, the non-axial inflow introduces periodic variations in these effects. This consequently makes the flow separation, radial flow, and the thrust generated by the propeller periodic as well. More specifically, the advancing and retreating blades may experience opposite thrust contributions. This imbalance leads to additional pitching and yawing moments, as well as asymmetric tip vortices. Additionally, the non-axial inflow conditions increase the blade vortex interaction by the deflected wake, resulting in unsteady loads on the propeller.

The differences between the 3D and 2D representation of a ducted fan can be rather small depending on the angle of attack with respect to the airflow. A comparison of a ducted wind turbine performance has been performed by Dighe et al. [39] comparing the performance of the ducted turbine under variation of yaw angle with respect to the incoming flow. Compared are the CFD study results from representation of the turbine as a 2D and 3D ducted actuator disc. The study is performed using URANS flow equations. The Figure 2.20 compares the obtained CFD results with experimental data for a wind turbine used to validate them. The graph shows the ratio $r = C_P/C_{P_o}$ on the vertical axis relating the power coefficient of the ducted C_P versus isolated fan power coefficient C_{P_0} with the same actuator disc and similar operating conditions for both cases. The horizontal axis plots the investigated yaw angle.

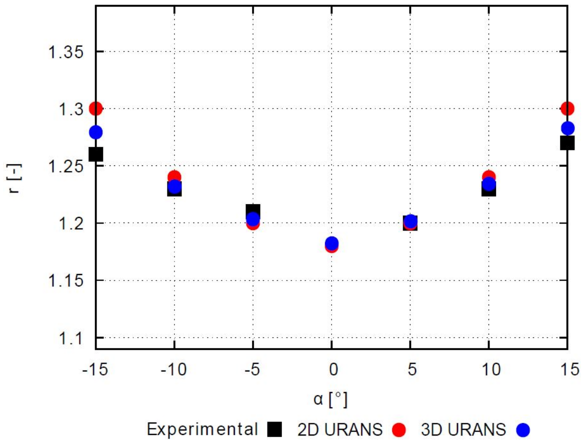

Figure 2.20: Comparison between 2D, 3D, and experimental results of a ducted wind turbine performance versus yaw angle [39]

Observed is that a good agreement of the data is achieved at the condition where the turbine is aligned with the airflow, while the difference in the predictions grows with the increase in yaw angle. Nevertheless, reported is that the margin between the 2D ducted fan predictions and the experimental findings is less than 5% at the maximum tested angle (15 degrees). Comparing with the 3D results, the disadvantage of the 2D data is that it does not consider the azimuthal variation of the velocity component at the the actuator disc plane in yawed case. Shown in Figure 2.21 is the time-averaged velocity contours of non-dimensional axial velocity at the actuator disc looking from upwind, serving as an example indication for the variation of the velocity component with the azimuthal angle Φ. [39]

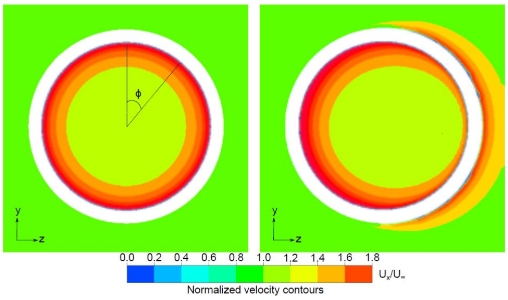

Figure 2.21: Time-averaged velocity contours at aligned (left) and yawed (right) case [39]

However, as shown in Figure 2.20 the difference with the 2D data is negligible when comparing *r*. Furthermore, an advantage of the 2D approach is that it requires four times less computational power compared to 3D, while providing not so large deviations. [39]

3

Blowing jet flow separation control

This chapter describes the literature findings for the principle of a blowing jet method for airflow separation prevention along with appropriate blowing jet properties.

3.1. Principle

The principle of flow separation control by blowing jet method is by increasing the momentum and hence, energizing the boundary layer near a given surface. This is achieved by implementing a slot near the surface through which an airflow is typically injected in a tangential direction to the wall surface so that it matches the direction of the main flow as illustrated in Figure 3.1. A non-tangential injection would result in a large positive normal velocity component leading to a flow blockage of the main flow, decreasing the clockwise spanwise vorticity near the wall, and favoring the adverse pressure gradient growth, rather than suppressing it. A normal injection to the main flow (90 degrees) would could cause a strong flow blockage and separation. [20]

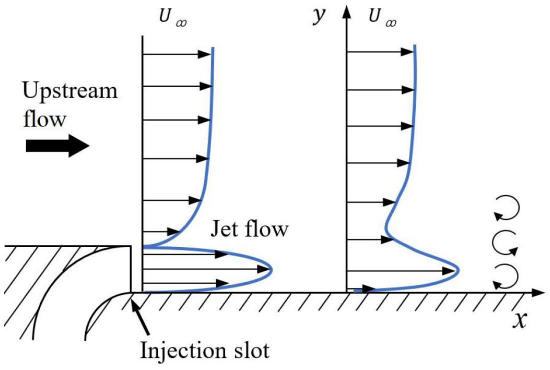

Figure 3.1: Sketch of the near-wall blowing jet principle [20]

The goal is to alter the velocity profile near the surface where the local flow velocity is significantly decreased due to the dominant viscous effects at this location. The decrease in velocity leads to occurrence of adverse pressure gradients causing the flow to separate from the surface's contour as discussed in more detail in section 2.4. Several papers can be found regarding the blowing jet method for prevention of flow separation by active flow control, namely co-flow wall jet (CFWJ or CFJ) airfoil. [20] [40–42]

The injection itself typically makes the boundary layer turbulent. As defined by Launder et al. [43] the wall jet is a ”boundary layer in which, by virtue of the initially supplied momentum, the velocity over some region in the shear layer exceeds that in the free stream”. The wall jet has an inner shear layer similar to a conventional boundary layer and an outer shear layer, which is like a free shear layer. The essential difference between the jet and conventional boundary layer is that the inner and outer shear layers have opposite spanwise vorticity signs or counter rotating vortices and the maximum shear stress of the outer layer is several times larger than the wall shear stress. [43] [20]

3.2. Blowing jet properties

The blowing jet is defined in terms of blowing coefficient, size, chord-wise location, and blowing angle. These characteristics are described in the following sections.

3.2.1. Blowing rate coefficient

The blowing rate coefficient C_μ is a measure of the momentum of the blown air. It has a significant contribution to the effectiveness of the jet for flow separation prevention. Generally, the increase in the coefficient's value leads to greater acceleration of the flow at an airfoil's suction contour and therefore, a greater circulation of the airfoil. [44] The blowing coefficient is expressed by the formula:

$$C_\mu = \frac{\dot{m}_j v_j}{0.5\rho_\infty v_\infty^2 S} \tag{3.1}$$

where $\dot{m}_j$ is the injection mass-flow rate, v_j is the mass-averaged injection velocity, ρ_∞ is the freestream air density, v_∞ is the freestream velocity, and S is the reference area which equals the chordlength for a 2D airfoil. [44] For incompressible flow where the densities of the blown and freestream air are identical, the coefficient from a blowing slot can be expressed as [45]:

$$C_\mu = 2\frac{h_{\mathrm{slot}}}{c}\frac{v_{\mathrm{j}}^2}{v_\infty^2} \tag{3.2}$$

where h_{slot}/c is the height of the slot scaled over the chord length *c* of the airfoil. As the slot would be positioned near the separation point at the lip of the duct, its position would be upstream from the propeller. Hence, the jet's blowing rate would affect not only the velocity profile near the duct's inboard surface, but also the incoming flow at the propeller. Depending on the location of the slot, an optimum value for the blowing coefficient can be found such that a velocity profile uniformity is achieved. Furthermore, the increase in angle of attack would require an increase of the coefficient, due to the increase of the boundary layer thickness and the separation region. [45].

Several studies have investigated the effect of the coefficient on the performance of cambered airfoils. Interestingly, Wang et al. [46] reports using multiple blowing slots with low velocity continuously reinforcing the wall jet to achieve greater efficiency in flow separation prevention than a single blowing slot with much greater velocity. Seifert et al. [47] and [48] report about flow separation suppression by oscillatory blowing achieving low energy input requirement. It is believed that the periodic energy input to the main flow generates large coherent structures, enhancing the mixing and and entrainment, which benefits the flow reattachment. The kinetic energy is brought from the outer inviscid flow, while the turbulent mixing itself contributes to the energy dissipation.

Kim et al. [49] selects blowing a coefficient of 6% to numerically analyze the flow separation control for a stalled airfoil. The study further reports the steady low-blowing jet to be found as detrimental for flow control with values less than $C_\mu < 1\%$, while a large coefficient as approximately 5% can be beneficial for enhancement of the lift of a lifting body. A substantial coefficient is reported as 6% by Matalanis et al. [50] to show ability in completely suppressing dynamic stall. Chabert et al. [51] analyses the flow separation suppression detection over a plain flap using steady blowing. The paper compares the unblown case with 3% blowing coefficient at flap angle of 20 degrees. The air is injected at the leading edge of the flap. It is reported that the 3% coefficient has been able to fully suppress the recirculation zone from the separation region and the flow is observed to be attached over the whole body of the flap. Ganesh et al. [52] applies an active flow control technique to a tubercled wing aiming to improve aerodynamic efficiency by enhancing lift production without compromising with drag penalty. It is stated by the paper the the low-blowing amplitude may cause hysteresis effects.

Chen et al. [53] investigates the steady blowing method for separation flow control at the leading edge of an elliptical airfoil. Adverse effects of steady blowing on lift were observed at low momentum inputs. For wider slots positioned upstream of the natural separation point, drag shows sensitivity to the Reynolds number and is not influenced solely by blowing coefficient. A minimum threshold C_μ of 2.5% is concluded by the paper to be required for overcoming the adverse pressure gradients caused by the incidence angle and leading edge's curvature. This threshold has also been confirmed by Müller-Vahl et al. [54] reporting that the range where the lift reduction switches to lift improvement is found to be

1.7-2.5%. Another notable conclusion made by the paper is that the analyzed leading edge slot triggers the resulting laminar flow separation bubble to burst when the jet velocity is lower than the local boundary layer edge velocity. This caused significant increase in drag and reduction in lift at pre-stall angles of attack. In case the boundary layer is turbulent, the paper indicates that the low-momentum blowing has a significant destabilizing effect of the boundary layer, causing the separation point to occur earlier. If a strong adverse gradients are present downstream of a suction peak, it appears that this would trigger leading edge separation. The paper also suggests that the leading edge separation caused by low-momentum blowing as a potential effective aerodynamic breaking system.

3.2.2. Slot size

The blowing jet size effect has been reported by Wang et al. [44] to not have a significant effect on the flow field. Moreover, the larger the slot is, the lower the airflow velocity through the slot is. Hence, looking at Equation 3.2.1, with constant blowing coefficient, the decrease in injection velocity would require a greater injection mass-flow rate. Figure 3.2, from the same paper, shows the visualized flow field at the injection and suction slots of a cambered CFJ airfoil at 10 degrees angle of attack for various injection slot sizes (A_j). It can be observed that the increase in slot size not only reduces the injection velocity for a given C_μ, but also degrades the uniformity of the injected velocity profile with visible growth of the regions with different local velocity.

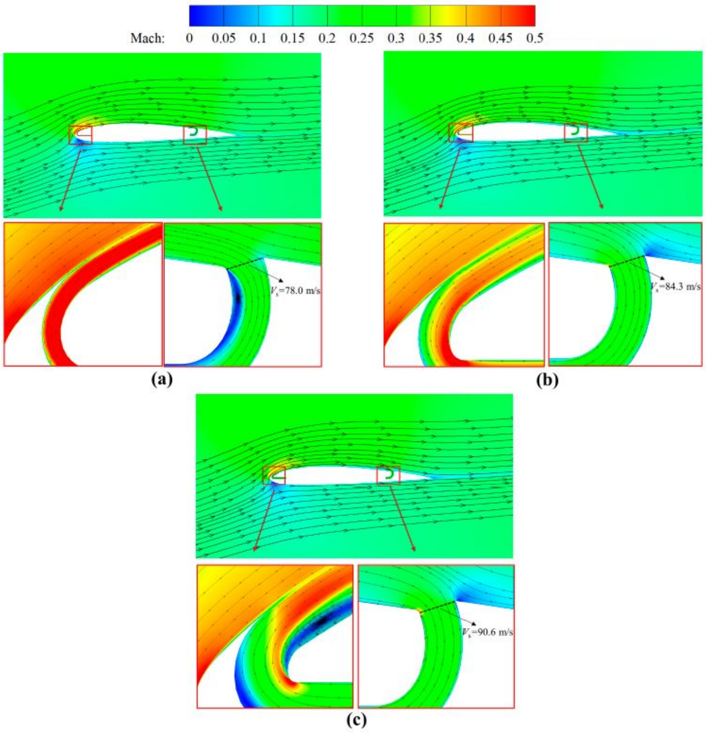

Figure 3.2: Mach contours and streamlines of CFJ2412 airfoil with various injection slot sizes at AoA = 10 degrees. (a) A_j = 0.5%c. (b) A_j = 0.8%c. (c) A_j = 1.2%c [44]

It has been reported that a smaller size of the blowing slot results in higher stall angle of attack and therefore higher maximum lift. Moreover, decreasing the slot size allows for a significant reduction of the energy consumption compared to a larger slot size. [40] It has been also studied that the smaller injection slot favors the lift production and the increase of stall angle of attack, while a larger slot benefits the reduction of drag. [55]. The Tomas et al. [56] paper, investigating 2D synthetic jet configuration for flow separation control, considers a recommendation for the actuation synthetic jet orifice diameter to be within 5-20% of the boundary layer thickness such that the influence of the jet orifice is minimized when not active. Moreover, the paper states that the tangential blowing of the synthetic jets has a beneficial effect to flow separation reduction in case the injected and freestream velocity are with comparable magnitudes.

3.2.3. Blowing location

The blowing jet has been found by literature to be the most optimally placed near the separation point for maximal flow separation control. Xu et al. [20] investigated the flow separation suppression effectiveness of the injection location with respect to the separation onset point. Compared are far upstream, close upstream, and at the separation onset point wall jet locations with the greatest effect and efficiency has been reported to have the close upstream to the separation onset point location. The paper Chen et al. [53] states that when the slot is positioned close to the natural flow separation point, the lift increment is highly sensitive to its location but remains independent of the Reynolds number.

The just upstream the separation point location of blowing has also been reported as most efficient in synthetic jet studies such as Zhao et al. [57] paper which investigates via numerical simulations the synthetic jet control for separation suppression over a rotor airfoil. Based on the jet slot position variation it has been found that the effectiveness of the jet actuator over the tested airfoil decreases with increasing the distance to the separation point based on increment in the lift coefficient data for a given angle of attack. The Tomas et al. [56] paper also supports this finding by recommending the actuation to be positioned near the separation point but not downstream of that point.

3.2.4. Blowing angle effectiveness

As mentioned earlier, implementing a tangential blowing slot with a finite height as shown in Figure 3.1 would minimize the positive normal velocity component leading to a flow blockage of the main flow. However, it also represents an obstacle for the flow that would trigger separation when the blowing jet is not active. To prevent this it has been selected the slot in this project to be inscribed in the airfoil's geometry instead such that the airfoil's contour is maximally preserved. The jet is then unable to be tangential to the local airfoil contour. Instead, the jet injection in the main flow is selected to rely on Coanda effect that redirects the injected flow tangentially to the main flow direction. To maximize the tangential velocity component, the slot is oriented at an angle with respect to the local curvature such that the Coanda effect can be maximized, while the slot can be inscribed in the wing's geometry.

The Coanda effect is a phenomenon in fluid dynamics that describes the tendency of a fluid jet, such as air, water, or another natural fluid, to deviate from its original trajectory and attach itself to a nearby surface rather than continuing along a straight path. First observed by Romanian aerodynamicist Henri Coanda in the early twentieth century, this effect occurs when a fluid jet interacts with a curved surface, causing it to follow the surface contour due to pressure differences between the jet and the surrounding fluid. The lower pressure along the inner side of the curved surface draws the jet toward the surface, resulting in the fluid adhering to it and, in some cases, even wrapping around it. [58]

The Coanda effect plays a significant role in high-lift systems such as flaps and blown flaps. When deployed, these devices create curved surfaces that promote airflow attachment and downward deflection due to the Coanda effect, thereby increasing the effective wing area and enhancing lift production. This principle is widely implemented in commercial aviation, allowing aircraft to operate at lower speeds during takeoff and landing. In addition, the Coanda effect presents considerable potential for improving aircraft maneuverability and control through thrust vectoring technologies. By deliberately redirecting engine exhaust, thrust vectoring leverages the Coanda effect to generate additional control forces, offering advantages for combat aircraft, vertical or short takeoff and landing vehicles, and unconventional airframe configurations. Coanda effect nozzles make use of this principle by employing control jets to deflect the primary jet stream, enabling rapid and efficient changes in thrust direction without relying on conventional control surfaces such as rudders or ailerons. [58]

The angle of blowing has been researched by several papers such as Kankatala et al. [59] focusing on separation flow control on thick wind turbine airfoils using active steady and unsteady blowing method. The study analyzes the injected air development for a range of blowing angles using numerical analysis. It is reported that for the same momentum the jet flow has the greatest effectiveness in staying attached to the airfoil's wall surface and hence, suppressing the separation region, with blowing angles of up to 40 degrees. Higher angles result in recirculation areas despite that the blowing is done at the optimum location for separation suppression. This finding is further illustrated in Figure 3.3 where the non-dimensionalized air velocity contours are compared for the investigated angles. The paper further states that the chordwise positioning of the blowing slot is more influential parameter in mitigating separation compared to the angle of blowing based on conducted C_L/C_D ratio evaluation for various blowing slot positioning and angles of blowing.

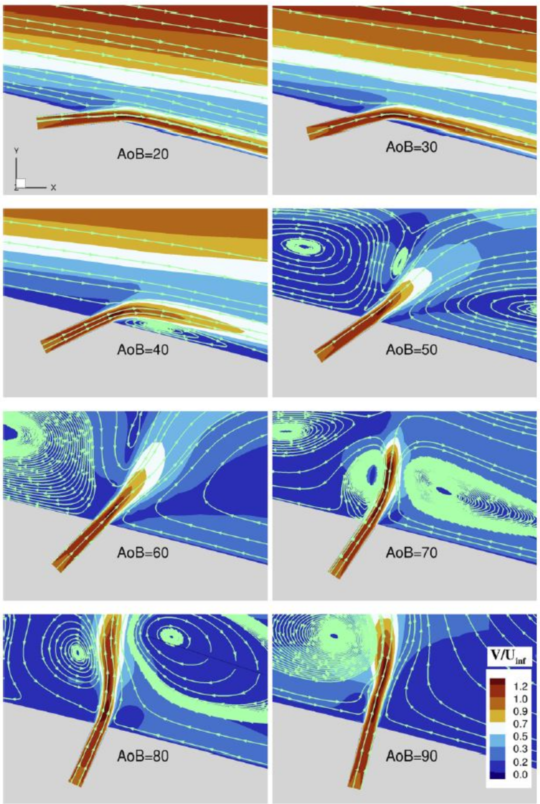

Figure 3.3: Angle of blowing (AoB) comparison at the midpoint of a wind-turbine airfoil at $Re = 3 \times 10^6$ [59]

A blowing angle of has been studied by other research papers involving steady or oscillating blowing near the leading edge of an airfoil with the purpose of maximizing separation control with an inscribed blowing slot in the geometry of the airfoil. For instance, Müller-Vahl et al. [54] investigates the steady blowing effectiveness through slots near the leading edge and mid-chord position on a NACA 0018 airfoil for quasi-static conditions for Reynolds number of up to $Re = 3.75 \times 10^5$ corresponding to freestream velocity of up to 16.7 m/s. The paper states that the jet angle is desirable to be minimized to obtain parallel jet of air to the wall surface. However, based on velocity field measurements, the jet is reported to be parallel to the wall surface at the selected 20 degrees, while further lowering the angle in that case has been limited due to structural considerations. Another example is the Puri et al. [60] paper which validates numerical results against experimental data for the effectiveness of steady blowing over NACA 0018 profile. The study uses RANS and implicit LES CFD approach to simulate the aerodynamic effect on the separation suppression for Reynolds numbers up to $Re = 2.5 \times 10^6$. Two blowing slots were implemented at the suction side of the airfoil with the upstream slot is reported to be positioned at the lip of the chord (x/c = 0.05) and designed to inject the air at 20 degrees relative to the airfoil surface. The study differentiates between a low and high value blowing coefficient case, namely 0.6% and 5%.

The 20 degrees jet with respect to the airfoil surface has also been implemented in Matalanis et al. [61] which studies the stall suppression capability of combustion powered actuators on a high-lift rotorcraft airfoil at high Reynolds numbers. A blowing angle of 22 degrees has been considered as tangential blowing by Matalanis et al. [50] and Kim et al. [49]. The Kim et al. [49] paper considers a tangential jet as 22 degrees with respect to the airfoil surface, while 80 degrees for normal to chord injection for comparison of their impact on stall suppression at the suction surface of an airfoil. The 22 degrees has been suggested as a practical limit for manufacturing. of the actuator. The outcome of the study is that the chord-normal jet negatively impacts the baseline aerodynamic performance by disrupting the external flow, while the tangential blowing shows effectiveness for suppression of both active and dynamic stalls. Additionally, the paper reports that based on three-dimensional simulations, the blowing slots with finite spans, may be less effective than continuous or two-dimensional slots. Moreover, it states that further research in required to better understand the 3D-effects of the finite span and skewed slots.

4

Propeller performance estimation

This chapter describes the methodology for estimating the performance of the used propeller in this project with the corresponding results. This is a required step that allows for the implementation of the influence of the propeller's operation on the flow field, and consequently the approximation of the separation point location, at the selected propeller-wing configuration in the later performed numerical analysis. First, the geometry of the propeller is specified, followed by the used software for performance estimation, and finally, the results that are implemented in the CFD analysis.

4.1. Propeller: TUD-XPROP

The selected propeller for this project is the TUD-XPROP propeller with the following specifications:

- Diameter: 406.4 mm
- Number of blades: 6
- Pitch at 70% of the radius: 45 degrees
- Spinning hub diameter: 92 mm

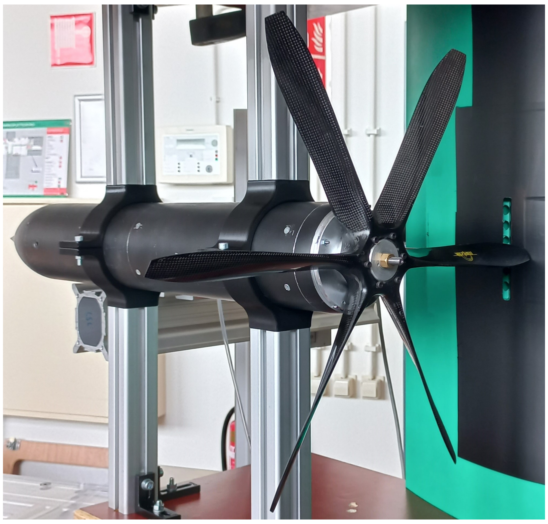

Figure 4.1: TUD-XPROP as part of the used experimental setup in this project

The propeller's radial chord length and twist distribution is further specified in Appendix B. The blade geometry is illustrated in Figure 4.2. Normally, propellers optimized for isolated (unducted) operation minimize the chord length at the tip such that the formation of tip vortices, and hence the tip losses, is also minimized. The selection of the TUD-XPROP propeller is an attractive choice for the purpose of this study due to its squared rather than rounded tip making it suitable for maximizing the propeller loading towards the tip and hence, the total pressure jump produced. Further details about this propeller are provided as a technical drawing attached to this document as a supplemental material.

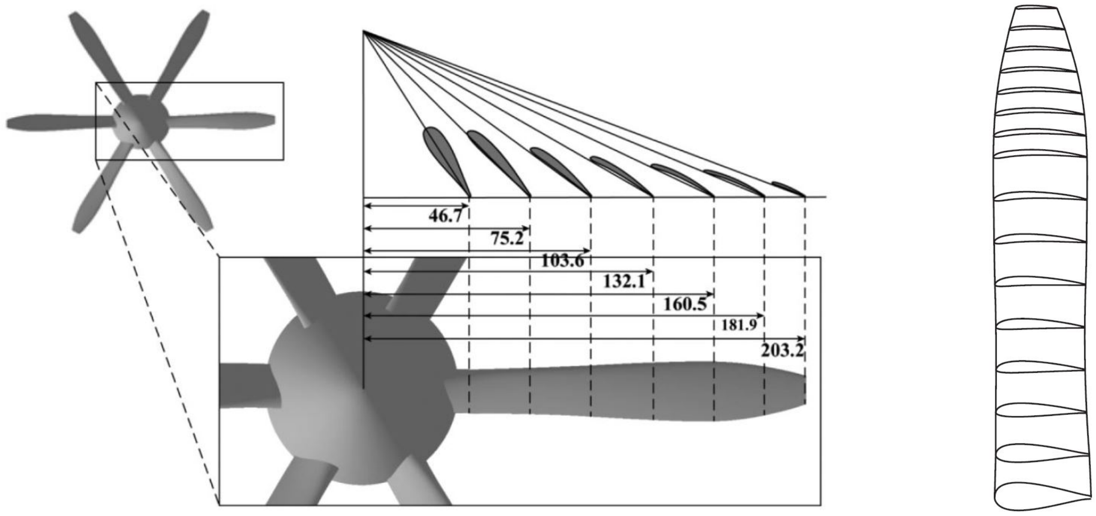

(a) Propeller layout [62]

(b) Untwisted blade geometry [63]

Figure 4.2: TUD-XPROP blade geometry references

As the specific airfoil names of the cross-section distribution of the blade geometry have not been found in the open literature, the distribution has been approximated based on the illustrations provided in Figure 4.2. Hence, the exact polar data for coefficient of lift and drag with respect to the angle of attack might differ from the real propeller's geometry. Considering the illustrations of the blade's geometry on Figure 4.2, the propeller's blade has been selected to be represented by the following airfoil selection also displayed on Figure 4.3:

- Clark-Y airfoil: 0-60% of the blade span; Re = 50 000
- E193 (10.22%) airfoil: 60-80% of the blade span; Re = 75 000
- ARA-D 6% airfoil: 80-100% of the blade span; Re = 60 000

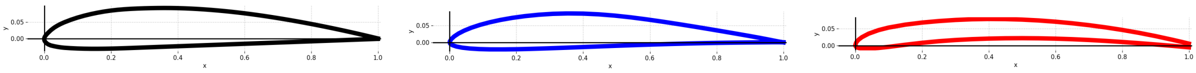

(a) Clark-Y airfoil [64]

(b) E193 (10.22%) airfoil [65]

(c) ARA-D 6% airfoil [66]

Figure 4.3: Selected airfoils for propeller blade geometry

The choice of the airfoils is elaborated further in the document.

4.2. Propeller performance analysis

The propeller performance at the selected operating conditions is estimated by performing a BEM analysis based on the approximated blade geometry. These points are further described as follows.

4.2.1. BEM

The performance of the propeller is estimated based on Blade Element Momentum (BEM) theory. It estimates the thrust produced by a propeller by dividing each blade into several small sections, known as blade elements. Each element is treated as an independent two-dimensional airfoil, allowing aerodynamic forces to be calculated based on its local operating conditions. By summing the contributions of all these elements, the overall performance of the propeller can be obtained. The theory also accounts for variations in airfoil shape, chord length, and pitch along the blade. [8]

BEM has first been developed by the Polish scientist Stefan Drzewiecki with the basic version, known as blade element theory (BET), introduced between 1892 and 1920. He has published this in 1920 in his book Théorie Générale de L'Hélice (General Theory of Helixes). This early theory ignored the influence of the induced velocity inside the propeller's slipstream, which is higher than the freestream velocity. This discrepancy alters the effective angle of attack, leading to errors in thrust predictions. The theory was subsequently refined by Albert Betz and Hermann Glauert, who incorporated the effects of induced velocity using the Rankine–Froude momentum theorem. This extended version is known as Blade Element Momentum Theory (BEM). [8]

BET offers several advantages over simple momentum theory. It allows variations in chord, pitch, and airfoil properties along the blade span to be analyzed. It also enables estimates of torque and power, incorporates nonlinear aerodynamic effects (such as those on lift and drag), and can predict propeller efficiency—all of which make it a popular tool in propeller design. However, BET assumes an undisturbed streamtube, making it less accurate under significant flow distortion (e.g. blockage effects). It simplifies aerodynamic forces to two-dimensional analyses, ignoring spanwise flow that can occur with large pressure gradients along the blade. It also assumes steady-state operation and cannot capture unsteady effects like thrust lag under rapidly changing RPM. In addition, the basic theory assumes rigid blades and neglects aeroelastic behavior. Finally, empirical corrections must be applied near the hub and tip to account for reduced lift and skewed inflow at high angles of attack. [8]

Figure 4.4a shows a single blade element of a propeller blade, defined with a certain thickness dr and at radial location from the rotation center (hub). Figure 4.4b, on the other hand shows the 2D airfoil cross-section of the blade element along with the corresponding aerodynamic forces. The shown variables are as follows:

- $c(r)$: Local chord length
- R_p: Propeller radius
- r: Arbitrary distance from rotation center
- Ω: Angular velocity
- V_∞: Freestream velocity
- ω: Local induced velocity by the element
- V_R: Resultant velocity, defined as $V_R = \sqrt{V_\infty^2 + (\Omega r)^2}$
- V_e: Effective resultant velocity, defined as $V_E = \sqrt{(V_\infty + w)^2 + (\Omega r)^2}$
- α: Local angle of attack
- α_i: Induced angle of attack from the induced velocity, defined as $\alpha_i = \sin^{-1}(w/V_R)$
- α_{ZL}: Zero-lift angle of attack
- β: Pitch angle: Defined as the angle between the chord line and the plane of rotation
- ϕ: Helix angle: Defined as $\phi = \tan^{-1}(V_\infty/(\Omega r))$

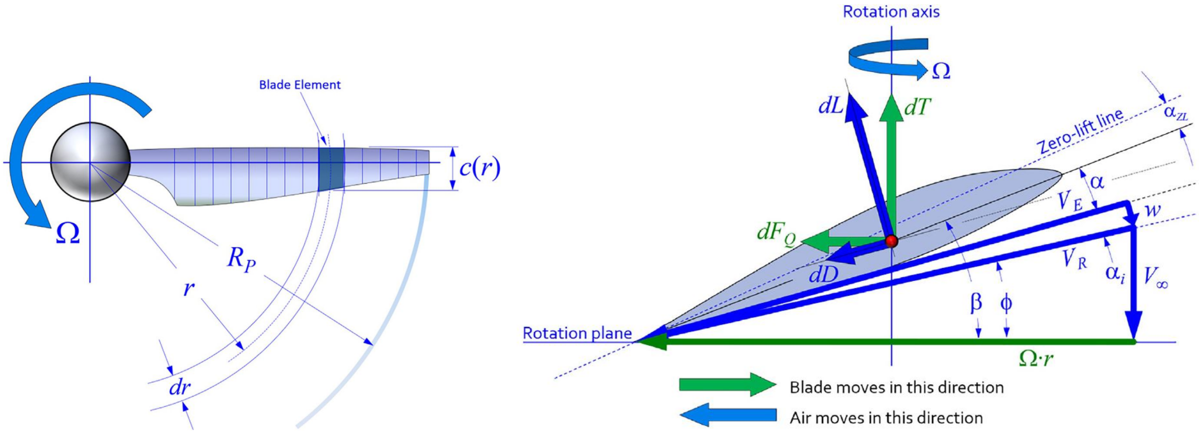

(a) Blade element

(b) Blade station 2D airfoil cross-section

Figure 4.4: Blade Element Momentum Theory (BEM) definitions [8]

The resulting local lift (dL), drag (dD), thrust (dT), and torque (dQ) are defined as:

$$dL = \frac{1}{2}\rho V_E^2 \cdot c(r) \cdot C_l \cdot dr \tag{4.1}$$

$$dD = \frac{1}{2}\rho V_E^2 \cdot c(r) \cdot C_d \cdot dr \tag{4.2}$$

$$dT = dL\cos(\phi + \alpha_i) - dD\sin(\phi + \alpha_i) \tag{4.3}$$

$$dQ = r \cdot dF_Q = r[dL\sin(\phi + \alpha_i) + dD\cos(\phi + \alpha_i)] \tag{4.4}$$

4.2.2. Prandtl Tip Loss Correction

A tip loss is normally described as a kinematic and/or dynamic difference between the 2D and 3D lifting device configuration. For an isolated propeller, the produced lift diminishes towards the tip due to the 3D flow effect of equalizing the pressure from suction and pressure side at the blade's tip. The lift for any lifting surface goes to zero at the tip. A correction of the lift loss towards the tip has been developed by Ludwig Prandtl. This correction has been implemented in BEM analysis for the case of a wing and a propeller blade in the beginning of the 20th century. The latter has been introduced as a correction to the Betz optimal circulation, allowing the Betz result to be applied not only for infinite but finite number of blades. The most common version of the Prandtl's tip loss correction integrated in the most BEM codes is the one suggested by Glauert. [67] Furthermore, Prandtl's tip loss correction has also been extended to include the lift loss at the hub of the propeller, where root vortex is formed due to the rapid decrease of circulation. [16] [4] The hub- and tip correction are expressed as follows, where N_B represents the number of blades:

- Hub correction:

$$F_{hub} = \frac{2}{\pi}\cos^{-1}\left(e^{-P_{hub}}\right) \quad \text{with} \quad P_{hub} = \frac{N_B}{2}\frac{r - R_{hub}}{r\sin\phi}. \tag{4.5}$$

- Tip correction:

$$F_{tip} = \frac{2}{\pi}\cos^{-1}\left(e^{-P_{tip}}\right) \quad \text{with} \quad P_{tip} = \frac{N_B}{2}\frac{R - r}{r\sin\phi}. \tag{4.6}$$

The resulting correction is expressed as:

$$F_P = F_{hub} \cdot F_{tip} \tag{4.7}$$

The correction is a function of the radial position and ranging between 0 at the hub and tip to a value close to 1 at the mid-span of the blade. [4] In case a surface is present in a proximity of the blade tip, the tip loss is suppressed. This allows for taking the assumption that the produced thrust, and therefore, pressure jump at the tip of the propeller blade is estimated considering purely by the 2D section aerodynamic properties. As the proximity between the wing and the propeller blade tip is intended for investigation of a flow towards ducted propeller configuration, the Prandtl's tip loss correction has been ignored when estimating the propeller's pressure jump at the selected operation setting.

4.2.3. Software used

Comparison is made between the predictions of two solvers - Qblade and JavaProp. BEM analysis has been employed for both cases with ignored Prandtl tip loss correction such that the duct presence at the tip is considered. The software details are as follows:

- **Qblade:** The QBlade software is an open-source graphical user interface (GUI)-based design and simulation tool for horizontal- and vertical-axis wind turbines (HAWTs and VAWTs), developed at TU Berlin. Its rotor aerodynamic computations rely on BEM theory, double-multiple streamtube theory (DMST), and free-wake vortex methods. It features structural dynamics analysis option using a corotational multibody formulation with Bernoulli beam elements. In addition, turbine supervisory controllers can be integrated into simulations through a set of library interfaces. Hydrodynamic modules for both floating and fixed offshore platforms are also under development. [68]

Furthermore, QBlade integrates XFOIL for airfoil polar extrapolation, making it a popular tool in wind energy education at numerous universities worldwide — including TU Berlin, HTW Berlin, HS Flensburg, DMU Leicester, Texas Tech University Lubbock, and DTU, and others. Its global user base spans Europe, USA, Brazil, and India. The propeller blade is defined by the user via airfoil selection, chordlength, and twist at corresponding spanwise stations. The software interpolates the aerodynamic properties of the airfoils between the stations (i.e. over a blade element). [68] [69]

- **JavaProp:** JavaProp is a software dedicated to propeller and wind turbine performance. The aerodynamic analysis is based on BEM method coupling the 2D airfoil characteristics with momentum considerations. It is suitable to both aeronautical and marine applications. [70]

  The propeller blade is defined by importing the blade chordlength and twist at specific blade locations. The solver interpolates the geometry over the blade elements. A limitation is that JavaProp sticks to a definition of blade in steps of r/R = 0.05, preventing more accurate geometry definition. Airfoil selection can be made at four pre-defined locations: r/R = 0.0, 0.333, 0.667, and 1.0.

4.3. Results

The operational setting of the propeller is set such that the stall angle of attack is not exceeded at any blade location, while still maximizing the thrust produced. This way the added kinetic energy to the flow by the propeller would also be maximized, and therefore, the captured slipstream dynamic pressure by the inlet of the passive flow control design, described further in chapter 6. Based on the BEM analysis by Qblade, the thrust for the approximated TUD-XPROP propeller geometry is maximized at advance ratio of about 1.3. However, the angle of attack distribution predicted by JavaProp shows a deviation from the Qblade prediction towards the tip region of up to 2 degrees. Hence, a conservative selection is made with advance ratio of J=1.4 for this project allowing the predictions of both software to be below the stall angle of attack, which happens at the tip of the blade, where the ARA-D 6% airfoil has a stall angle of attack of 10 degrees at the estimated local Reynolds number. Figure 4.5a shows the comparison of both software prediction for the angle of attack distribution at J=1.4. The freestream velocity is selected considering the capabilities of the wind-tunnel where the experimental validation would be performed, while still maximizing the Reynolds number in the test-section, consequently minimizing the boundary layer thickness. Hence, the value for the freestream velocity is selected to be 20 m/s. Based on Equation 2.1, this results the rotational speed of the propeller to be 2109 RPM.

The local Reynolds numbers are calculated for the 3 pre-defined by JavaProp radial positions, that are outside the spinning diameter. These locations are r/R = 0.333, 0.667, and 1.0. The local tangential velocity (v_t) is calculated considering the radial distance multiplied with the angular velocity, expressed in the following equation:

$$v_t = \text{RPM} \cdot \frac{2\pi}{60} \cdot \frac{r}{R} \cdot R \tag{4.8}$$

and the local velocity magnitude as:

$$v_{local} = \sqrt{v_\infty^2 + v_r^2} \tag{4.9}$$

Considering standard atmosphere conditions for the air density ($1.225\ kg/m^3$) and dynamic viscosity ($\mu = 1.79 \times 10^{-5}\ kg/m \cdot s$), the local Reynolds number are obtained to be 51 600, 75 500, 62 300 for r/R = 0.333, 0.667, and 1.0 respectively using the following equation:

$$Re_{local} = \frac{\rho \cdot v_{local} \cdot c_{local}}{\mu} \tag{4.10}$$

Since accurate selection of the local Reynolds number in this case is not possible in JavaProp, the closest option of selected airfoil with available Reynolds number combination is chosen, leading to using Re = 25 000, 100 000, and 50 000 for the r/R = 0.333, 0.667, and 1.0 radial positions respectively.

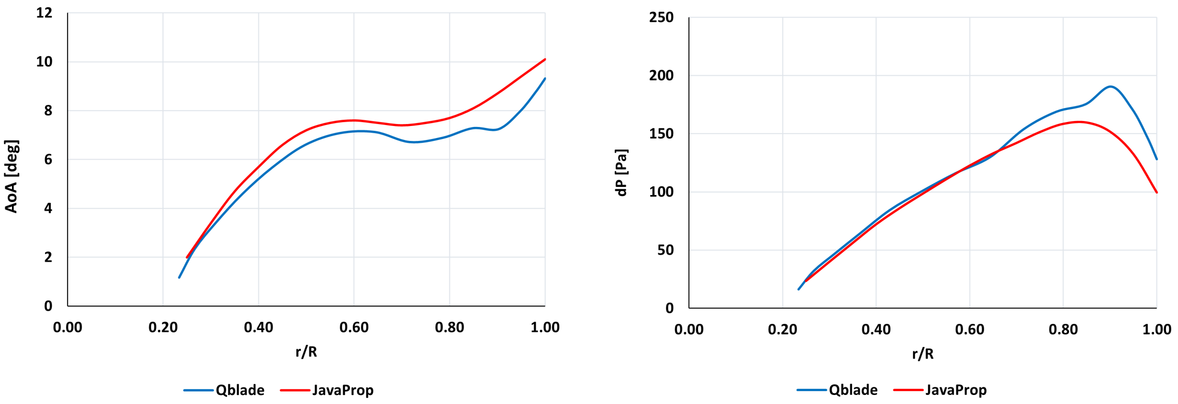

(a) Angle of attack comparison

(b) Pressure jump comparison

Figure 4.5: Comparison of predictions between Qblade and JavaProp solvers for the propeller performance at J=1.4

Looking at Figure 4.5b, the pressure jump predictions by the two solvers show a good match up to r/R = 0.65, where they start diverging from each other. The largest margin occurs at about r/R = 0.90 with a difference of roughly 40 Pascals, while the difference at the tip is estimated to be about 30 Pascals. The reason for the disagreement of the two solvers could be based on the different approximation accuracy of the blade geometry. JavaProp allows the local airfoil section to be defined only at 4 pre-defined spanwise locations, as stated in subsection 4.2.3, while interpolation is done for the intermediate regions. However, the number of the locations in Qblade is possible to be set as needed. The original blade's local geometry parameters distribution of r/R, chord length, and twist angle is simplified by the JavaProp solver. The original number of locations where the blade geometry is specified is 26, as provided in Table B.1 in Appendix B. JavaProp simplifies this geometry by reducing the original locations to 16 instead. Hence, the propeller blade is specified in 16 spanwise locations in Qblade as well for keeping consistency. The used blade geometry in both Qblade and JavaProp solvers is then as defined in Table B.2. The airfoil distribution along the blade, presented in section 4.1, is selected based on the available airfoils in the JavaProp solver.

As the total pressure jump is not a direct output from the BEM calculation with Qblade, it is extracted from the normal force radial distribution. The local normal force per unit span (F_n in N/m) is multiplied by the radial blade thickness between the given and the previous radial distance. Then the result is multiplied by 6 to account for the total local contribution of the 6 blades, which gives the thrust produced at the current radial location. The local total pressure jump at the given radial position is then obtained by division of the calculated local thrust by the annular area of the rotor disc enclosed by the given and previous radial position as displayed in Equation 4.11:

$$\Delta p_i = \frac{\Delta T_i}{\Delta A_i} = \frac{B \times F_n(r_i)\,\Delta r_i}{\pi\left(r_i^2 - r_{i-1}^2\right)}. \tag{4.11}$$

Interestingly, integrating the direct output from JavaProp for the total pressure jump distribution over the propeller disc area gives inconsistent result with the total thrust value output. Hence, the pressure jump from JavaProp plotted in Figure 4.5b is extracted from the coefficient of thrust distribution over an annular area of the disc ($dC_t/d(r/R)$). However, as the local Reynolds number could be more accurately specified with Qblade, the Qblade total pressure jump has been further considered in the analysis. The BEM simulation output is defined where data for the local airfoil polar data are known. Hence, no data is available for the hub region of the propeller. As the used numerical analysis software requires the resulting total pressure jump to be imported via a function instead of discrete data points, the estimated performance is approximated by a polynomial curve fit as shown in Figure 4.6.

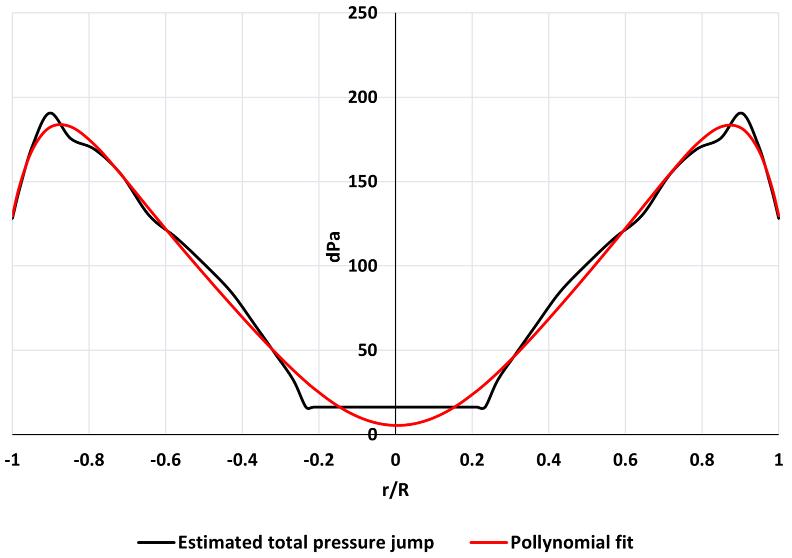

Figure 4.6: Total pressure jump distribution at J = 1.4 used in the numerical analysis

Since no data is available for the hub region, the pressure jump distribution at this location is considered constant for simplicity with the same value as at the closest point analysed by the BEM method, which is at r/R = 0.2 equal to 16 Pa. The pressure jump in the hub region is expected to drop significantly due to the symmetrical shape of the hub, creating practically no pressure jump. Hence, despite the deviation of the polynomial fit and the selected pressure jump at the hub, the fit is considered reasonable to be further used in the numerical analysis. Furthermore, the pressure jump at the hub is expected not to have a substantial influence on the region of interest for this study.

5

Numerical analysis

Performed are Computational Fluid Dynamics (CFD) simulations on a 2D domain with the purpose of designing the experimental test setup and including estimation of the approximate location of the separation point on the wing's surface in a range of angles of attack. This is further used for identification of the required angle of attack for triggering flow separation near the leading edge of the wing, serving as a representation of a duct's lip flow separation phenomenon. This chapter begins with description of the airfoil smoothing procedure, the domain size and the selection of the boundary conditions. Then, the mesh definition is provided, followed by the presentation and discussion of the main results.

5.1. Airfoil contour smoothing

The original X400 flap airfoil coordinates considered for this thesis project are reported by van Egmond [71]. A performed XFOIL study of the original coordinates shows spikes/irregularities in the resulting pressure coefficient distribution. Savitzky-Golay (savgol) filter is employed to smoothen the coordinates and hence, the pressure distribution. The filter is commonly used in preprocessing in spectroscopy and signal processing. "For a given signal measured at N points and a filter of width (w), savgol calculates a polynomial fit of order (o) in each filter window as the filter is moved across the signal." [72] The filter's estimate at each window's center is evaluated by the polynomial fit at the central point. Hence, the window size is beneficial to be an odd number. The filter functions when the window size (number of measurements) is greater or equal to the parameters to be estimated, i.e $w \geq$ (o+1). Smoothing is achieved if the width is greater than (o+1) and no smoothing is present if w = (o+1). As the filter width increases, greater smoothing is achieved and hence, the peaks are suppressed. [72]

Investigated were several combinations of window size and polynomial fit with the goal of maximally preserving the original pressure distribution of the original contour, while also minimizing the present spikes. After iterative process, the combination meeting these requirements has been found to be:

- Filter width = 11
- Polynomial order = 3

Therefore, the used airfoil coordinates for the rest of this research, provided in Appendix A, are resulting from these filter settings. The comparison between the original and smoothened pressure distributions is provided in Figure 5.1, while additional XFOIL plots with other analyzed filter settings can be also found in Appendix A.

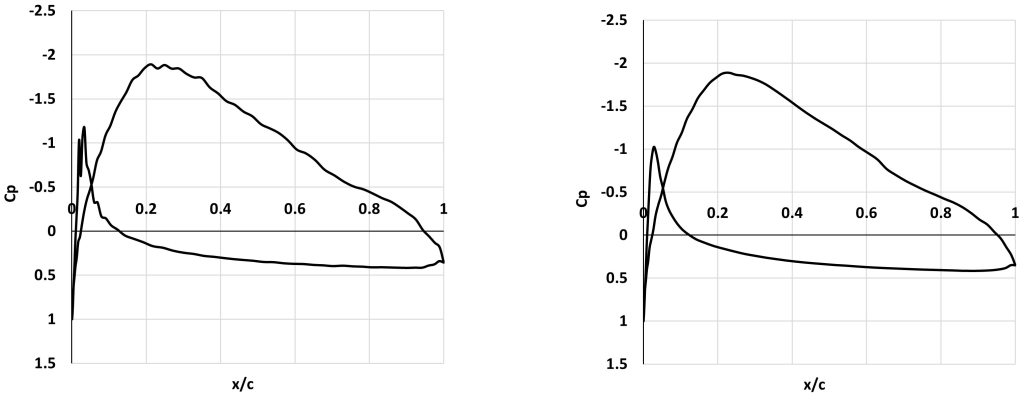

(a) Original coordinates

(b) Smoothed distribution: Savgol filter with w = 11, o = 3

Figure 5.1: Cp distribution comparison for AoA = 0 degrees in incompressible flow, Re = 400 000

5.2. Domain size and boundary conditions

The computational domain defines the simulation region. The location where the boundary conditions are specified needs to be studied at which does not disturb the flow propagation. Increasing this distance to the object of interest reduces their disturbance effect. However, this distance should prevent increasing the domain size excessively leading to excessive computational power usage.[73] Following the examples for CFD studies involving ducted fan such as Dighe et al. [39] or baseline airfoil aerodynamic performance such as Jindal et al. [45], the inlet boundary condition is placed at 10 chord lengths of the duct. On the other hand, the outlet is located at 20 chord lengths downstream from the duct's leading edge. As the propeller is simplified by an actuator line, it is modeled by a fan boundary condition. [39]

The domain size is selected to represent to a high degree the conditions at the experimental wind-tunnel test setup, described in chapter 6, while considering the recommendations for boundary conditions spacing as indicated in Figure 5.2. The selected dimensions for performing the numerical analysis and corresponding boundary conditions are as follows:

- **Velocity inlet:** The width of the inlet is set to match the width of the test-section of the wind-tunnel setup. This dimension equals 900 mm.
- **Wing:** The wing is represented as the airfoil shape of its uniform cross-section. The used coordinates of the airfoil are provided in Appendix A The chord length used is set identical to the real wing model equal to 300 mm. The change of the angle of attack has been selected to be about a rotation point allowing at least half of the wing to be immersed in the flow for the majority of the angles of attack. This point has the coordinates of (0.15, 0.0244) with respect to the origin of the coordinate system placed at the leading edge of the wing.
- **Propeller:** Matching the used XPROP propeller's diameter of 406.4 mm. The propeller is represented by a fan boundary condition. This allows the estimated total pressure jump generated by the propeller to be defined along a line instead of explicitly resolving the rotating blades.
- **Outlet:** The outlet is positioned at 20 chord lengths downstream of the wing's leading edge.
- **Walls:** Both the wing and the wind-tunnel's test-section wall which the wing sticks out of are set to no-slip walls. The rest of the walls in the domain are set to free-slip walls.
- **Downstream wall opening:** A complete seal of the the test-section's wall where the propeller-wing assembly is intended to be installed is expected to induce substantial flow blockage which would restrict the shift of the separation point by the injected air from the blowing slot. To have a noticeable effect on the separation point, it is hypothesized that a large injection velocity from the blowing slot would be required and consequently large blowing coefficients. Therefore, to allow the separation point to be more easily impacted by the blowing jet's properties, a wall opening of 0.7 meters is selected between the suction side of the wing and the wind-tunnel's wall. This distance is selected as a trade-off between restriction of the freestream to stay mostly within the test-section, while the blockage effect is reduced.

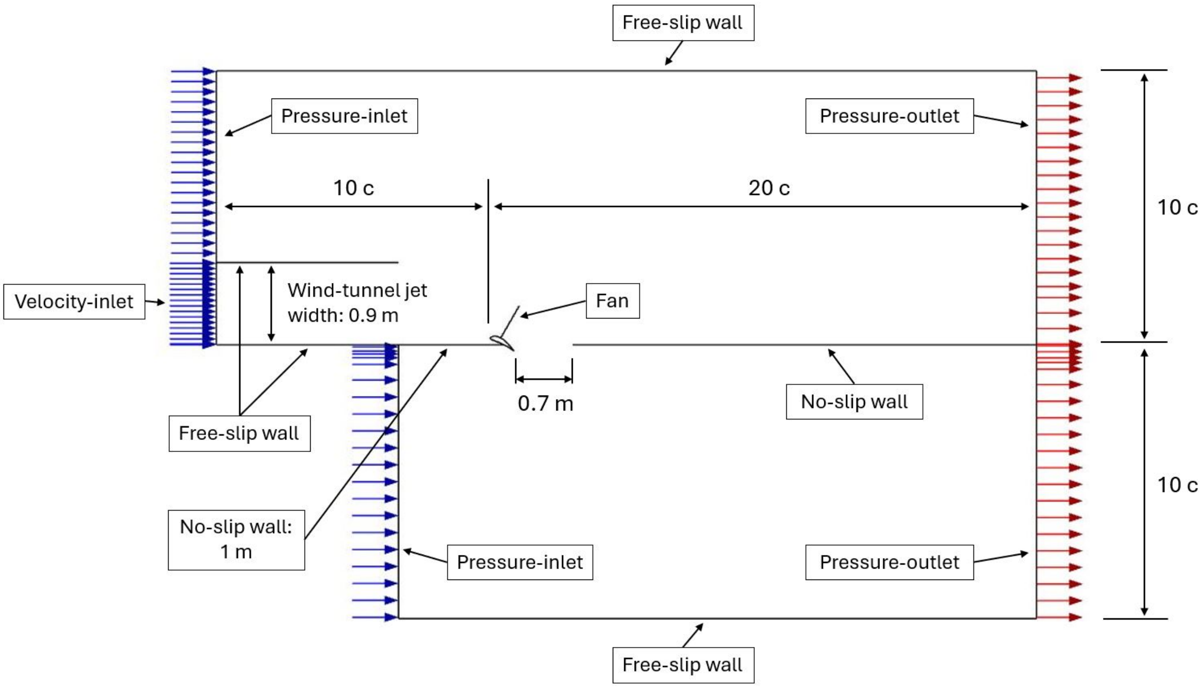

Figure 5.2: Domain size and boundary conditions

5.3. Computational mesh

A mesh is a division of a continuous geometric space into discrete topological and geometric cells, forming a simplicial complex. A simplicial complex consists of triangles, line segments, points, and their n-dimensional equivalents. [74] The two main types of computational mesh are *structured* and *unstructured*. An optimal structured mesh for complex geometries is more time-consuming to be created than an unstructured. This is caused by the requirement of a manual split of the domain in blocks and definition of their own properties. Moreover, an unstructured mesh offers a greater flexibility and automation. However, the structured mesh shows a superior accuracy for viscous calculations as it can handle cells with very high aspect ratio in the boundary layer. [73] The mesh for all simulations of this project are created by ANSYS ICEM CFD software.

The most famous relationship of turbulent flow near solid boundaries is the *law of the wall*. It is empirically-determined that the streamwise velocity of the flow near the wall varies logarithmically with the distance from the surface. To fully resolve the viscous sublayer of the boundary layer without the need of wall functions approximations, the normal distance (height *y*) of the first cell row at the walls of the object of interest should ideally match the dimensionless wall distance y^+ value of 1 of the *law of the wall* shown in Figure 5.3. [75]

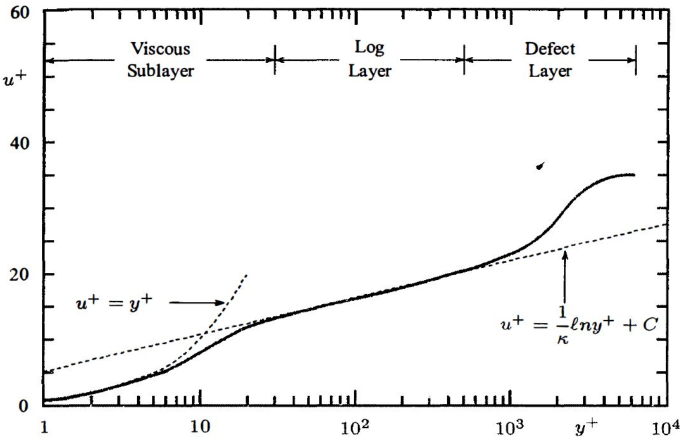

Figure 5.3: Typical turbulent boundary layer velocity profile [75]

where:

$$u^+ \equiv \frac{v_\infty}{u_\tau} \quad \text{and} \quad y^+ \equiv \frac{u_\tau y}{\nu} \quad \text{with} \quad u_\tau \equiv \sqrt{\frac{\tau_w}{\rho}} \tag{5.1}$$

Using the relation of coefficient of friction (C_f) and wall shear stress (τ_w), the height of the first cell is calculated for a given value of y^+ as [76][75]:

$$\tau_w = \quad \tfrac{C_f \rho v_\infty^2}{2} \quad \text{with} \quad C_f = 0.027 \cdot Re^{-1/7} \tag{5.2}$$

$$y = y^+ \sqrt{\frac{2}{C_f}} \frac{\nu}{v_\infty} \tag{5.3}$$

Standard atmosphere conditions are considered with total pressure of 101 325 Pa. The dynamic viscosity is obtained by the Sutherland's law [77]:

$$\mu = \mu_0 \left(\frac{T}{T_0}\right)^{3/2} \frac{T_0 + S}{T + S} \tag{5.4}$$

Where:

- $\mu_0 = 1.716 \times 10^{-5}$ is a reference value in kg/m·s
- $T_0 = 273.11$ K is reference temperature
- $S = 110.56$ K is Sutherland constant
- T is the static temperature in Kelvin
- μ is the dynamic viscosity in kg/m·s

Assuming ambient static temperature of 15 degrees Celsius (288.15 K) gives dynamic viscosity of $\mu = 1.79 \times 10^{-5}\ kg/m \cdot s$. As the freestream velocity is 20 m/s, and the chord length is equal to 300 mm, the resulting Reynolds number is approximated as Re = 400 000. After evaluating the coefficient of friction C_f, the first layer cells height for $y^+ = 1$ is $y = 1.58 \times 10^{-5}\ m$. The resulting computational mesh for the whole domain is presented on Figure 5.4 while the zoom-in image of the computational mesh at the propeller-wing configuration is shown in Figure 5.5.

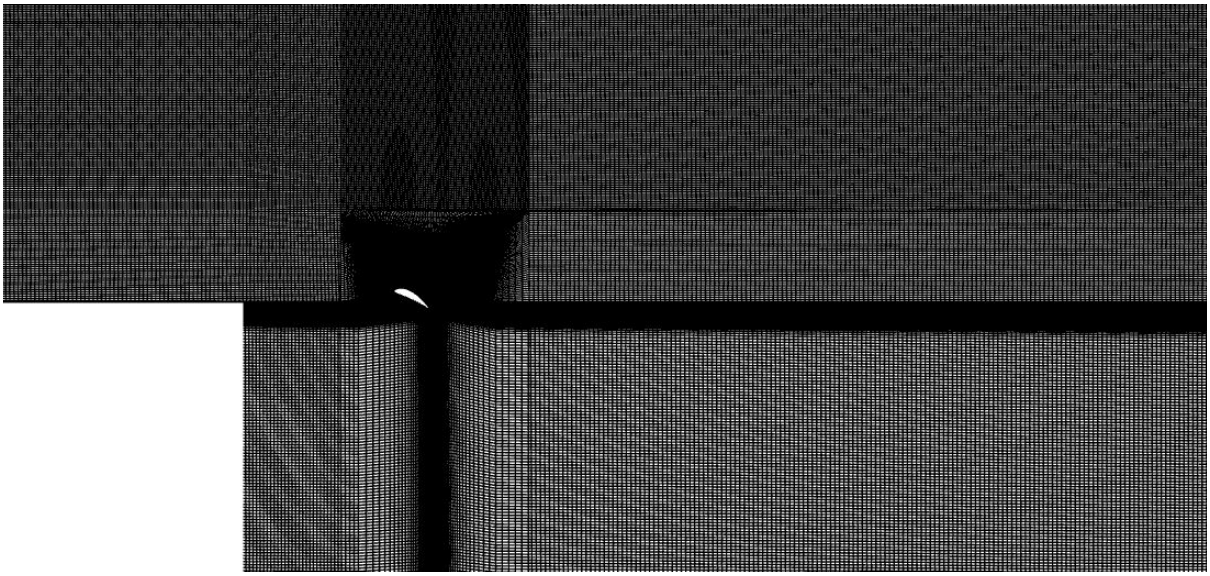

Figure 5.4: Computational mesh: Domain view

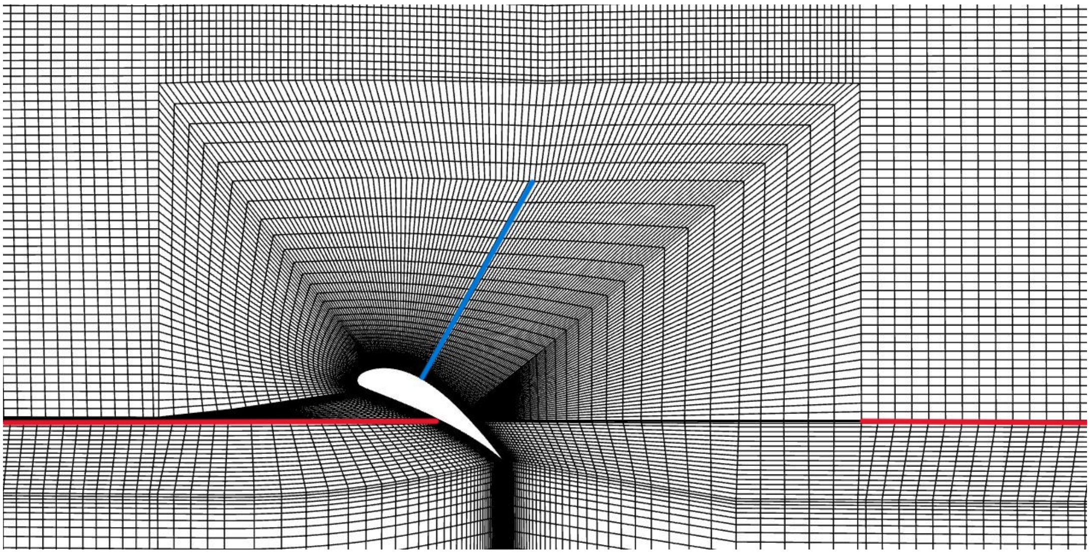

Figure 5.5: Zoomed-in mesh at duct-propeller configuration; Blue: Propeller pressure jump line; Red: Wind-tunnel walls

5.4. Turbulence models

A turbulence model is a mathematical model constructed and applied to predict the effects of turbulent flow. ”Despite the years of research, there is no single analytical theory explaining the evolution of turbulent flow, only equations, which can be solved directly for simple cases of flow”. [78] CFD studies involving prediction of adverse pressure gradients recommend three specific RANS turbulent models:

- Shear Stress Transport (SST) $k-\omega$ [39] [79] [26] [73] [80]: The SST $k-\omega$ model allows for a high-accuracy predictions of the onset and extent of flow separation, leading to a more precise representation of the flow. [73]
- Spalart-Allmaras [45] [81] [55] [41] [44]: This one-equation model predicts reasonably well the surface pressure distribution, separation bubble length, and separation onset. It performs as well as other RANS models such as SST $k-\omega$ model. [81]
- $k-\epsilon$ [18] [40]:The $k-\epsilon$ model shows ability to account for the effects of turbulent boundary layer history by solving the full transport equations for k and ϵ. Compared to algebraic models, it is more effective in predicting flow separation, which occurs when the airfoil stalls at high angles of attack. [40]

Following the recommendations of the found literature, the SST $k-\omega$ and Spalart-Allmaras turbulence models are selected for performing the numerical analysis in this project.

5.5. Results

All simulations in this project are performed with the pressure-based finite volume solver of ANSYS Fluent software. A converged solution has been considered when all the residuals are lower than 1×10^{-6} as recommended by Fatahian et al. [82]. Presented in Figure 5.6 and Figure 5.7 are the resulting contours of velocity magnitude at 30 degrees angle of attack, with higher velocity is depicted in red, while lower or stagnant air with blue color:

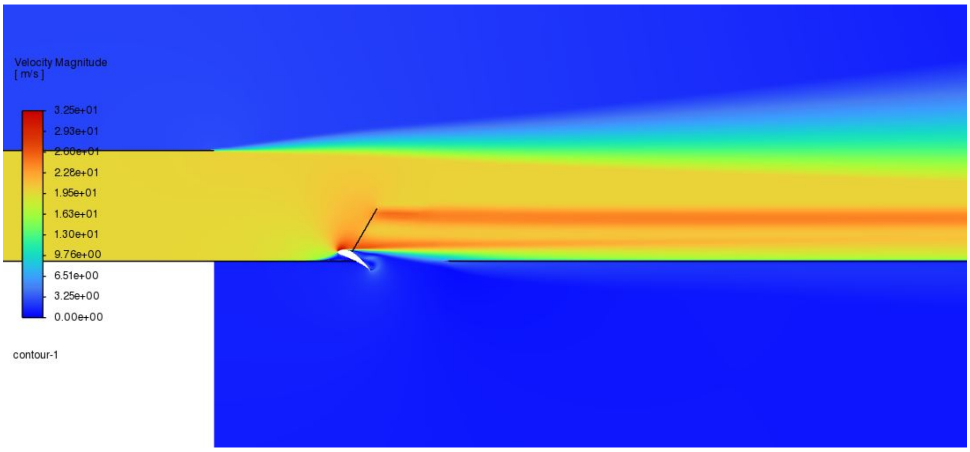

Figure 5.6: Domain view: Velocity magnitude at AoA=30 degrees, v_∞ = 20 m/s, SST $k-\omega$

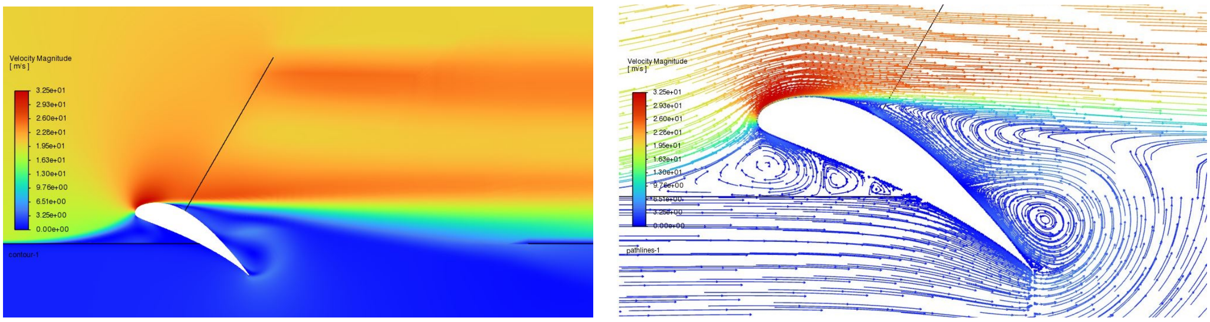

(a) Zoom-In: Velocity contour

(b) Zoom-In: Velocity pathlines

Figure 5.7: Zoom-In view: Velocity magnitude at AoA=30 degrees, v_∞ = 20 m/s, SST $k-\omega$

It is observed that at this condition, the flow over the wing is mostly separated and hence, not significantly impacting the main flow direction. The high-velocity flow remains overall within the wind tunnel's width while entraining the ambient air as it moves downstream. On Figure 5.7 is visible that the contact between the upstream wall with the pressure side of the wing prevents any upstream interaction of the jet and ambient air behind the wall, causing the formation of air stagnation area inducing flow blockage. The downstream wall opening, on the other hand, allows the ambient flow to be impacted by the flow in the test section. Looking specifically at the velocity magnitude pathlines on Figure 5.7b, it can be seen that this configuration causes a suction area downstream of the wing, causing the ambient air to enter the test-section. This is due to the resulting static pressure difference between the two flow areas, forcing airflow from the high static pressure area (the ambient air) to the low static pressure air inside the test-section, creating recirculating flow structure around the trailing edge of the wing. The ambient air flowing into the test-section matches the freestream flow direction with increasing distance from the wing's surface.

To quantify the effect of the computational mesh density on the results deviation, a mesh convergence has been performed on the shown case. The criterion for the convergence is the separation point, evaluated by the location where the wall shear stress distribution becomes zero over the suction surface of the wing. Another indicator for a separation point would be looking at the pressure distribution over the wing and indicating where the pressure gradient becomes zero after a certain point (i.e. the pressure distribution becomes flat). However, in this case, an operating propeller is present in close proximity inducing a pressure jump over the suction side of the wing and hence, assumed to alter the true separation location. Instead, the method for finding the separation point precisely is by indicating the location over the suction surface of the wing where the wall shear stress reaches zero. As the flow in the analyzed setup has a complex development as visible in Figure 5.7b, it is characterized by multiple locations where the stress becomes zero. These locations correspond to local recirculating structures within the separated region due to the unsteady flow over the suction wing surface. Hence, the separation point is estimated based on the closest point to the leading edge where the wall shear stress is zero. Figure 5.8

shows the x-wall shear stress on the suction side of the airfoil by the mesh convergence study.

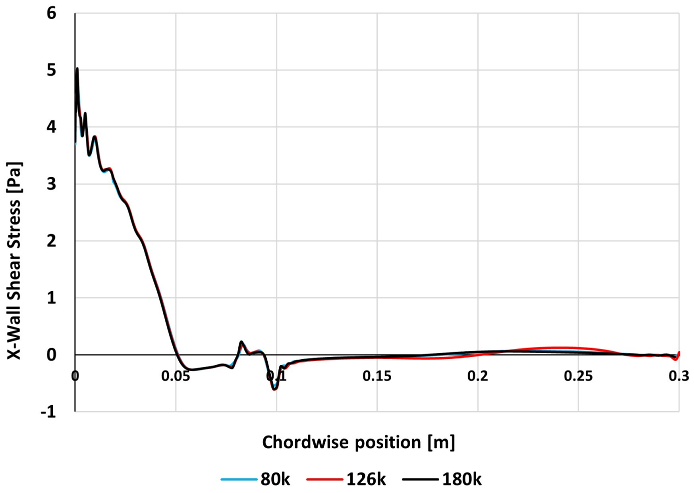

Figure 5.8: X-wall shear stress predictions on the suction surface of the airfoil by the mesh convergence study performed at v_∞ = 20 m/s and AoA=30 degrees, SST $k - \omega$

It is observed a good match of the predictions of the three mesh densities for the x-wall shear stress distribution. It can be indicated that the first location where this stress becomes zero is about 0.05 meters from the airfoil's leading edge at these conditions. The value for the stress then fluctuates until reaching the propeller location at 0.1 meters from the leading edge then stays roughly zero until the trailing edge of the airfoil. The regions where the stress is negative correspond to a flow going in reverse (upstream) direction, while the positive - downstream. Based on the plot, it can be concluded that the flow structures result in upstream flow direction just downstream of the separation point, while the airflow downstream of the propeller shows stagnant behavior. Presented on Table 5.1 are the predictions of the separation point by the selected three mesh sizes:

Table 5.1: Mesh convergence data

Mesh type	Zero wall shear-stress chordwise location
Coarse (8×10^4 cells)	0.0520 m (x/c = 0.1732)
Medium (1.3×10^5 cells)	0.0512 m (x/c = 0.1707)
Fine (1.8×10^5 cells)	0.0506 m (x/c = 0.1686)

Looking at the data, it can be concluded that all meshes give similar results. More precisely, the coarse mesh shows the largest deviation of 1.4 mm with respect to the fine mesh. This value, however, drops to 0.6 mm for the medium mesh. As the accuracy of the separation point converges to a value of approximately 0.051 m from the leading edge, the medium mesh is hence selected for the rest of the numerical study as it shows a good trade-off between accuracy and computational resources. The separation point on the real wing is also impacted by factors such as surface roughness and flow blockage effects from the experimental setup installation which are ignored in this case for rough approximation. Despite this, the medium mesh is assumed to be reasonable choice for this goal.

Additionally, the resulting stress fluctuations at the leading edge are hypothesized to be due to not sufficient smoothing of the airfoil. Hence, performed is the same simulation conditions for larger filter width but maintaining the polynomial order as default. The results are displayed on Figure 5.9.

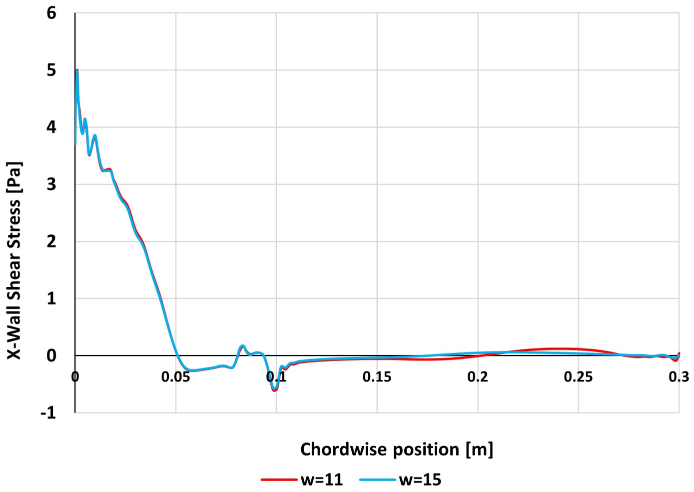

Figure 5.9: X-wall shear stress smoothening comparison with different savgol filter widths, AoA = 30 degrees, SST $k - \omega$

It can be concluded that the stress fluctuations near the leading edge are not affected noticeably by the further smoothening of the airfoil. However, a noticed difference of the smoothening effect is the dampening of the stress fluctuations past the half chord-length for the w = 15 case. This suggests that smoothening of the used coordinates could affect the stress distribution noticeably. However, as even further smoothening leads to a strong deviation form the pressure distribution of the original airfoil as shown in Appendix A, the x-wall shear stress distribution over the suction surface of a further smoothened airfoil has not been analyzed. It is hypothesized that a significant smoothening method would be required to dampen the leading edge stress fluctuations of the used coordinates.

To assess the effect on the flow by varying the distance (bleed size) between the wall and the pressure side of the wing, three upstream bleed sizes have been studied as well. The sizes are selected with a step equal to the separation region thickness at the propeller location at the case where no upstream bleed is present, as shown in Figure 5.7. The CFD data shows that this thickness is 25 millimeters. Hence, simulations were performed with upstream bleed size of 25, 50, and 75 millimeters. Figure 5.10 shows the velocity contours corresponding to the three scenarios for angle of attack 30 degrees.

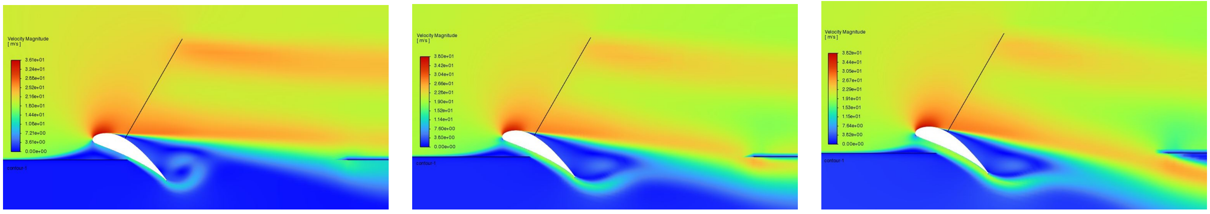

(a) 25 mm **(b)** 50 mm **(c)** 75 mm

Figure 5.10: Upstream bleed size effect on the flow development while the propeller is active

Analyzing the velocity contours, it can be concluded that the propeller slipstream is noticeably affected by the upstream wall opening size. At 25 millimeter opening, the flow blockage still prevails as the allowed freestream velocity to pass between the wing and the wall still recirculates around the trailing edge. With already 50 millimeter opening a higher-velocity flow from the pressure wing side directly merges with the higher velocity from the propeller slipstream at downstream stage. This encloses a separation region over the suction side of the wing. With the maximum opening of 75 millimeters, significant portion of the high velocity flow is redirected outside the wind-tunnel's test section, while the stagnation air upstream the wing is almost removed. Furthermore, as the propeller slipstream is further deflected towards outside the test-section it aligns better with the wing's orientation, allowing the increase of the flow attachment distance over the suction surface, and hence, the flow separation point is pushed downstream towards the propeller and consequently the flow separation region is further reduced.

To assess the position of the separation point at lower angles of attack and the upstream bleed size effect, performed are similar simulations for 20 and 25 degrees as well. Figures showing the velocity contours for these are provided in Appendix C. Figure 5.11 shows the data for estimation of the separation point from both used turbulent models, where the chordwise location of the propeller is indicated by a black line and the wing's cross-section is shown for reference:

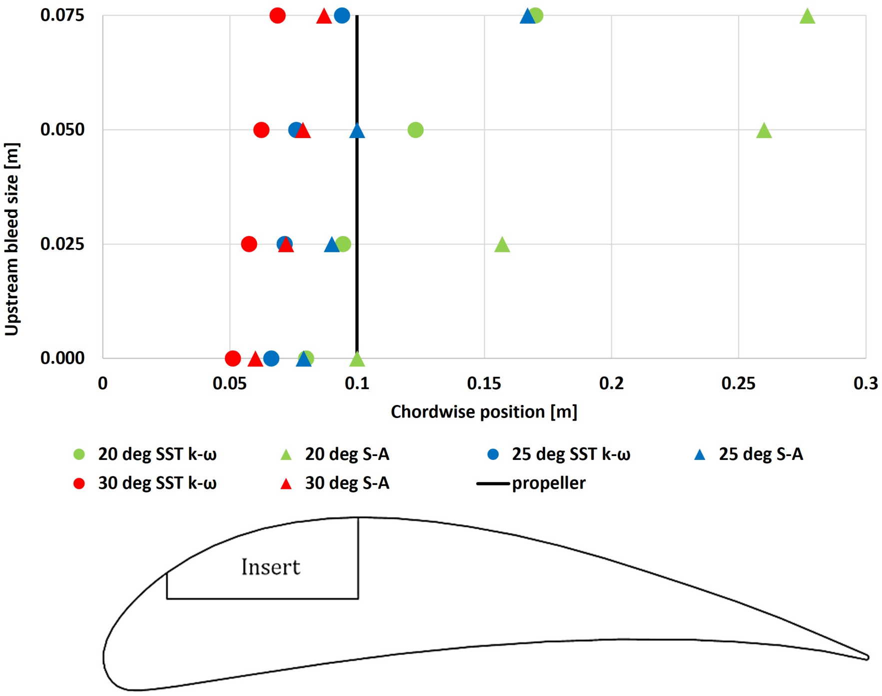

Figure 5.11: Comparison of the separation point data prediction by SST $k - \omega$ and S-A turbulent models for varying upstream bleed sizes at v_∞ = 20 m/s

Generally, it is indicated that decreasing the angle of attack causes the separation point to shift downstream compared to the 30 degrees case. This is expected as the adverse pressure gradient at lower angles is decreased, allowing the flow to stay attached up to a later chordwise position. It is further observed that the prediction of the two models differs quite drastically with increasing the distance between the upstream wall and pressure side of the wing. The closest difference has been achieved for the case where the upstream wall touches the wing with the smallest chordwise margin of 10 mm for the case of 30 degrees angle of attack, indicated by red color. This difference grows to roughly 20 mm for the largest upstream opening simulated. The second closest difference is shown by the 25 degrees case where, again, the closest margin is about 15 mm at zero distance between the wall and the wing, while growing to roughly 70 mm for 75 mm opening. And lastly, the strongest disagreement in the plotted data is presented by the lowest analyzed angle of 20 degrees. The lowest margin in this case is 25 mm, while growing to 110 mm. Overall, it is observed that the SST $k - \omega$ turbulent model always predicts the zero shear stress to be reached earlier for all investigated cases, and hence, earlier flow separation. This indicates further that the offset between the wing and the upstream wall should be a crucial factor for the boundary layer development of this propeller-wing configuration.

It is apparent that the uncertainty of the separation point can become extreme for a non-zero opening. Based on the results in Figure 5.11 the upstream wall opening should be minimized so that the confidence in the separation location is maximized. The 30 degrees angle of attack case with no upstream opening, as expected, results in the earliest separation point as the effect of the flow blockage induced by the wall contact is the strongest, consequently reducing the wing's effective contour. This case also represents a condition where the separation point is within the boundaries of the insert part of the wing, while also providing upstream distance for a the blowing slot to be designed in the same part. Furthermore, the separation point in this case is also not too close to the propeller, which allows for a better investigation of the effectiveness of a blowing slot with certain blowing coefficient. Hence, the blowing slot location is selected to be designed at 50 millimeters from the leading edge, such that it is just upstream of the separation point at the highest investigated angle of attack.

The wall shear stress is a dimensional parameter resulting from the fluid-wall friction force. Instead, it is non-dimensionalized by the dynamic pressure obtaining the coefficient of friction C_f. The C_f distribution is plotted as additional material in section C.3 for all simulated angles and cases. It can be observed that, at lower angles of attack the weaker adverse pressure gradient delays boundary layer separation, causing the friction coefficient to reach zero Pascals further downstream. The suction peak at lower angles is reduced, leading to a more gradual pressure recovery and hence a weaker adverse pressure gradient. In case the boundary layer is attached to the full suction side length, the C_f remains non-zero until the trailing edge.

The velocity profile shown in Figure 5.12 upstream the separation point is used to estimate the boundary layer thickness used in the design procedure of the blowing slot.

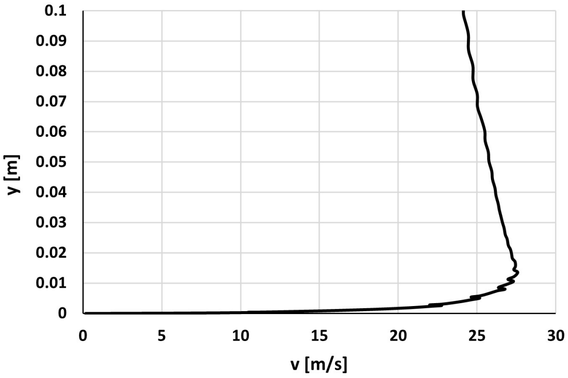

Figure 5.12: Velocity profile upstream and close to the separation point (x/c = 0.152)

It is observed that the flow velocity maximum is present near the wall rather than converging to a maximum freestream value. This could be explained by the presence of the propeller jump maximum towards the tip of the blade and the suction peak produced by the airfoil's curvature, accelerating the flow near the surface. The boundary layer thickness is estimated by considering the point where the velocity magnitude has its maximum and then starts decreasing. Based on the plot, the resulting boundary layer thickness is then considered as 16 millimeters.

As a summary, the CFD results on the approximated experimental setup, show that the separation point is strongly dependent on the upstream bleed size between the pressure side of the wing and the wind-tunnel wall. For the purpose of this project, the separation point is aimed to occur upstream of the propeller, while allowing for the blowing slot to be integrated within the wing insert's boundaries. This leads to the most optimal condition to evaluate the separation region mitigation using blowing jet to be 30 degrees angle of attack, while there is no upstream bleed. This would maximize the separation region size to be observed upstream of the propeller, while considering the structural integration of the blowing slot within the insert.

6

Experimental analysis

This chapter provides the reader with a description of the performed experimental analysis on the selected propeller-wing configuration. The chapter begins with the description of the used wind-tunnel setup, followed by the methodology for performing the experiments. The obtained results are then provided and discussed.

6.1. Experimental setup

The experimental analysis has been performed in the SLT wind-tunnel of the Low Speed Laboratory of TU Delft. The used test-section has dimensions of 1.8×0.9×0.6 meters. The propeller-wing assembly has been designed to be installed on the left side of the test-section when facing the wind-tunnel's nozzle, as depicted on Figure 6.2 and Figure 6.3. This allows for the wing size to have a tight fit with the height of the test-section minimizing the formation of 3D-effects of the flow near the wing tips. The propeller position is fixed with respect to the wing using two mounting plates at the wing tips. A detailed 2D drawing of the top plate of the assembly is provided as an attachment to this document as a supplemental material in Appendix F. The bottom plate has just a mirrored design of the top plate. The propeller is mounted such that the minimum tip clearance is obtained at the mid-span of the wing, using 4 metal bars with 3D printed parts matching the propeller drive body. This mounting design at the wingtips allows for no flow blockage from an object that would alternatively be required to be installed within the blowing span to keep the propeller drive at the set position from the wing. Additionally, each rod supporting the propeller drive is fixed to the corresponding mounting plate in three points preventing the free movement of the propeller drive's supports on the surface of the mounting plate but also the twisting of the whole assembly. The propeller drive arm that contains the required electrical cables and cooling tubes for its operation is designed to stick out of the test-section and to be supported by a long vertical rod, maintaining the horizontal plane. The top and bottom test-section walls are present during all tests, while the right wall is selected to be removed. The presence of the right wall is expected to force the flow to stay attached to its surface, while the Coanda effect over the wing's suction surface would force the flow towards the left side of the test-section. Hence, this is considered to result in significant divergence of the flow over the suction surface of the wing leading to strong influence on the separation point.

The freestream velocity during the tests is measured by a pitot-static tube at mid-height of the most upstream location of the right side of the test-section, as shown on Figure 6.2.This choice is considered to be reasonable due to two reasons. First, the velocity is measured exactly at the velocity inlet where the flow is assumed to be undisturbed as there are not upstream objects that could influence the flow. Second, this positioning is expected to most closely replicate the conditions at the region of interest as the propeller-wing assembly is mounted also close to the wall instead of the centerline of the test-section. In case positioned just upstream the propeller-wing assembly, the pressure measurement of the pitot-static tube is affected by the flow blockage induced by the presence of the assembly. If positioned at the top or bottom centerline of the test-section, the freestream velocity estimation is higher due to the fact that the tube experiences lower influence of the boundary layer velocity deficits developed over the side walls, allowing the friction forces to be minimized.

The active flow control is performed by actuation of a limited maximum mass-flow provided by the air supply system of the laboratory. The different blowing coefficients were achieved by setting a selected percentage of this maximum mass-flow rate by a mass-flow controller, shown on Figure 6.1. A sketch of the layout of the air supply system in the laboratory is provided on Figure 6.4.

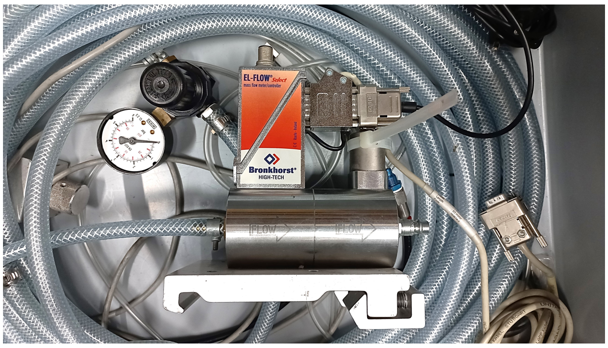

Figure 6.1: Bronkhorst EL-FLOW Select mass-flow controller

The flow transfer from the controller to the blowing slot is done by a circular air tube connecting the supplied mass-flow to the rectangular pattern of holes made in the wing body, described further in this section. The passive flow control consists of a flow channel inlet within the wing body, connection from the rectangular flow inlet geometry to a circular tube, and an air tube allowing the captured mass-flow downstream of the propeller to be recirculated back at the blowing slot. The recirculation air tube which connects the blowing with the 'suction' slot outside the wing body considering machining costs of the wing model and installation convenience. Details about the blowing slot and the flow channel inlet are provided further in the document.

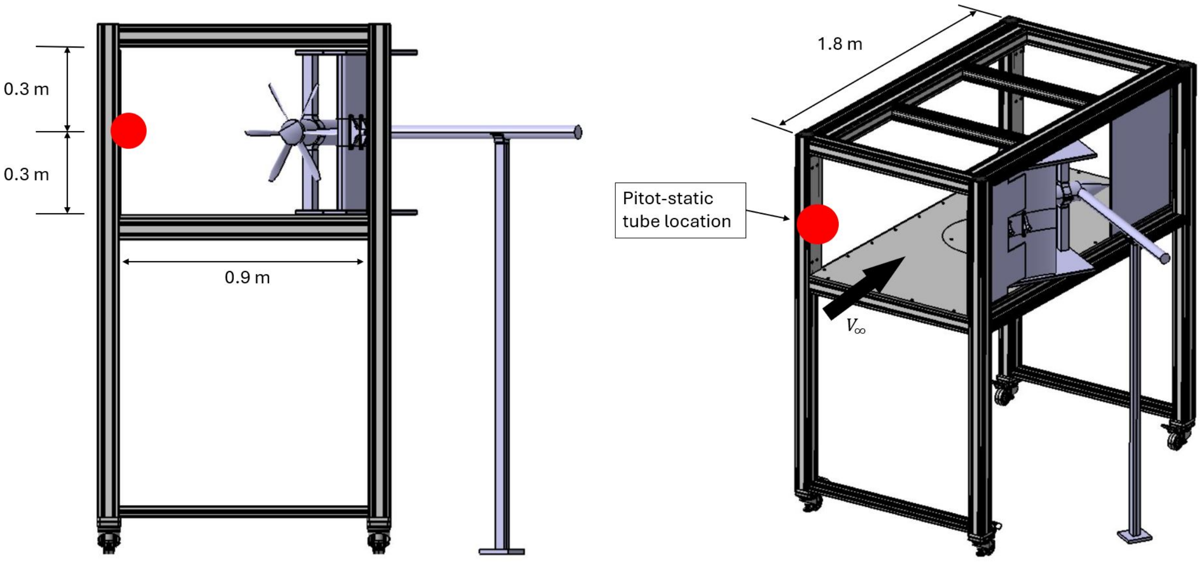

(a) Front view

(b) Isometric view

Figure 6.2: Experimental setup views

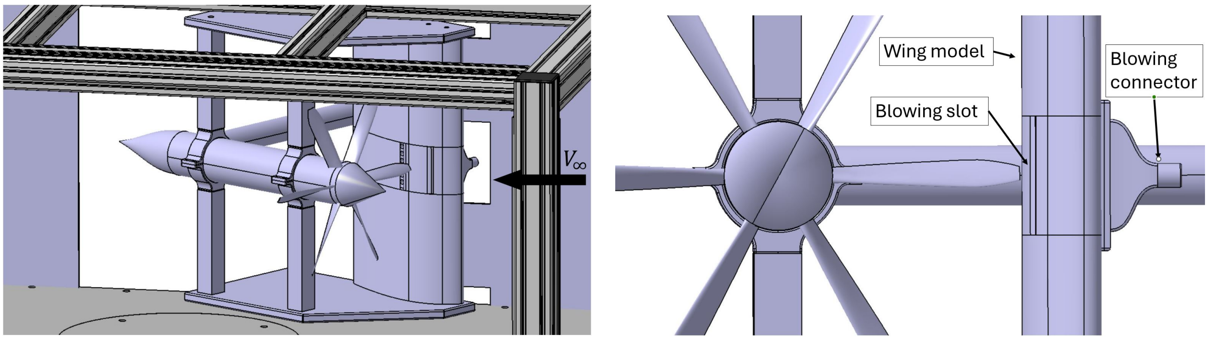

(a) Right side zoom-in at propeller-wing assembly

(b) Front view zoom-in at the propeller rotational plane

Figure 6.3: Experimental setup zoom-in views

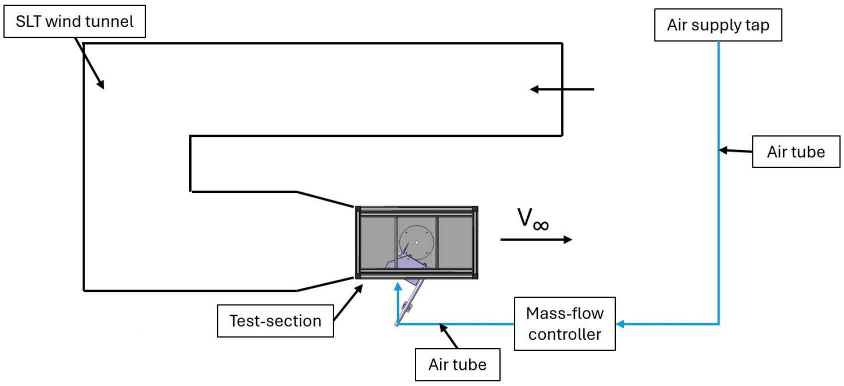

Figure 6.4: Sketch of the top view layout of the air supply system setup for the active flow control

6.1.1. Region of interest

The region of interest (ROI) for the analysis of the blowing method is selected to be the mid-span of the wing where the minimum tip clearance occurs. This selection choice is based on the fact that the mid-span is the location of the wing where the three-dimensionality of the flow is expected to be minimized such as wing-tip vortices or flow influence by the boundary layer formation at the mounting plates. Hence, selecting the mid-span for the experimental analysis is considered as the most appropriate to match the flow conditions in the performed numerical analysis described in chapter 5, where the three-dimensionality of the flow is ignored.

6.1.2. Blowing slot design

The blowing jet is designed to be actuated through a finite span upstream the estimated separation point for 30 degree angle of attack. However, since the minimum tip clearance occurs only at one location, while the blowing jet should be acting on a continuous spanwise distance, the jet is designed to be applied within the wingspan distance where the tip clearance is within typical percentages.

The maximum tip clearance selection is based on the finding of Li et al. [34] discussed in section 2.6 suggesting that the tip vortex intensity has not been observed to be affected by larger tip clearance than 2% of the propeller's diameter. Considering the TUD-XPROP's diameter of 406.4 mm, this results in maximum tip clearance of 8.13 mm. The lower limit of the tip clearance selection considers the methodology suggestion of the Hu et al. [35] for the maximum tip clearance to be 4 times larger than the minimum inspected tip clearance, leading to a minimum of 0.5% of the rotor diameter in this case. Hence, the minimum selected tip clearance for this project becomes 2.0325 mm. This results in 14.07 degrees in azimuthal angle with respect to the vertical position, for the blade to achieve a tip clearance of 2% of the diameter. The equation used to calculate the required azimuthal angle is:

$$\phi = \arccos\left(\frac{R - \Delta\delta_{tip}}{R}\right) \tag{6.1}$$

This corresponds to a horizontal distance of 49.4 mm from the minimum tip clearance, which is then multiplied by 2 to obtain the total blowing slot span of 98.8 mm but has been rounded to 100 mm for manufacturing convenience. The equation used to calculate the total blowing slot span is provided as:

$$Blowing\ span = 2 \times R \times \sin\phi \tag{6.2}$$

As discussed in section 5.5, the boundary layer thickness is estimated to be 16 mm close upstream to the numerically estimated separation point for the case of 30 degrees angle of attack. Following the mentioned recommendation in the Tomas et al. [56] paper, 5-20% of the boundary layer is also considered for this project. Hence, the influence of the slot on the aerodynamic characteristics of the wing contour is minimized when not active. This corresponds to a slot width of 0.8-3.2 mm. To analyze the effect of the slot size, selected are widths of 1 and 3 mm to be designed, shown on Figure 6.5 and Figure 6.6. The angle of blowing with respect to the local wing curvature is selected to be 20 degrees, following the recommendations of Müller-Vahl et al. [54], Puri et al. [60], and Matalanis et al. [61], discussed in subsection 3.2.4. Further details about the slots can be found on the corresponding technical drawings provided as a supplemental material in Appendix F. It is noted that the 1 mm width slot has a decreased span with 4 mm at the left and the right side. This reduction is made such that a structural reinforcement of the blowing slot geometry is applied when 3D-printed, minimizing the risk of fracture at high blowing coefficients.

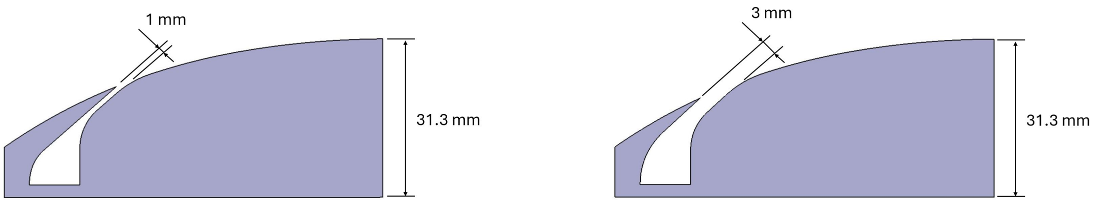

(a) Blowing slot width = 1 mm

(b) Blowing slot width = 3 mm

Figure 6.5: Blowing slot design: Left view

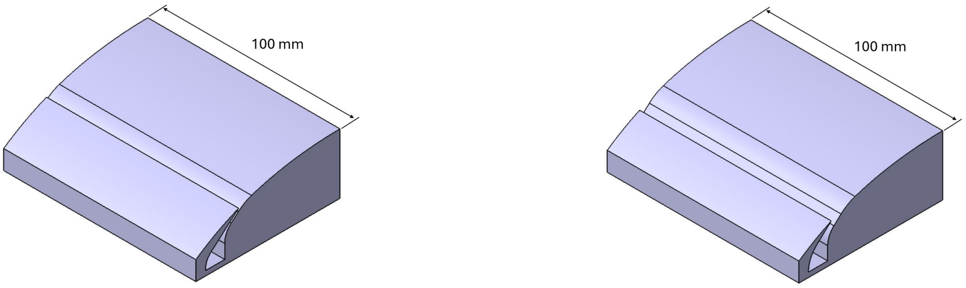

(a) Blowing slot width = 1 mm

(b) Blowing slot width = 3 mm

Figure 6.6: Blowing slot design: Isometric view

6.1.3. Blowing slot connector

The active flow control is regulated by an air supply tube connection to the mass-flow controller. As the tube cross-section is circular, while the blowing slot rectangular, a connector between the tube and the slot has been designed. It distributes the mass-flow from the air supply tube to each of the 6 holes made in the wing model with 10 millimeter in diameter each. The design of the connector is based on the 1/7th power law applicable for estimation of boundary layer profiles in pipes as suggested by Salama [83] and De Chant [84]. The general expression of the law is defined as [83]:

$$\frac{u}{u_{max}} = \left[1 - \left(\frac{r}{R}\right)^{m}\right]^{\frac{1}{n}} \tag{6.3}$$

The fitting parameters *m* and *n* that the law incorporates represent a non-dimensional length scale and overall exponent respectively. [83] Figure 6.7 shows the dependence of the power law on these two exponents. The velocity ratio of the local to freestream velocity is plotted on the x-axis, while the normalized radial position with respect to the pipe's centerline is plotted on the y-axis.

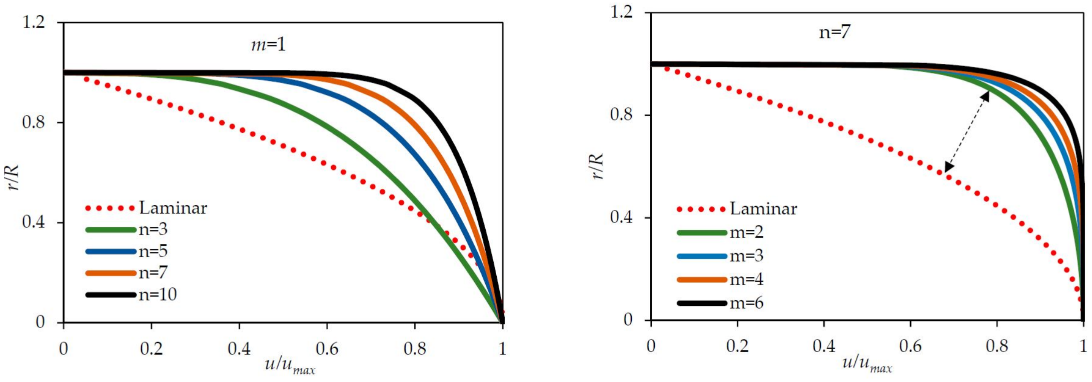

(a) m=1, n varies

(b) n=7, m varies

Figure 6.7: Normalized velocity profiles along a radial position of a pipe wall [83]

The Salama [83] study reports that n = 7 is found to match many of the cases involving fully developed turbulent flow over smooth surfaces. Using the basic formulation of the law with m = 1 has the two disadvantages of not having continuous derivative at the centerline and it does not match the laminar flow at relatively low Reynolds number. The continuity of the profile is satisfied at m > 2. Analysis of experimental data indicates that m varies within a relatively narrow range (between 1 and 3) depending on the Reynolds number, while n varies over a broader range (from 1 to 12), and potentially beyond. However, it is further noted by the paper, that this power-law profile is not intended for wall shear stress calculations. Instead, it is more appropriate for estimating parameters such as flow rate and cross-sectional average velocity. Moreover, the modified power law can potentially be extended to non-circular ducts. Hence, since a fully developed turbulent flow is expected within the air supply tube, the values used for estimating the air velocity profile are assumed to be m = 2 and n = 7.

The supplied air is designed to reach the blowing slot through 6 equally spaced circular holes drilled in the wing model, as presented in Figure F.2. They connect the blowing slot body to the pressure side of the wing, where the connector supplies air to each of them. A simple hollow body connecting the air supply tube to the rectangular sequence of the 6 holes is expected to result in unequal distributed mass-flow due to the shape of the velocity profile in the tube and blending region. This means that the holes that are closer to the air supply tube are expected to receive larger mass-flow than the farther holes. Hence, this issue has been selected to be mitigated by splitting the inlet of the connector where the air supply tube is attached into 6 different sectors by implementing 5 internal vertical bars (vanes). The resulting 6 sectors are then connected to a corresponding connector outlet hole sequence, matching the drilled holes in the wing's pressure side. Hence, the inner structure of the connector is split in 6 different channels. The spacing of the vertical vanes is selected such that the air-supply mass-flow is distributed equally in each channel.

The methodology to achieve this is by considering the average velocity ratio in each channel based on the radial location in the obtained velocity profile with m = 2 and n = 7. Considered are velocity ratio of 1 for the two central sectors, 0.96 for the two at medium distance, and 0.8 for the two farthest sectors. The thickness of the vanes is selected to be 1 millimeter. Then based on an iterative process, the locations of the vanes have been determined to be at 0, 2.325 and 4.635 mm from the centerline of the air supply tube. The Python code used to for this calculation is presented in Appendix E. The code considers a quarter-circle for simplicity where the central vane is fixed, while the remaining vanes position can be varied. The mass-flow is estimated for each of the enclosed areas by the vanes position with respect to the selected thickness. Important to note is that the velocity ratios do not account for the flow blockage and viscosity effects on the supplied air. Hence, the uncertainty of this approximation of the equal mass-flow distribution is assumed to be high as the flow development within the connector requires CFD analysis for accurate estimations of the distributed mass-flow in the channels. However, due to time-limitations of this project this has not been performed. The 3D model of the designed blowing connector is shown on Figure 6.8, while the technical drawing with the used dimensions is provided in Appendix F. The connector is mounted on the pressure side of the wing using two-bolt connection. The contact face of the connector with the wing is designed to match the local curvature of the mounting place to the wing. Additionally, the contact place has been sealed with a gasket such that mass-flow leakage is prevented.

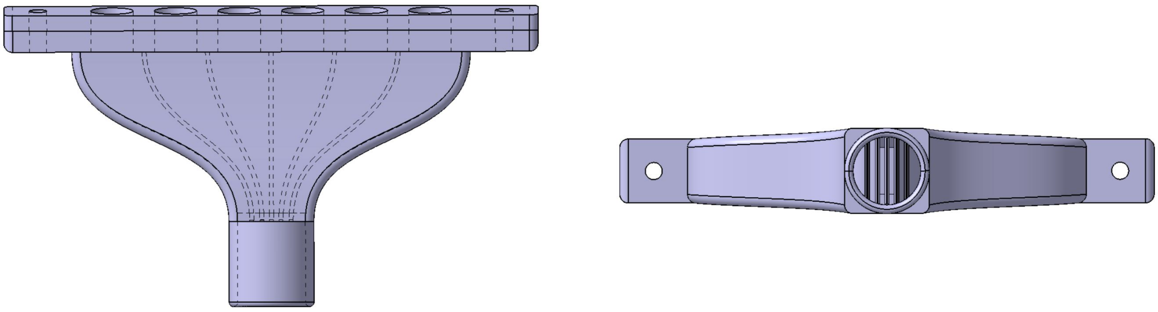

(a) Front view: Indicated internal vanes

(b) Bottom view: Air supply connection side

Figure 6.8: Connector blowing side

6.1.4. Passive flow channel inlet design

As mentioned earlier in the document, the passive flow control is designed by implementing an external air tube on the wing model, connecting the flow channel inlet, positioned downstream of the propeller, to the blowing slot, positioned upstream of the propeller. The length of the tube is approximately 0.85 meters. The length of the tube has been selected such that a concept of such a passive flow channel is tested, while maintaining the length as short as possible such that the air friction losses are minimized until the flow reaches the blowing slot and also allowing for a convenient installation in the setup. The sketch of the left view of the designed passive flow channel system is shown in Figure 6.9.

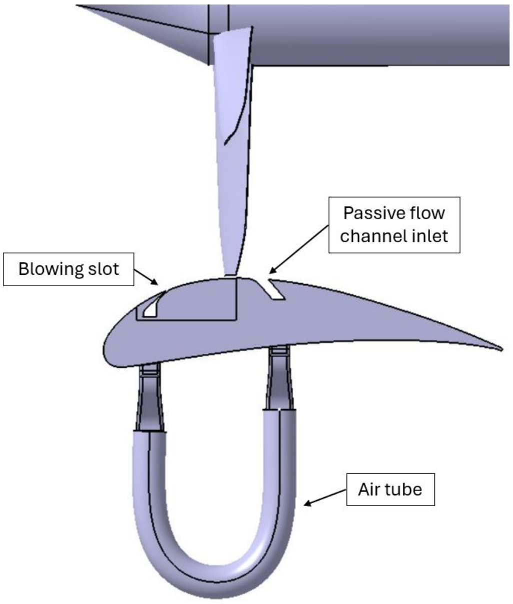

Figure 6.9: Sketch of the left view of the designed passive flow channel. The air tube length is not to scale.

The passive flow channel inlet is selected to be with the same span as the blowing slot such that the same span reference is investigated. Following the suggestion of the Sheng et al. [85] patent, the suction slot is designed to be placed at 1 tip chord length downstream from the trailing edge of the propeller tip. The patent further suggests the range of the suction slot to be within 1-5% of the duct radius. This leads to a minimum slot suction slot size of 2.05 mm and maximum of 10.26 mm. It is selected the suction slot to be with a width of 7.5 mm, following the suggestion in Genç et al. [86] paper conducting low Reynolds number CFD study on laminar separation bubbles suppression using single or simultaneous active blowing/suction slot area of 2.5% of the chord length of the NACA 2415 airfoil. The paper states that an increase in the suction area beyond 2.5% is expected not to improve lift significantly. The angle selected for Coanda effect is 40 degrees for manufacturing convenience with an upstream smoothened edge with a radius of 15 mm.

Similar to the drilled holes in the wing model for transferring the supplied air to the blowing slot, six holes with the same rectangular pattern have been made for the captured air to be transferred to the connector on the pressure side of the wing. The connector on the pressure side, however, is not designed with internal vanes as the blowing slot connector, but rather have a completely hollow design as no distribution of equal mass-flow is needed here, but rather collection of captured mass-flow. The technical drawing of the designed ’suction’ connector is attached to the document as a supplemental material in Appendix F.

The ideal conditions for the flow channel inlet would be to capture uniform mass-flow along its span, as the mass-flow is maximized. Based on actuator disc theory, the static pressure at far upstream and far downstream within the stream tube through the diameter of an operational propeller is identical. An extremely rough approximation of the blowing coefficient of the passive flow control may be made considering the predicted total pressure jump at the tip of the propeller of 128 Pa by Qblade solver in Figure 4.5b as it is the closest to the flow channel inlet. Considered is Bernoulli’s principle within the propeller stream tube with subscript ”1” indicates upstream the propeller, and ”2”- downstream:

$$p_{s1} + \frac{1}{2}\rho v_1^2 \ + \ \Delta p_t \ = \ p_{s2} + \frac{1}{2}\rho v_2^2 \tag{6.4}$$

Since the static pressure difference is neglected, the total pressure jump is then considered as dynamic pressure jump of 128 Pa. Hence, the velocity downstream the propeller results in 24.77 m/s with the 4.77 m/s induced by the pressure jump. The calculation is done with the following equation:

$$v_2 = \sqrt{v_\infty^2 + \frac{2\,\Delta p_t}{\rho}}. \tag{6.5}$$

Hence the mass-flow results in 0.0223 kg/s using the equation:

$$\dot{m} = \rho\, v_2\, A \tag{6.6}$$

Ignoring the friction losses within the channel until reaching the blowing slot and considering the blowing area, the resulting velocity at the blowing slot becomes 201.89 m/s and 67.30 m/s for 1 mm and 3 mm slot width respectively. This leads to respective blowing coefficients of 67.93% and 22.64%. However, these values assume complete uniformity of the pressure jump along the channel inlet and 100% Coanda effectiveness redirecting all the mass-flow towards the inlet, no separated flow and zero tip clearance. However, this is not true as the local velocity inlet conditions vary along the inlet span due to the change of the total pressure jump as there is a finite minimum tip clearance which increases towards the inlet boundaries. More importantly, considering the numerical analysis, the inlet is located at the chord-wise position where the flow is expected to be separated from the wing surface. Furthermore, the assumption of equal static pressure at the flow inlet with the upstream of propeller should not be true as the inlet is positioned at just one tip chord length downstream the propeller, which is expected to be still within the region where the static pressure downstream the propeller still decreases, so the static pressure at the inlet is higher than at far upstream of the propeller. These factors make the mentioned approximation of the blowing coefficient from the passive flow channel in the ideal conditions invalid. A more realistic estimation would be possible with conducting numerical study on the designed flow channel inlet configuration where the velocity within the inlet’s span can be obtained.

Based on the findings from the experimental study with this passive flow control provided further in this chapter, the resulting achieved blowing coefficient is lower than 0.69% for both the tested freestream velocities with 1 mm slot. This supports the expectation that the assumptions made for this calculated potential blowing coefficient in ideal conditions are invalid.

6.2. Results

The results from the performed experimental testing of the effectiveness of the blowing slot are provided below. They are differentiated between propeller off and on case.

6.2.1. Propeller off

The condition where the propeller is not present has been investigated by both designed blowing slot thicknesses. The 3 mm slot width analysis involves velocity profile readings at specific locations and tufts visualization of the flow field over key points on the wing. While the 1 mm slot width data is extracted solely from performed PIV flow visualization technique. A detailed description of the setup of these used measurement techniques is provided further in the document.

Blowing slot width = 3 mm

For the case of blowing slot width of 3 mm, the dynamic pressure data has been measured at 1 and 2 quarter-chords downstream from the propeller tip trailing edge for freestream velocity of 10 and 20 m/s at 25 and 30 degrees angle of attack. The measurements have been made while the propeller is not operational and an active steady blowing is injected through the slot. This has been done by traversing a pressure probe in a perpendicular axis to the chord line. The probe provides reading of the local dynamic pressure based on Bernoulli's principle of subtraction of the measured local static from the local total pressure. The data has been used to obtain the corresponding airflow velocity based on the dynamic pressure (q) to velocity (v) relation:

$$v = \sqrt{\frac{2 \times q}{\rho}} \tag{6.7}$$

It should be noted that at the near wall locations the readings for the dynamic pressure are negative. This indicates that the local static pressure is larger than the local total pressure. Hence, this cannot be used as a valid indication of the air velocity, but just as indication of strongly disturbed flow such as the separation region. The following sections present the resulting velocity profiles with negative velocities calculated from the negative dynamic pressure readings. The negative values in the plots consider the absolute value of the negative pressure and then being converted to negative just such that the velocity profile can be completed near the wall, but not accurate value of the air velocity.

Additionally, the profiles have been investigated at 1 and 2 quarter-chords downstream the expected propeller tip trailing edge. These locations are selected despite that the focus of this study is on the flow field upstream the propeller, as the boundary layer thickness upstream the propeller is expected to be highly uncertain due to its small thickness. Hence, analyzing the velocity profile downstream the expected propeller mounting point allows for more convenient evaluation of the blowing coefficient effect on the velocity profile and hence, separation thickness. The nearest point of the pressure probe to the wing surface is selected to be 1 mm as lower value is expected to cause high probability of interaction of the two bodies due to vibration. To prevent strong influence by the propeller drive on the pressure measurements, the pressure probe is selected to have the same minimum offset from the hub of the propeller. Hence, due to the larger airfoil thickness at 1 than at 2 quarter-chords position, the velocity profile at 1 quarter-chord location has smaller y-coordinate range. The sketch of the pressure probe traverse lines are shown on Figure 6.10.

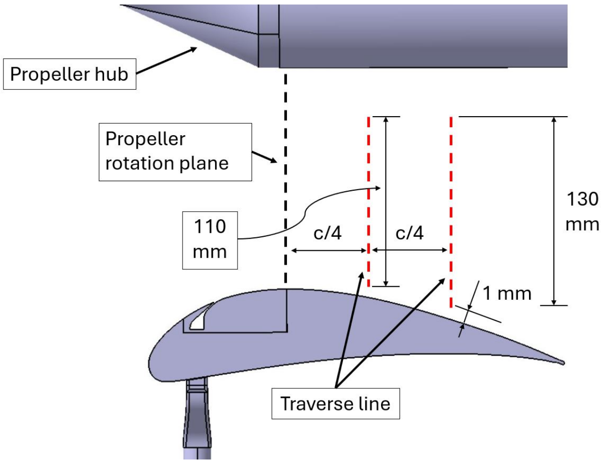

Figure 6.10: Pressure probe traverse lines shown in red color

The effectiveness on the velocity profile of several percentages of the maximum mass-flow available from the air supply system of the laboratory have been analyzed. As the blowing slot has a finite length, the corresponding blowing coefficient based on Equation 3.2.1 is calculated by considering the blowing slot area as the span of the blowing slot multiplied by the slot width, while the reference area (S) to be the slot span multiplied by the chord length. The maximum mass-flow provided by the laboratory is $\dot{m}_{\text{max}} = 5.6 \times 10^{-3} \ \ kg/s$. The air density of the jet and the freestream air are considered to be identical. The resulting percentages of mass-flow vs blowing coefficients for the blowing slot width of 3 mm is presented in Table 6.1:

Table 6.1: Jet velocity and momentum coefficient for selected blowing percentages with blowing slot width of 3 mm

v_∞	**10 m/s**			
Mass-flow %	20%	50%	80%	100%
v_{jet} [m/s]	3.11	7.78	12.45	15.56
C_μ	0.19%	1.21%	3.10%	4.84%
v_∞	**20 m/s**			
Mass-flow %	20%	50%	80%	100%
v_{jet} [m/s]	3.11	7.78	12.45	15.56
C_μ	0.05%	0.30%	0.78%	1.21%

Figure 6.11 presents the velocity profiles at unblown case (0%), 20%, 50%, 80%, and 100% of the available mass-flow for both freestream velocities.

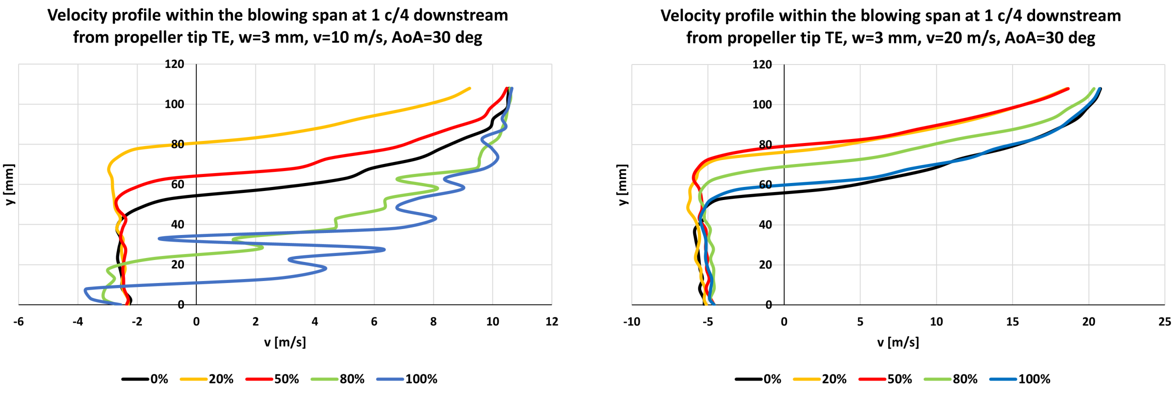

(a) v = 10 m/s **(b)** v = 20 m/s

Figure 6.11: Velocity profiles comparison at 1 quarter-chord downstream of propeller tip TE within the blowing span at AoA=30 degrees for different active blowing percentages of the maximum available mass-flow

Analyzing Figure 6.11a showing the velocity profiles for freestream velocity of 10 m/s, it can be concluded that the low blowing coefficient increases the separation region compared to the unblown case. More specifically, the lowest (20%) mass-flow percentage shows the largest increase in the separation region thickness. On the other hand, a blowing with 80% and 100% of the mass-flow shows positive effectiveness in decreasing the separation region. Additionally, it is observed highly unstable flow for these two percentages as the velocity profile shows rapid deviations from the mean line, specifically near the wing's surface, while the deviations are observed to dampen towards the outer region of the profile. This indicates that the injected air has the largest impact near the wing's surface as intended, but also that the difference between the injected air and freestream velocities promotes the flow to show strong unstable behavior.

Looking at Figure 6.11b it can be concluded that none of the blowing jet intensities has a positive improvement effect on the separation region at 20 m/s. In fact, all of them show triggering an increase of this region. Furthermore, the velocity profiles show no signs of instability up to the largest jet strength. Comparing the velocity profiles for both freestream velocities, the same mass-flow percentages, and hence same injected velocity achieves a greater impact on the profile at lower than higher freestream velocity, and therefore Reynolds number. This can be explained by the fact that the same injected velocity magnitude results in greater difference in blowing coefficient at lower freestream velocity than at higher freestream velocity, as seen also in Table 6.1. This is due to the fact that the freestream velocity only affects the reference dynamic pressure expressed in the denominator in Equation 3.2.1. Hence, the lower the freestream is, the greater the velocity profile behavior variation would be expected to be observed. Similar results were obtained at further downstream. Figure 6.12 displays the velocity profiles at 2 quarter-chords from the propeller tip trailing edge.

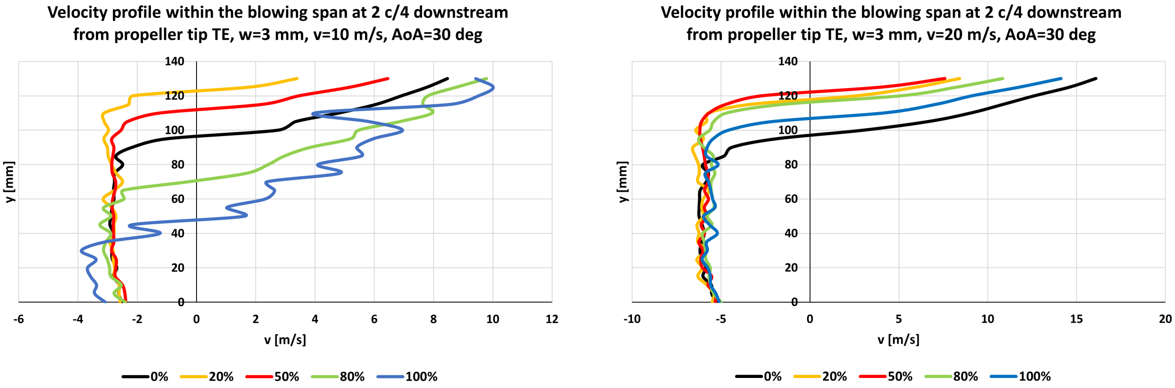

(a) v = 10 m/s **(b)** v = 20 m/s

Figure 6.12: Velocity profiles comparison at 2 quarter-chords downstream of propeller tip TE within the blowing span at AoA=30 degrees for different active blowing percentages of the maximum available mass-flow

As expected, the separation region has a larger thickness compared to the measured at 1 quarter-chord. It is indicated that for both 10 and 20 m/s freestream velocity, the lowest blowing coefficient results in the largest increase in the separation region. Interestingly, on Figure 6.12b showing the profiles for 20 m/s, the 20% and 50% blowing show significant similarity to the resulting separation thickness. The substantially larger reference dynamic pressure prevents the jet velocity to have a noticeable impact on the profile up to higher mass-flow injection.

The obtained data also agrees with the findings in the previously mentioned Müller-Vahl et al. [54] in subsection 3.2.1. The paper reports that the low-blowing coefficient indeed increases the separation area over the investigated NACA 0018 airfoil. It has been stated that ”the exact mechanism by which steady blowing at low jet speeds induces the separation of an otherwise attached boundary layer has not been investigated in detail to the authors’ knowledge. It is generally interpreted as the “inverse effect” of blowing at high jet velocities: The addition of low-momentum fluid near the wall decreases the boundary-layer momentum, making it more susceptible to separation”. As mentioned in subsection 3.2.1 the paper states that the injection of a low-momentum air destabilizes the turbulent boundary layer, causing earlier separation point. It is reported by Chen et al. [53] that the low-blowing displaces the streamlines away from the wall, causing thicker boundary layer and pushing the separation point upstream. This finding has also been observed by Meijerink [87] who numerically investigates the tangential blowing effect on separation reduction on a ducted propeller. According to the study, the low-momentum blowing reduces the momentum of the original boundary layer it displaces. Consequently, the weakened boundary layer cannot overcome the adverse pressure gradient, resulting in flow separation.

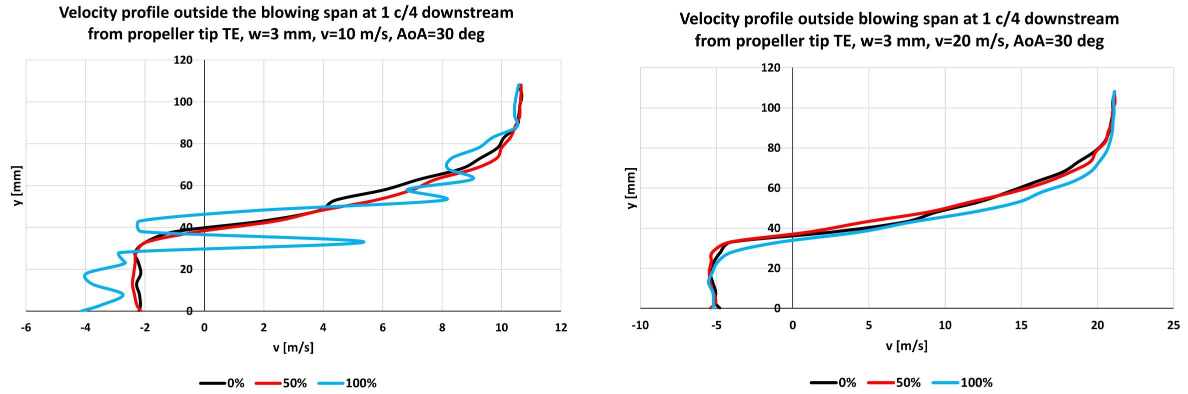

(a) v = 10 m/s

(b) v = 20 m/s

Figure 6.13: Velocity profiles comparison at 1 quarter-chord downstream of propeller tip TE outside the blowing span at AoA=30 degrees for different active blowing percentages of the maximum available mass-flow

Figure 6.13 shows the comparison of the velocity profiles for both 10 and 20 m/s freestream velocity in the region where it is not directly downstream from the blowing slot, but at mid-span between the blowing region and the wing tip. This location has been selected to evaluate the velocity profile at the region of the wing where the overall disturbances of the freestream velocity are minimal. Selecting this distance to be as close to the wing tip, would result in strong interaction with the boundary layer developed at the mounting plate of the assembly. On the other hand, shifting the spanwise measurement location too little from the blowing slot area would still be strongly affected by the blowing momentum of the jet. Compared are three blowing percentages - unblown (0%), 50%, and 100%. It is observed that the separation region in this part of the wing is not affected by any blowing percentage compared to the unblown case for both investigated freestream velocities.

Same has been observed in Figure 6.14. Interestingly, the data shows that at freestream of 10 m/s, blowing with 100% of the maximum mass-flow produces a highly unstable profile for both at 1 and 2 quarter-chord downstream locations. Additionally, the mean profile line is not altered compared to all other blowing cases. This could be explained by the instability strength induced by the mixing of the injected and freestream air boundary layers at this condition ($C_\mu = 4.84\%$) is sufficient to noticeably affect the stability of the velocity outside the region affected by the blowing slot. While for the case of 20 m/s in Figure 6.14b all the profiles are smooth and unchanged. The 100% blowing ($C_\mu = 1.21\%$) shows a bit smaller separation region but the difference is negligible and assumed to be due to a measurement error. This analysis clearly indicates that the instability of the flow at the blowing slot indirectly affects the stability of the flow outside the jet area.

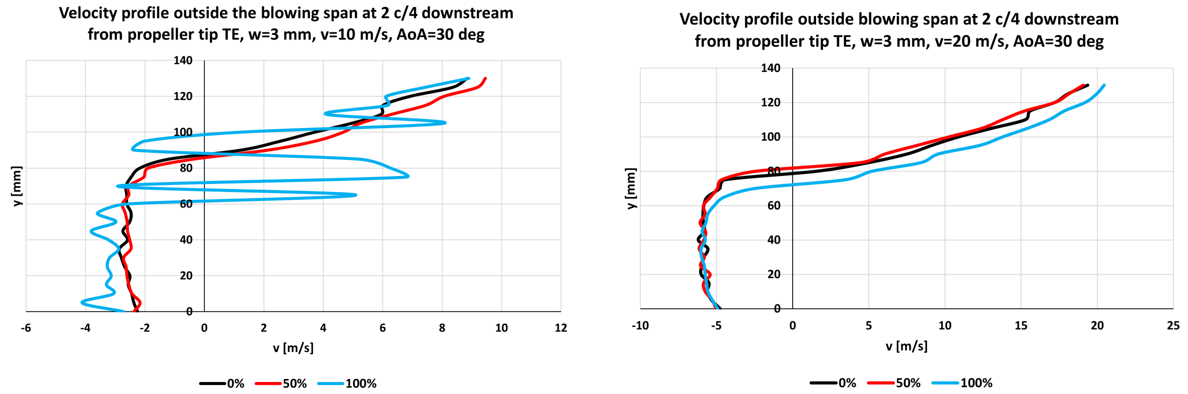

(a) v = 10 m/s

(b) v = 20 m/s

Figure 6.14: Velocity profiles comparison at 2 quarter-chords downstream of propeller tip TE outside the blowing span at AoA=30 degrees for different active blowing percentages of the maximum available mass-flow

Similar analysis has been performed for the case of 25 degrees of angle of attack. Both measurement locations indicate similar results to the 30 degrees angle of attack case. The data has been plotted in Figure 6.15 and Figure 6.16. Both figures indicate that the separation region has been increased by a low-blowing coefficient, while only 100% blowing at v = 10 m/s shows reduction of the separation region. However, it is interesting that the flow instability at 100% blowing at v = 10 m/s shows less intensity compared to the 30 degrees case on Figure 6.11a. This could be reasoned by the fact that the lower angle of attack allows the accelerated flow over the wing to increase its effectiveness up to a greater chord-wise position due to the reduced adverse pressure gradient, allowing for reduction of the separation region at the same measurement location. The reduction of the separation region allows for higher air momentum further downstream and hence, increasing the local flow velocity over the suction surface of the wing. This suppresses the blowing coefficient and consequently, the injected momentum cannot generate the same effectiveness as at higher angles where the local flow velocities are lower due to larger separation region.

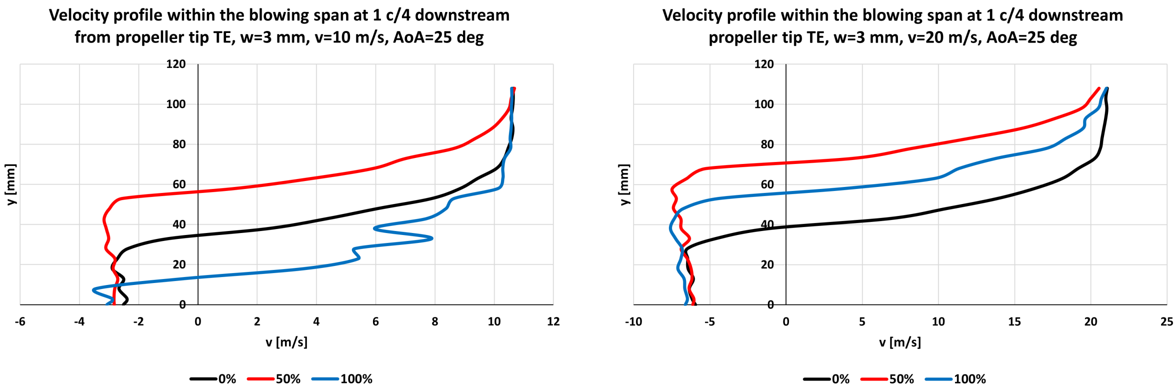

(a) v = 10 m/s **(b)** v = 20 m/s

Figure 6.15: Velocity profiles comparison at 1 quarter-chord downstream of propeller tip TE within the blowing span at AoA=25 degrees for different active blowing percentages of the maximum available mass-flow

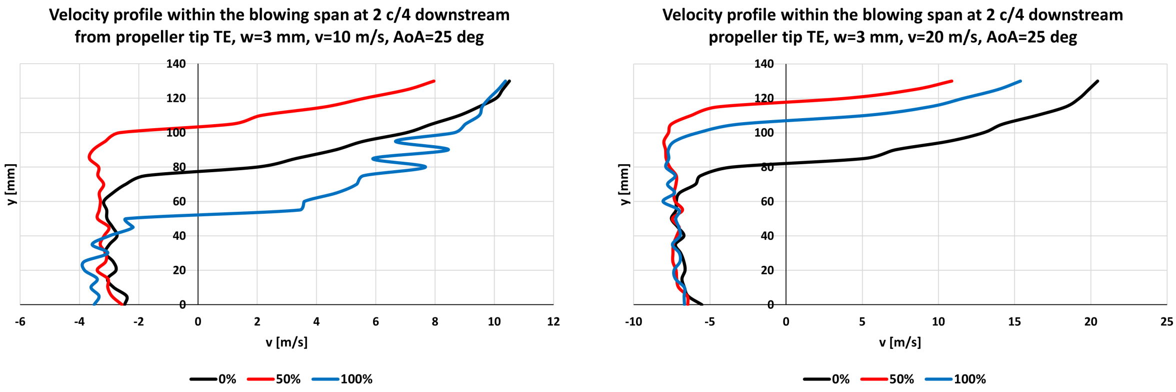

(a) v = 10 m/s **(b)** v = 20 m/s

Figure 6.16: Velocity profiles comparison at 2 quarter-chords downstream of propeller tip TE within the blowing span at AoA=25 degrees for different active blowing percentages of the maximum available mass-flow

Tufts visualization has also been used to evaluate the blowing coefficient effect on the flow on the whole wing model. Selected are four positions where tufts are positioned such that each tuft serves as indication for the local flow behavior. The selected positions are sketched on Figure 6.17. Three of the tufts are positioned downstream the rotation plane of the propeller and one tuft upstream between the propeller and the blowing slot. This way the flow behavior is observed qualitatively within and outside the blowing span. The tufts within the blowing span are positioned at the centerline of the blowing span, while the tufts outside the span are placed at the mid-span between the blowing region and the mounting plate of the propeller-wing assembly. This way they are expected to be reasonably indicative to the freestream flow as the influence of the injected air and the 3D-effects of the flow near the mounting plates is assumed to be equally minimized. Presented is the average tufts position at v = 20 m/s on Figure 6.18 and v = 10 m/s on Figure 6.19. The pictures are taken from the right side of the test-section facing the wing's suction surface. Therefore, the freestream air in the figures flows from right to left, and hence, the leading edge of the wing is on the right side of the images. The passive flow channel inlet has been covered with aluminum tape such that a scenario with only blowing slot present is investigated. Overall, the conclusion to be drawn based on the tuft positions for both freestream velocities is that the flow is not attached past the propeller plane of rotation in any blowing case for both freestream velocities, while 2 specific coefficients resulted in flow attachment upstream the propeller's rotational plane.

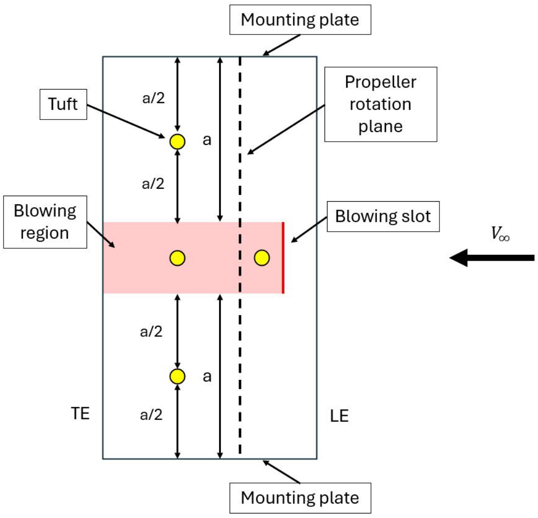

Figure 6.17: Sketch of the selected tuft positions on the suction side of the wing model

Looking at the 20 m/s case in Figure 6.18 fluctuations of the tufts are observed to be pointing mainly in upstream direction for all tested blowing mass-flow percentages. This indicates that the region downstream of the propeller rotational plane experiences a recirculating zone where the flow near the wall flows upstream as a result of the upstream flow separation point. The tuft at the centerline of the blowing slot downstream of the propeller does not indicate any flow attachment position which consequently implies that any of the blowing coefficients achieved by the blowing slot width of 3 mm with the given maximum mass-flow does not benefit to flow attachment past the propeller. This coincides with the analysis performed with the pressure probe readings as discussed earlier. The tuft between the propeller and the blowing slot is found to have a chaotic behavior for all the blowing coefficients applied. Hence, the separation point has not been pushed at least until the propeller location for up to $C_\mu = 1.21\%$.

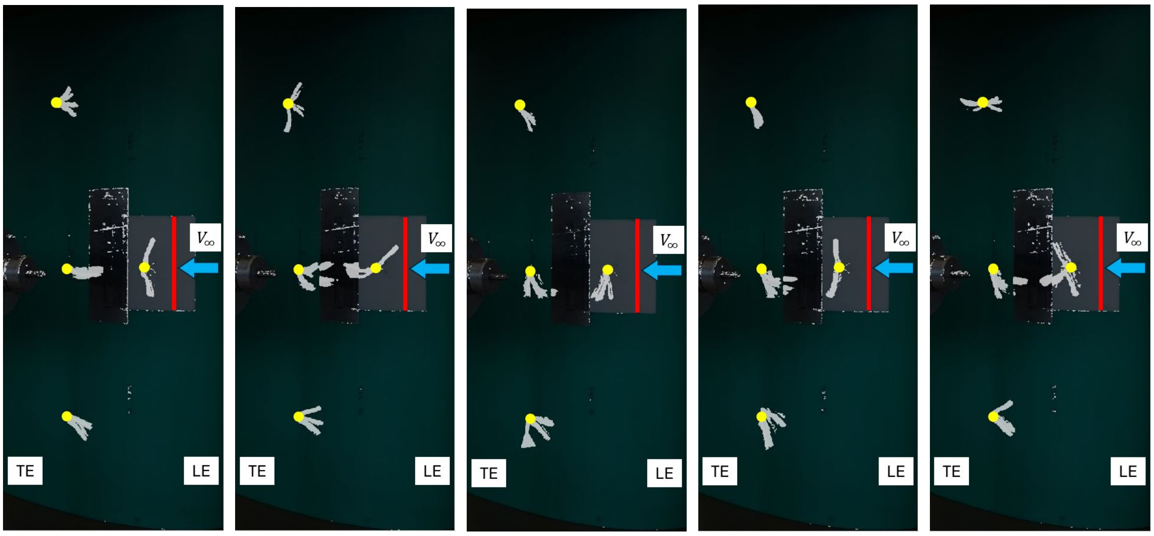

(a) 0% ($C_\mu = 0\%$) **(b)** 20% ($C_\mu = 0.05\%$) **(c)** 50% ($C_\mu = 0.30\%$) **(d)** 80% ($C_\mu = 0.78\%$) **(e)** 100% ($C_\mu = 1.21\%$)

Figure 6.18: Tuft flow visualization over darkened wing background at AoA=30 degrees, v_∞ = 20 m/s. The leading edge is on the right side of the images with air flowing from right to left. The freestream velocity is indicated with a blue arrow. The blowing slot span is indicated with a red line, while the center of rotation of each tuft is depicted with yellow color.

Analyzing the case for v = 10 m/s on Figure 6.19, it can be concluded that the tufts barely show any responsive behavior to the flow. Their orientation is mainly downwards, suggesting that the flow downstream of the propeller plane has insufficient momentum to be analyzed with the selected tufts design. However, greatest deviation from the vertical position it is observed for the case of the maximum blowing percentage (corresponding to $C_\mu = 4.84\%$) in Figure 6.19e where the position of the centerline tuft downstream the propeller shows unsteady behavior with the position fluctuating between downwards and streamlined. This also supports the pressure probe measurements discussed earlier which also suggest for the unsteady characteristics of the boundary layer downstream of the propeller position. However, the tuft positioned between the propeller and the blowing slot is found to start fluctuate its average position between downwards and streamlined at 50% blowing ($C_\mu = 1.21\%$), but this is also visible at the unblown case in Figure 6.19a. Therefore, this still could be due to separation intensity. While for 80% ($C_\mu = 3.10\%$) and 100% ($C_\mu = 4.29\%$) blowing, the tuft indicates completely attached flow. Therefore, it can be concluded that the approximate threshold where the blowing jet prevents the separation region up to the propeller rotational plane could be between $C_\mu = 1.21\%$ and $C_\mu = 3.10\%$.

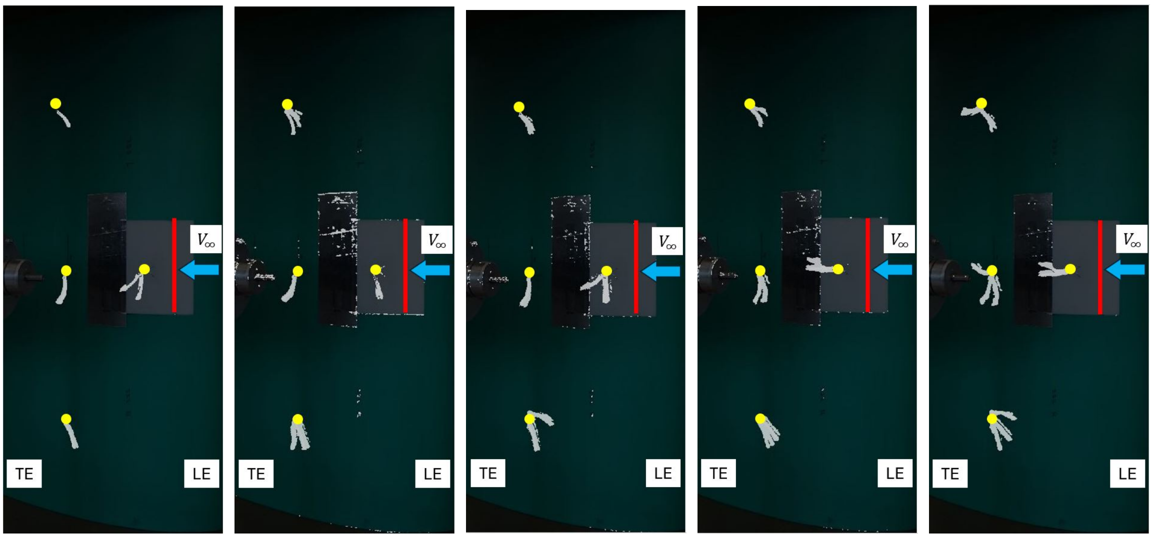

(a) 0% ($C_\mu = 0\%$) **(b)** 20% ($C_\mu = 0.19\%$) **(c)** 50% ($C_\mu = 1.21\%$) **(d)** 80% ($C_\mu = 3.10\%$) **(e)** 100% ($C_\mu = 4.84\%$)

Figure 6.19: Tuft flow visualization over darkened wing background at AoA=30 degrees, v_∞ = 10 m/s. The leading edge is on the right side of the images with air flowing from right to left. The freestream velocity is indicated with a blue arrow. The blowing slot span is indicated with a red line, while the center of rotation of each tuft is depicted with yellow color.

Blowing slot width = 1 mm

Same percentages of the maximum available mass-flow have been investigated for the blowing slot of 1 mm in width, representing 5% of the boundary layer thickness. The resulting corresponding blowing coefficients are provided in Table 6.2. As the injection width decreases, the injection slot area decreases, causing the injected velocity to increase such that the same mass-flow is corresponding injected percentage is achieved. Since the injected velocity rises with tighter slot, the achieved blowing coefficient is greater compared to the same blowing percentages for the case of 3 mm slot width. More specifically, three times smaller blowing width allows for roughly 3.5 times higher C_μ for the same mass-flow.

Table 6.2: Jet velocity and momentum coefficient for selected blowing percentages with blowing slot width of 1 mm

v_∞	**10 m/s**			
Mass-flow %	20%	50%	80%	100%
v_{jet} [m/s]	10.15	25.38	40.60	50.75
C_μ	0.69%	4.29%	10.99%	17.17%
v_∞	**20 m/s**			
Mass-flow %	20%	50%	80%	100%
v_{jet} [m/s]	10.15	25.38	40.60	50.75
C_μ	0.17%	1.07%	2.75%	4.29%

Particle Image Velocimetry (PIV) measurement technique is used to determine planar velocity fields around the blowing region upstream the propeller. It serves both for qualitative flow visualization and for quantitative analysis of velocity distributions within a flow. Since its introduction in the late 1970s, PIV has become a widely adopted standard in fluid mechanics research. [88] It is non-invasive flow visualization technique used to measure the velocities and trajectories of individual particles introduced into the fluid. These tracer particles are typically uniform, spherical in shape, and may be solid, liquid, or even gaseous. To accurately follow the fluid motion, the particles should be neutrally buoyant, minimizing sedimentation and drag relative to the surrounding fluid. This ensures the most precise flow visualization. As a result, it is generally assumed that the tracer particles move with the same velocity as the local fluid, and their physical properties match to those of the bulk flow. [89] The basic principle of PIV is illustrated in Figure 6.20.

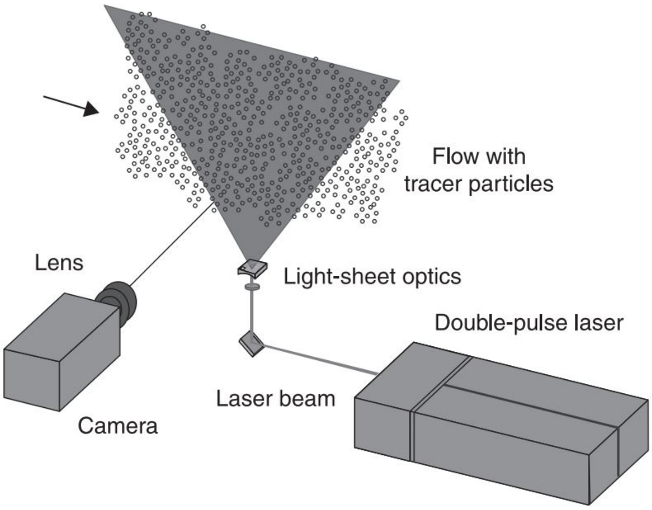

Figure 6.20: Typical PIV setup [88]

A thin plane within the flow is illuminated using light-sheet optics and a powerful light source. The tracer particles within this plane scatter the light and are captured by a camera. By recording two successive images, the displacement of the particles can be measured. The particle displacement between the second image and the first image is converted into velocity, accounting for the magnification of the imaging system and the time interval between the two recordings. [88]

The two captured images, which display the illuminated tracer particles as grayscale patterns, are divided into smaller sections known as interrogation windows. For each interrogation window in the first image, a pixel-wise correlation is performed with a region of the same size in the second image, centered around the corresponding location. This process generates a local correlation map for the particle or intensity pattern, as illustrated in Figure 6.21. The location of the peak value in this correlation map indicates the most probable vertical and horizontal displacement of the particle pattern within that particular interrogation window. [88]

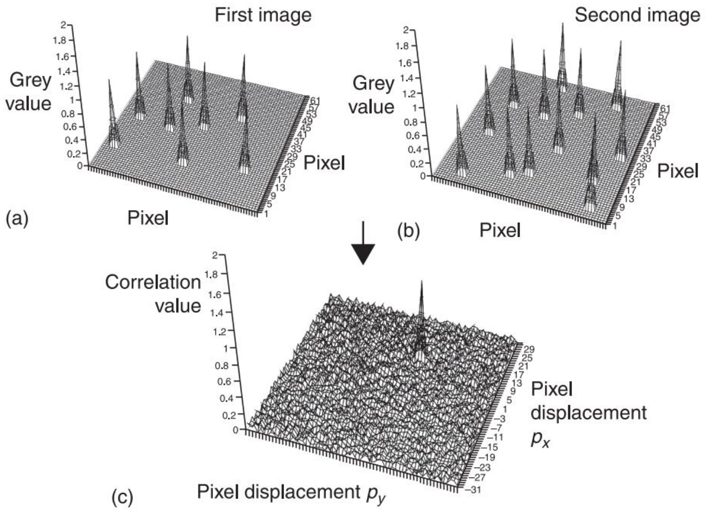

Figure 6.21: Cross-correlation map illustration [88]: First image (a) - particle pattern indicated by peaks, Second image (b) - particle pattern indicated by peaks, Cross-correlation map of the two images with the peak indicating the most probable displacement (c)

Applications for PIV technique are found both in scientific and industrial applications. Examples are fluid mechanics, aerodynamics, e.g. aircraft and airfoil profile design, characterization of building and bridge aerodynamic actions, sports science, combustion, hydraulics, or bio fluid mechanics. [90]

The selected region of interest for performing the PIV measurements is presented on Figure 6.22. The selection for the chord-wise dimension of the ROI has been made such that the flow field is captured partially upstream the blowing slot where the flow is expected to be attached and just downstream the passive flow control inlet serving as indicative region for the flow separation suppression downstream the propeller. The vertical distance of 85 millimeter between the slot location and the closest boundary to the propeller hub is selected such that the expected separation region thickness to be captured for angle of attack 30 degrees. The 10 millimeter below the blowing slot are selected such that the wing's surface does not take the majority of the ROI, while still being distinguishable. This ROI has been considered to be a trade-off between inspection of the separation region over the suction surface of the wing under the various blowing coefficients and mounting capabilities in the test-section for the intended setup.

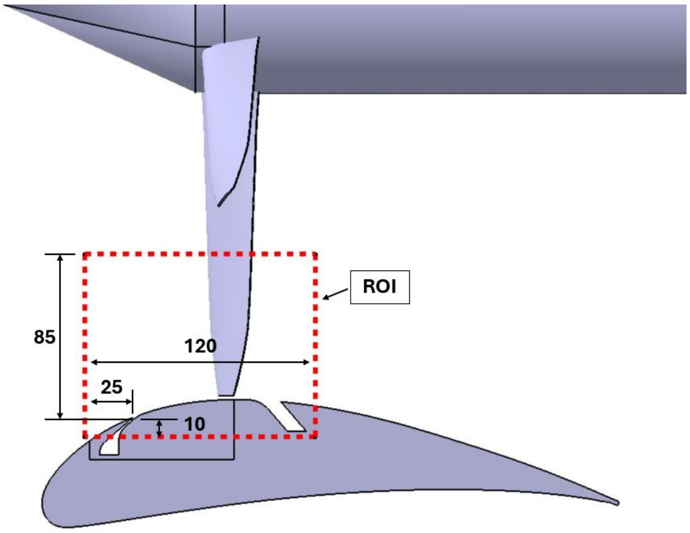

Figure 6.22: Selected region of interest for PIV measurements at wing's mid-span; Dimensions in millimeters

The top view of the PIV setup is sketched in Figure 6.23. The sketch indicates the laser position with the approximate laser sheet dimensions, while the propeller-wing assembly is under 30 degrees of angle of attack.

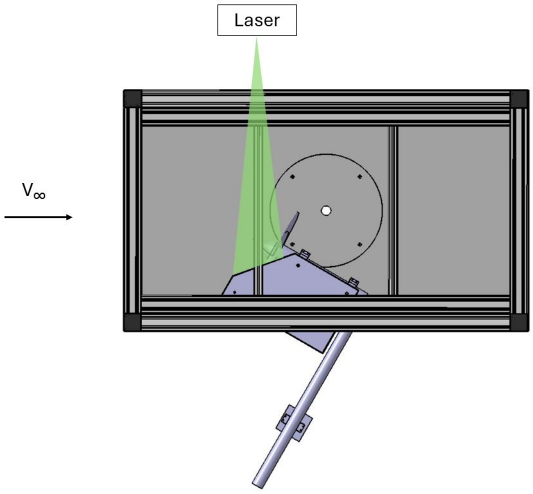

Figure 6.23: PIV setup sketch: Top view with propeller-wing assembly under 30 degrees angle of attack relative to the freestream flow

Figure 6.24 shows the propeller-wing assembly setup for the performed 2D PIV flow visualization technique for the 1 mm slot case. Considering the time-limitations of the project, PIV tests are done only with the blowing slot width of 1 mm as it allows for a wider range of blowing coefficients to be analyzed, compared to the 3 mm slot case. The camera for performing the PIV measurements is selected to be positioned below the bottom side of the test-section, looking upwards. A hole has been cut in the bottom mounting plate such that the flow field near the blowing slot can be visible by the camera, while still reliable mounting capability of the plate is maintained.

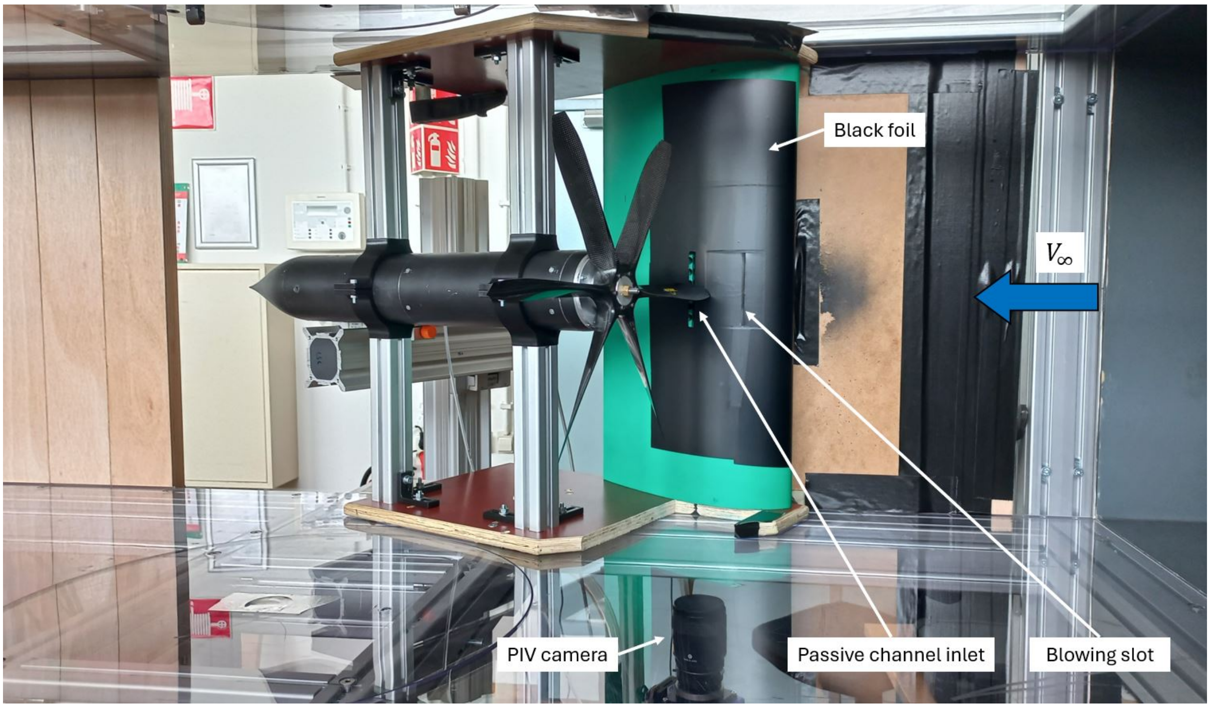

Figure 6.24: 2D PIV setup: Laser point of view; Freestream air flows from right to left

The original green color of the wing model has high reflectivity properties to the laser light leading to large difference between the reflectivity of the wing surface and the seeded particles in the airflow required for visualization of the flow field after post-processing of the image pair. Therefore, black foil has been applied on the suction surface such that the reflections are mitigated and acceptable flow visualization achieved. The foil has been applied only to the areas which are captured by the camera. Despite that the thickness of the foil affects the exact contour of the suction surface of the wing, this modification is assumed to be negligible. Further details for the performed 2D PIV technique are as follows:

- Image acquisition and post-processing software: DaVis
- Camera $f\#$ = 5.6
- Laser: Quantel Evergreen Nd-YAG Laser Class 4
- Laser light wavelength: 532 nm
- Laser power: 60%
- No propeller phase-locking
- Interrogation window size with 2 initial passes: 48×48 pixels
- Interrogation window size with 3 final passes: 16×16 pixels
- Interrogation window overlap factor: 50%
- v_∞ = 20 m/s:
    - Image rate: 15 Hz for propeller off, 12 Hz for propeller on
    - Time difference between image pair: 40 microseconds
- v_∞ = 10 m/s:
    - Image rate: 12 Hz
    - Time difference between image pair: 65 microseconds

Similar to the numerical analysis method, the PIV analysis is selected to be based on the averaged velocity field for the tested cases. The tests were performed for 20 and 10 m/s freestream velocity for the same advance ratio of the propeller. The rotational speed of the propeller at 20 m/s freestream velocity is 2109 RPM and 1054.6 RPM at 10 m/s. The provided PIV average velocity fields further in the document are obtained from 1000 images per case. The figures within this chapter concern only the cases of 20 m/s freestream velocity, while the data for 10 m/s is provided in Appendix D.

As the PIV technique allows to obtain information for the flow field upstream of the rotational propeller, it is selected to analyze the effectiveness of the blowing coefficient on the flow separation reduction by analyzing the velocity profile just upstream the propeller blade location. More specifically, this is 35 mm downstream of the blowing slot, which is 11.67% of the wing's chord length. This location has been selected as it has two advantages. The first is that it represents the largest distance downstream the blowing slot where the flow separation can be investigated before the seeded particles trajectory in the flow is strongly influenced by the propeller's rotation. The second advantage is that propeller inflow velocity profile uniformity can be evaluated. First, the velocity profile comparison for the propeller off case is displayed on Figure 6.25.

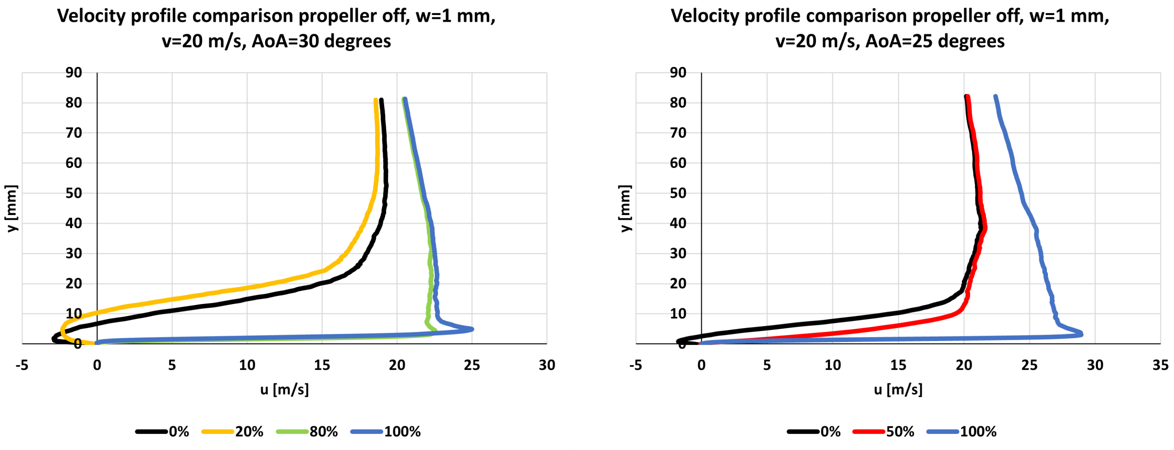

(a) Propeller off, AoA = 30 degrees

(b) Propeller off, AoA = 25 degrees

Figure 6.25: PIV data: Velocity profile comparison at just upstream the propeller blade location at v_∞ = 20 m/s

It can be concluded that the separation is observed for the unblown and 20% of the maximum mass-flow as the velocity near the wing surface has a negative magnitude, indicating for a flow reversal at the location of measurement. Additionally, it is visible that the low-blowing jet of 20% of the maximum mass-flow leads to an increase of the thickness of the separation region. However, the separation is observed to be fully suppressed for the 80% and 100% cases, corresponding to blowing coefficient of 2.75% and 4.29% respectively. Additionally, it should be noted that the a case for 50% ($C_\mu = 1.07\%$) for 30 degrees angle of attack was unfortunately skipped during the tests by a mistake. However, based on the profile comparison it could be expected that the 50% ($C_\mu = 1.07\%$) should be close to the coefficient threshold where the blowing momentum is sufficient for beneficial effect on the separation region reduction.

Looking at the case for freestream velocity of 10 m/s on Figure D.1, the flow separation is already prevented by the 20% ($C_\mu = 0.69\%$) case or higher. It is further analyzed that the higher the blowing percentage, the larger the normal distance from the wall is where the peak of the injected air velocity is. This could be reasoned by the reduction of the Coanda effect with increasing the momentum of the injected air. This has been also observed by He et al. [91] which investigates the improvement of the jet pressure ratio and jet velocity in the circulation control of an airfoil in a high subsonic airflow. The paper reports that outward shift of the velocity maximum with increasing blowing coefficient, and at even higher momentum ratios, has been observed to cause premature detachment of Coanda jets. Kamotani et al. [92] states that when a jet issues along a curved wall, the shearing and entrainment of fluid between the jet and the surface induce a region of low pressure at the wall. This pressure difference forces the jet to bend and remain attached to the surface. However, as the jet momentum increases, the required pressure gradient to maintain curvature also rises, and the entrainment-induced low pressure may no longer be sufficient to keep the jet fully attached.

The 3D model of the wing is overlaid over the PIV velocity fields for the corresponding propeller off, propeller on, and passive flow control case. This way a better visualization can be made with respect to the blowing slot position. The results for the 30 degrees angle of attack when propeller is not operational are presented on Figure 6.26. The higher velocities are indicated by warm colors with the highest corresponds to red, the lower velocities with colder colors with the lowest corresponding to black. The relative velocity magnitude range is kept identical for all the figures presented.

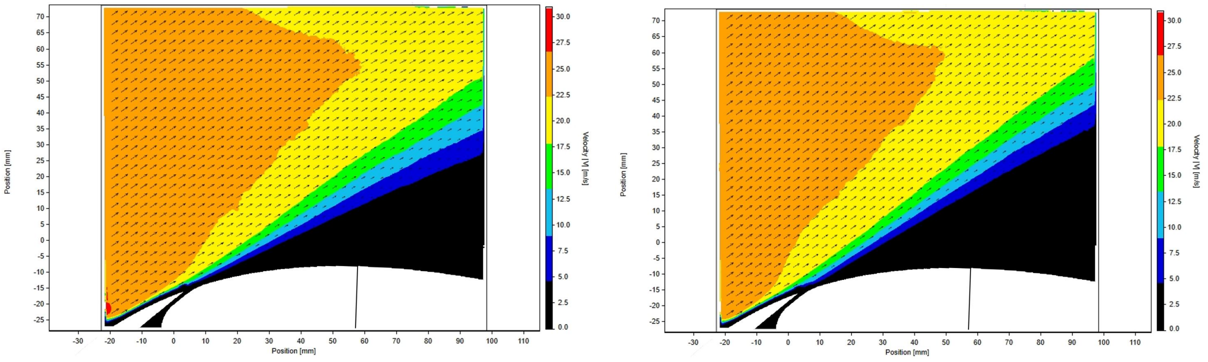

(a) 0% **(b)** 20% ($C_\mu = 0.17\%$)

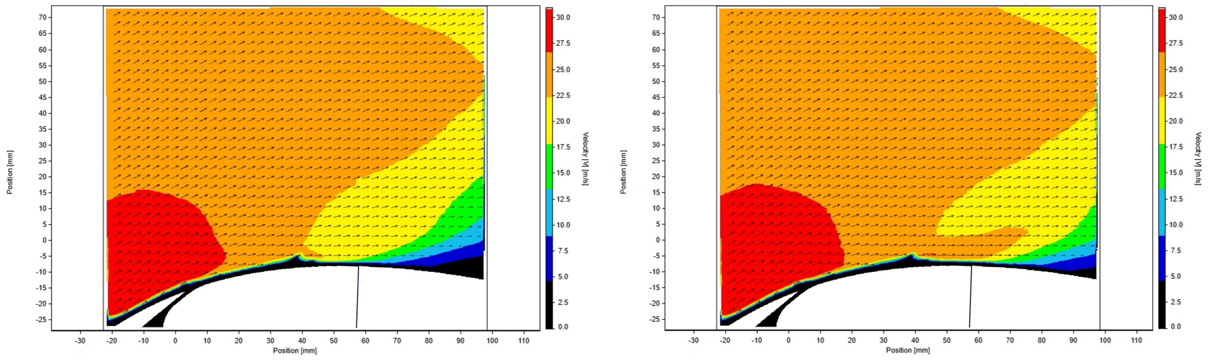

(c) 80% ($C_\mu = 2.75\%$) **(d)** 100% ($C_\mu = 4.29\%$)

Figure 6.26: PIV data: Average velocity field for the tested blowing coefficients at AoA = 30 degrees, v_∞ = 20 m/s, propeller off

It can be observed on Figure 6.26 that the active flow control becomes detrimental for the separation region reduction by comparing the 0 and 20% blowing cases. The 20% case shows a slight increase of the separation area compared to the unblown case. This result confirms the data also shown by the pressure measurements in subsection 6.2.1. It can be concluded that the separation region has been significantly reduced up to downstream the propeller rotation plane for 80 and 100% with $C_\mu = 2.75\%$ and $C_\mu = 4.29\%$ respectively, with the highest effectiveness shown by the highest value. Furthermore, comparing the low with high C_μ flow field, it can be observed that the flow upstream the blowing slot is accelerated with the increase in the injected air momentum. Hence, the static pressure over the wing is decreased, leading to stronger suction peaks over a larger section of the wing's suction surface. In contrast, the increase of the separation region for the low-momentum injected air results in lower freestream velocity upstream the blowing slot where the flow is still attached, degrading the suction peak of the wing's geometry.

A further observation is a black hump with identical shape near the wall for the 80 and 100% in Figure 6.26c and Figure 6.26d respectively. This is a result from presence of a scratch in the bottom plexiglass surface of the wind-tunnel's test section which significantly disturbs the reflected light from the seeded particles, resulting in a bright spot where the reflected light from the seeded particles in the flow cannot be differentiated. This leads to no velocity data at that location. Unfortunately, this issue has not been able to be resolved within the wind-tunnel campaign duration and the hump can be observed in all PIV results where it is upstream of the separation region.

The data for freestream velocity of 10 m/s for the same conditions is presented Appendix D on Figure D.3. It can be observed that already with the 20% ($C_\mu = 0.69\%$) case, a suppression of the separation region occurs as the separation point is pushed downstream. A complete separation prevention has been achieved for 50% ($C_\mu = 4.29\%$) and higher within the selected ROI. The data agrees with the findings of the 20 m/s condition, where the increase of the blowing coefficient increases the flow velocity upstream the injection slot, and hence, the suction peak. Furthermore, the Coanda effect at the slot is indicated to be effective even at the highest applied coefficient of $C_\mu = 17.17\%$ as no triggering of separation is observed, but only suppression. Interestingly, the 80% ($C_\mu = 10.99\%$) and 100% ($C_\mu = 17.17\%$) shows a maximum velocity region (in red) to be detected at the downstream boundary of the ROI rather than upstream the blowing slot as typically. This could be explained by possibly under-seeded jet with reflective particles and/or too large time difference between the image pairs at these conditions where the particle movement is way too large for the an accurate correlation with the selected Δt which was tuned for unblown cases. Therefore, the presence of the maximum detected velocity at the downstream boundary of the ROI could be due to the jet's local velocity becoming low enough due to the friction forces allowing it to be processed by the software, while the velocity near the wall closer to the blowing slot is underestimated.

The case for angle of attack 25 degrees at 20 m/s freestream velocity is displayed on Figure 6.27. Tested are only 0%, 50%, and 100% of the mass-flow. The blowing conditions here differ from the angle of attack of 30 degrees, as in this case, the natural flow separation point, as predicted in Figure 5.11, occurs at more downstream location. Hence, the blowing slot location distance to the natural separation point is increased.

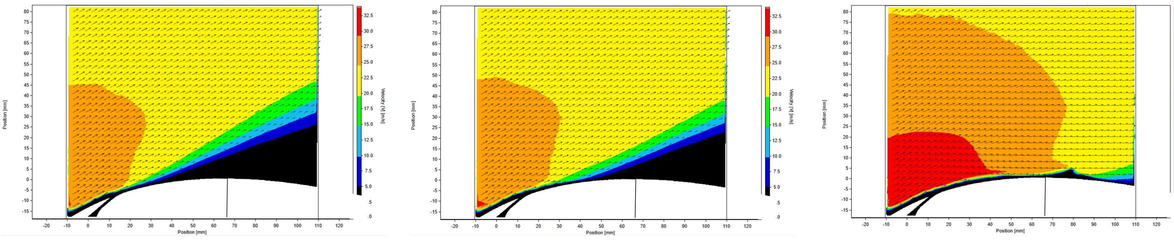

(a) 0% **(b)** 50% ($C_\mu = 1.07\%$) **(c)** 100% ($C_\mu = 4.29\%$)

Figure 6.27: PIV data: Average velocity field for the tested blowing coefficients at AoA = 25 degrees, v_∞ = 20 m/s, propeller off

Analyzing the figures, it is found that the 50% blowing ($C_\mu = 1.07\%$) has a positive effect on pushing the separation point downstream, while the separation region is fully removed at the 100% ($C_\mu = 4.29\%$) case within the ROI. As the 25 degrees angle of attack required the rotation of the propeller-wing assembly to this selected angle, the discussed scratch in the bottom surface of the wind-tunnel's test section has shifted downstream as the relative position to the ROI changes. Based on the results, the threshold for the beneficial C_μ for flow separation region reduction is close to 1.07%. Figure D.4 shows the results for 25 degrees angle of attack at 10 m/s. It is concluded that the separation region is effectively suppressed within the whole ROI already for 50% blowing ($C_\mu = 4.29\%$).

6.2.2. Propeller on

Performed are wind-tunnel tests involving the operational propeller for both active and passive flow control method. The analysis is based on velocity flow fields and profiles at the selected location within the PIV ROI.

PIV: Velocity profiles data

Presented on Figure 6.28 is the PIV data comparison for the velocity profiles at 20 m/s freestream velocity at 30 and 25 degrees angle of attack. It can be observed that all the cases indicate a fully attached flow just upstream of the blade. This is a finding which does not agree with the numerical simulation predictions for the operational case, where the separation point over the suction side of the wing has been estimated to be at about 50 mm from the leading edge with the set propeller advance ratio for the 30 degrees angle condition for example, as displayed in Figure 5.11. This mismatch may be caused by the propeller performance underestimation due to the inaccurate approximation of the airfoil cross-section distribution of the actual blade geometry. Moreover, the total pressure jump prediction of the BEM analysis does not consider the aerodynamic properties of the wing. The wing suction peak accelerates the flow locally and increases the advance ratio at the propeller tip, which would reduce the local blade loading in the BEM model. However, since the experimental data shows that the boundary layer is attached upstream of the propeller, this would suggest that the total pressure jump generated by the propeller-wing interaction exceeds the simplified BEM prediction.

Regarding the blowing effectiveness, it is found that 20% ($C_\mu = 0.17\%$) and passive flow control blowing coefficients lead to a larger thickness of the boundary layer compared to the unblown case. As the boundary layer shape is roughly identical for these two coefficients, it is assumed that the achieved blowing coefficient with the passive control is close to $C_\mu = 0.17\%$ as well. The 50% of the maximum mass-flow is found to give almost the same results as the unblown case. While the near-wall velocity deficit is reduced for 80 and 100% of the maximum mass-flow with $C_\mu = 2.75\%$ and $C_\mu = 4.29\%$ respectively. The greatest uniformity of the propeller inflow velocity profile is observed to be achieved with $C_\mu = 2.75\%$ for 30 degrees angle of attack.

Figure D.2a shows the condition where the freestream is 10 m/s, while maintaining the angle of attack of 30 degrees. The data indicates that the passive flow control and the 20% blowing ($C_\mu = 0.69\%$) result in larger boundary layer thickness than the unblown case, while a thickness reduction is observed for at 50% blowing ($C_\mu = 4.29\%$) or higher. The passive flow control is found to result in the largest boundary layer increase, which suggests that the achieved blowing coefficient is lower than ($C_\mu = 0.69\%$).

The 25 degrees angle of attack data shown on Figure 6.28b indicates that the 50% and the passive flow control are found to lead to an increase in the boundary layer thickness near the wing surface compared to the unblown case. An increase in the near-wall velocity has been observed only at the 100% case. Additionally, the velocity maximums of all profiles have been slightly increased near the wall compared to the 30 degrees angle of attack. Since the profile measurement is taken downstream of the suction peak of the wing, which is upstream the blowing slot, this phenomenon could be explained by the reduced adverse pressure gradient for the lower angle of attack allowing for the airflow to maintain a high momentum for a larger distance past the suction peak.

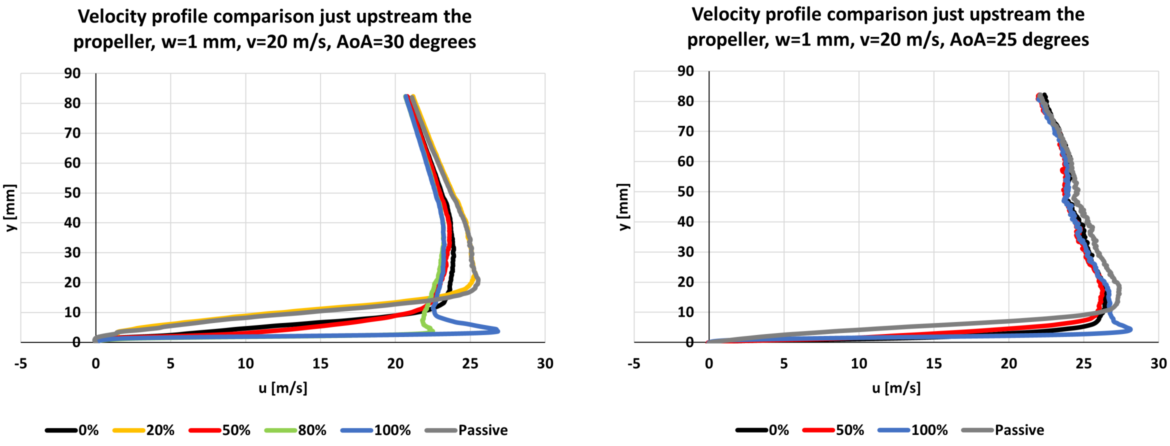

(a) Propeller off, AoA = 30 degrees

(b) Propeller off, AoA = 25 degrees

Figure 6.28: PIV data: Velocity profile comparison at just upstream the propeller blade location at v_∞ = 20 m/s with propeller on

Regarding the freestream velocity of 10 m/s for the same angle on Figure D.2b, improvement of the unblown condition has been achieved by all of the inspected blowing cases including the passive flow control. The unblown profile shows a deficit up to 60 mm away from the wall where it matches with the rest of the data. A deficit dip is formed specifically within 30 to 50 mm away from the wall. This could be due to a measurement error resulting from the propeller influence on the seeded particles at lower velocity where the viscous effects from the propeller blade movement are stronger. Hence, the measurement proximity to the propeller might be too close in this case. An increase in the near-wall velocity has been achieved by the 50% and 100%. The greatest uniformity of the profile has been achieved by the 50% ($C_\mu = 4.29\%$).

PIV: velocity fields data

Presented on Figure 6.29 are the velocity fields at 30 degrees angle of attack at 20 m/s freestream velocity. The comparison also includes the tested condition with a passive flow control.

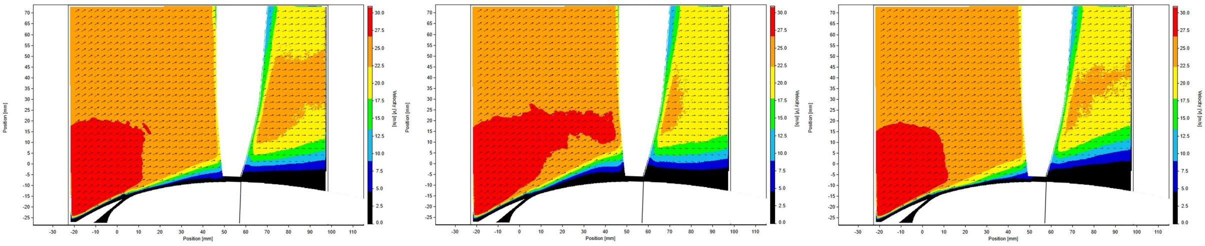

(a) 0%

(b) 20% ($C_\mu = 0.17\%$)

(c) 50% ($C_\mu = 1.07\%$)

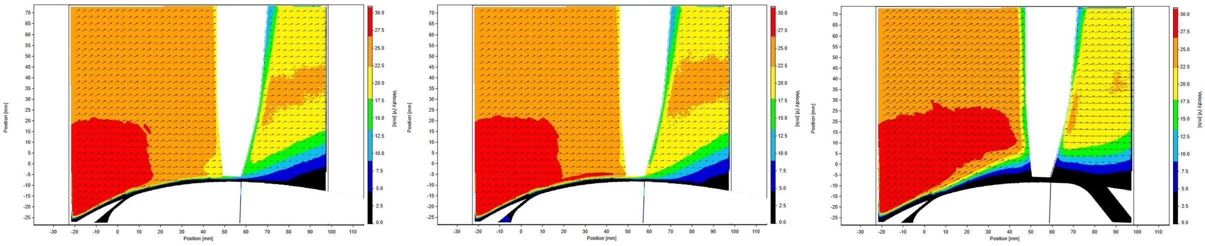

(d) 80% ($C_\mu = 2.75\%$)

(e) 100% ($C_\mu = 4.29\%$)

(f) Passive flow control

Figure 6.29: PIV data: Average velocity field for the tested blowing coefficients at AoA = 30 degrees, v_∞ = 20 m/s, propeller on

Looking at Figure 6.29a, it can be observed that the velocity deficits near the wall begin to increase noticeably near the blowing slot which is also the design location of the blowing slot based on the numerical prediction of the separation point. Similar to the propeller off results, the low blowing coefficient is observed to thicken the boundary layer compared to the unblown case. An increase of low-momentum region upstream the propeller is observed up to the 50% case ($C_\mu = 1.07\%$), while the airflow near the wall is found to be accelerated up to the flow velocity away from the wall upstream the propeller blade for the 80% and 100% cases. The greatest low-velocity suppression near the wall occurs for the 100% as expected due to the greatest energy addition to the boundary layer. However, a notable difference with the propeller off condition on Figure 6.26d is that the suppression is more effective when the propeller is not present for the same blowing coefficient. This could be explained by the fact that the blade passing induces both a flow blockage of the injected air due to the small tip clearance, and an unsteadiness due to the passing frequency which could deflect the injected air direction out of the plane of the analysis. Moreover, the velocity downstream of the propeller is indicated to have a lower magnitude (yellow color) than upstream (orange color). This may be due to the increased freestream velocity by the suction peak of the wing contour, leading to accelerated flow near the wall, which consequently increases the effective advance ratio of the propeller. Hence, the thrust produced may be lower than the BEM prediction which assumes uniform inflow and zero angle of attack. Also, a possible bias of the PIV accuracy could be present downstream the propeller as the seeding particle trajectory is significantly modified by the blade motion, potentially causing reduction of the in-plane particle density and therefore, apparent velocity reduction.

Looking at Figure 6.29f, the passive flow control is observed to increase the boundary layer thickness compared to the unblown case. The velocity field for the passive flow control case is comparable to the 20% ($C_\mu = 0.17\%$) field on Figure 6.29b. The data shows that the boundary layer thickness is increased for the passive flow control while already a slight decrease is observed for the 50% case. Hence, the designed passive flow channel is assumed to produce a blowing coefficient between 0.17% and 1.07%. Further comparing the passive flow control with the 20% and 50% cases, the passive flow control inlet indeed seems to create a flow suction based on the curved shape of the separated flow downstream of the propeller.

Analyzing the case for 10 m/s freestream velocity on Figure D.5 the 20% blowing ($C_\mu = 0.69\%$) is found to result in larger boundary layer thickness, while already with 50% ($C_\mu = 4.29\%$) the low-momentum flow near the wall is fully prevented upstream the propeller blade. Furthermore, the this region has been fully suppressed for the cases of 80% ($C_\mu = 10.99\%$) and 100% ($C_\mu = 17.17\%$) within the ROI despite the propeller presence. Additionally, the passive flow control shows larger boundary layer thickness, indicating for achieved blowing coefficient lower than 0.69%.

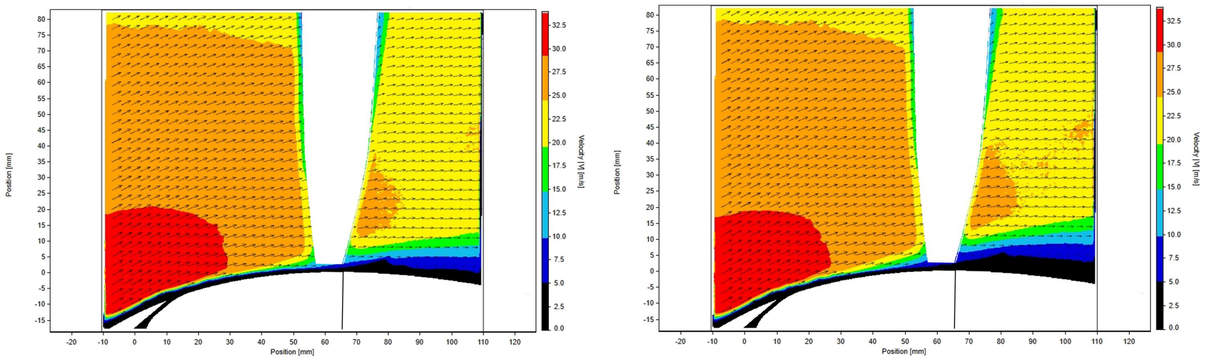

(a) 0%

(b) 50% ($C_\mu = 1.07\%$)

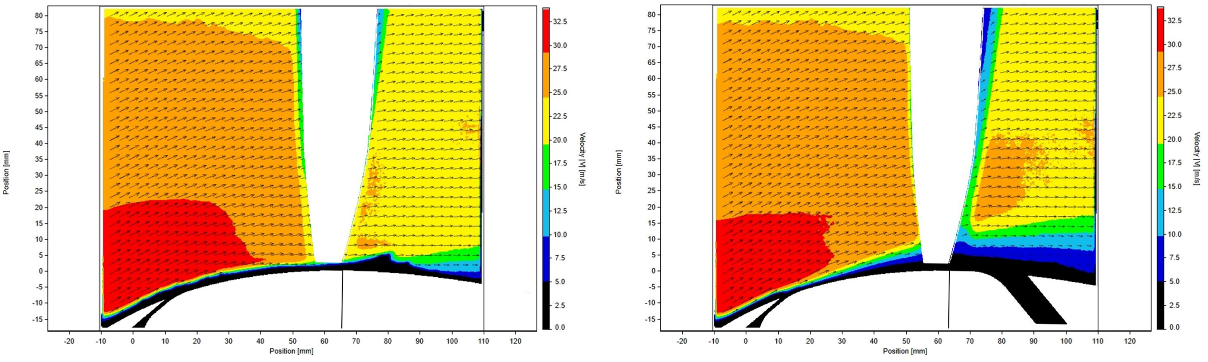

(c) 100% ($C_\mu = 4.29\%$)

(d) Passive flow control

Figure 6.30: PIV data: Average velocity field for the tested blowing coefficients at AoA = 25 degrees, v_∞ = 20 m/s, propeller on

Looking at the 25 degrees condition at 20 m/s on Figure 6.30, similar findings are made as in for the 30 degrees case. The 50% blowing ($C_\mu = 1.07\%$) is observed to show an increase in the boundary layer thickness compared to the unblown case. However, for this lower angle of attack, the 100% case with $C_\mu = 4.29\%$ is found to almost fully suppress the low-momentum area for the entire ROI, which does not occur for the 30 degrees case in Figure 6.29e. This could be explained by the fact that the lower angle of attack reduces the suction peak over the wing surface allowing for more gradual pressure recovery, and hence, larger section of the wing with higher local velocity of the flow for the same amount of injected momentum. The boundary layer with the passive flow control is observed to be increased, indicating for an achieved blowing coefficient lower than 1.07%.

Figure D.6 shows the results for 25 degrees angle of attack at v = 10 m/s. The lower freestream velocity allows for a complete suppression of the distinguishable boundary layer thickness upstream the propeller already at 50% blowing ($C_\mu = 4.29\%$), while this has been achieved in the entire ROI for the 100% case with $C_\mu = 17.17\%$. The passive flow control remains with achieved coefficient lower than required for beneficial effect in decreasing the boundary layer thickness. Instead, it increases it leading to an larger low-momentum area than the unblown case.

7

Conclusion and recommendations for future research

This chapter concludes the findings of the performed research along with the answers of the project's research questions. Additionally, several recommendations are suggested for future work aiming for improvement of the accuracy of the analysis of a similar research topic and setup.

7.1. Conclusions

This document discusses the master thesis project titled ”Towards flow separation control at the lip of a ducted propeller using blowing jet method”. The analysis is based on the flow development over the suction surface of a uniform cross-section wing in proximity to an operational propeller. Performed are numerical and experimental analysis on the propeller-wing configuration. The effectiveness of the blowing jet has been analyzed by application of various blowing coefficients through an inscribed blowing slot in the wing body. The findings of this project might be applicable to both ducted propeller or propeller over-the-wing configuration under high angle of attack. The answers of the sub-research questions are as summarized as follows:

- **How is the ducted propeller performance affected by the duct's geometry?**

  According to the found literature, comparison of the aerodynamic performance of a duct with implemented thick, thin and cambered airfoil cross-section shows that the cambered airfoil provides the largest benefit for the thrust production by the duct. The cambered airfoil also leads to the lowest power required for generating the same amount of thrust and better achievable efficiency than the isolated propeller. In terms of the leading edge geometry, it is reported that the best trade-off for both static and forward flight condition is shown by a small leading edge that is skewed towards the exterior contour of the duct, allowing the pressure gradient to change gradually. Additionally, a small leading edge radius and shorter chord length of the inlet lip would benefit the forward flight with the reduction of the adverse pitching moment, lateral forces, surface friction and pressure drag, while still being able to prevent the formation of tip vortices. On the other hand, the larger radius would be benefit the static condition allowing the flow to be attached and increase the thrust.

- **How is the propeller's advance ratio affecting the performance of the duct?**

  Due to the dominating viscous forces of the duct's internal flow at high advance ratio, the duct becomes disadvantageous for net total thrust production by the ducted compared to an isolated propeller. At low advance ratios, a ducted propeller can generate more thrust than an isolated propeller for the same power input. The duct lip, depending on its geometry and the inflow conditions, accelerates the incoming flow and induces a region of low static pressure upstream of the lip, which contributes to the total thrust production.

- **How does the tip clearance affect the propeller loading?**

  According to found literature, the propeller loading increases towards the blade tips as the tip clearance decreases. More specifically, decreasing the tip clearance allows for greater blade tip vortex suppression, leading to a greater total pressure jump. As the tip vortices are effectively suppressed, the blade tip section of the propeller approaches the local 2D airfoil aerodynamic properties.

- **How should the flow control performance be experimentally analyzed?**

  The flow control is analyzed most effectively by observing the velocity profiles just upstream of the propeller blade for both active and inactive propeller case. This way the flow separation region can be assessed quantitatively instead of solely observing the flow field in the region of interest. However, a qualitative method for flow visualization such as tufts, positioned at key locations on the wing surface, provides an additional insight into the blowing jet influence both within and outside the blowing span over the wing at different blowing coefficients.

- **How is the range of angle of attack of interest limited?**

  The range of the angle of attack in this project is limited such that the separation point occurs within the boundaries of the insert of the wing, while still upstream of the rotation plane of the propeller. Furthermore, the most upstream flow separation point is also limited by the structural consideration for the blowing slot to be manufactured within the insert's boundaries too so that the injected jet is applied just upstream the separation point as recommended by literature.

- **How can the separation point be reasonably approximated?**

  The separation point over the wing suction surface is reasonably approximated by a numerical study of the plane of interest in the intended approximated experimental setup. Literature findings suggest the suitable RANS turbulent models for flow separation prediction could be considered the SST $k-\omega$ and Spalart-Allmaras turbulence models, together with a computational mesh that satisfies the $y^{+}=1$ condition such that the viscous sub-layer of the boundary layer can be resolved. The propeller total pressure jump has been implemented in the CFD study by an actuator line based on BEM analysis prediction, while ignoring the Prandtl tip correction to account for the presence of the duct. The plane of interest of the experimental study has been selected to be at the mid-span of the propeller-wing assembly, where the minimum tip clearance and region of interest are selected to be due to the minimized influence of the flow development near the wingtips, allowing for maximized 2D-flow condition.

- **What is the blowing coefficient's influence on the flow separation with variation of the angle of attack and freestream velocity?**

  The obtained data suggests that the threshold for effective blowing coefficient for flow separation reduction could be reduced with the decrease of the angle of attack. This is assumed to be due to the more gradual pressure gradient at lower angle of attack, allowing for the injected momentum to remain effective over a larger chord-wise distance. The reduction of the freestream velocity has a similar effect on the threshold, as the flow separation point is found to be pushed downstream at lower coefficient compared to at higher freestream velocity.

- **How should a passive flow control method such as a flow channel be implemented to contribute to separation prevention at the lip for the entire investigated range of angle of attack?**

  The passive flow channel designed to recirculate captured mass-flow from the propeller slipstream using Coanda effect back to the blowing slot showed incapability of flow separation reduction. It is assumed that this is caused by the steep angle of the flow channel inlet, causing strong deviation from an optimal angle for the Coanda effect. Additionally, the flow channel inlet is immersed in the flow separation region, which significantly disturbs the inflow velocity in the passive channel. Based on the obtained velocity fields, the achieved blowing coefficient with the designed passive flow control is about $C_\mu \approx 0.17\%$ at freestream velocity of 20 m/s and lower than $C_\mu = 0.69\%$ at 10 m/s, which showed an increase of the separation region rather than suppressing it. Hence, the answer to this question has not been found in this research. However, recommendations are made further in the document how such method could show beneficial results.

Active and passive flow control have been designed and experimentally analyzed. Various blowing coefficients have been tested at 10 and 20 m/s freestream velocity. Based on the obtained velocity profile data at several chord-wise locations, it is observed that a low-blowing coefficient promotes earlier separation or an increase of the boundary layer thickness compared to the unblown case. It has been found that the predictions for the separation point by the numerical analysis do not match which may be caused by the selected approximation of the propeller blade geometry in the analysis. The evaluated velocity profiles just upstream of the operating propeller indicate that the threshold of flow boundary layer thickness reduction compared to the unblown case is achieved between 1.21% and 2.75%. These measurements are taken at 11.67% of the wing chord length downstream of the blowing slot. The findings in this project indicate for a match with found literature also reporting for observed threshold of blowing coefficient of 2.5% near the leading edge to have a beneficial impact on flow separation reduction. However, the obtained data show a reduction of the beneficial blowing coefficient to just 0.69% for a flow separation mitigation at lower freestream velocity, while lowering the angle of attack reduces it to 1.07%. This is expected due to the resulting weaker adverse pressure gradient, allowing for the blowing jet to remain effective over larger section of the wing. The suggested mechanism by which low-momentum blowing triggers separation is that the addition of low-momentum air near the wall reduces the boundary-layer momentum, destabilizing the boundary layer and causing the separation point to shift upstream. Hence, the answer to the main research question of this project can be summarized as:

How effective is a near-wall blowing jet method for preventing flow separation at the lip of a ducted propeller?:

When positioned at 11.67% of the duct's chord length upstream of the propeller and just upstream of the separation point, the near-wall blowing jet is expected to show a beneficial effect on the flow separation region reduction at the lip of a ducted propeller at a blowing coefficient of at least $C_\mu = 2.75\%$. The threshold where the blowing coefficient becomes beneficial for flow separation reduction is found to be in the range of 1.07%-2.75%. However, in case the angle of attack or the freestream velocity is lowered, this effective threshold could also be reduced.

7.2. Recommendations for future research

Several recommendations are suggested for improving the methodology and data accuracy in the reported analysis in this document. They are grouped in numerical - and experimental analysis recommendations and are listed as follows:

7.3. Numerical analysis

- **Propeller pressure jump estimation:** The airfoil cross-section distribution of the propeller blade is approximated based on open literature and attempted to be represented by available typical propeller airfoils in the JavaProp solver. Using the exact airfoil aerodynamic properties is expected to lead to better total pressure jump estimation. Additionally, using BEM analysis with ignored Prandtl tip correction is a first order estimation of the pressure jump produced by the propeller. However, this estimation does not consider the angle of attack of the propeller with respect to the freestream. At non-zero angle of attack the inflow velocity varies azimuthally at the propeller plane, and hence the loading of the propeller. A higher order accuracy of pressure jump estimation is expected to improve the match between the numerical and experimental results.
- **Mesh minimum angle:** The mesh used to perform the CFD simulations for estimation of the separation point over the suction surface of the wing is highly skewed at the pressure side of the wing where the upstream wall contacts the wing even at 30 degrees angle of attack. This issue becomes more pronounced for simulations involving lower angles of attack. Hence, an unstructured mesh might be considered to improve the orthogonality of the mesh, and therefore, enhancing the accuracy of the separation point location.
- **Upstream wall boundary layer:** The assumption of 1 meter no-slip wall length upstream the propeller-wing assembly aims for development of a boundary layer which would approximately recreate the one at the wind-tunnel's nozzle and test-section wall. A better prediction by the CFD results might be achieved by implementing more accurate velocity profile data that the propeller-wing assembly faces at the selected wind-tunnel setup.
- **Flow channel connectors + wind tunnel setup equipment implementation:** The blowing and suction connectors attached on the pressure side of the wing have been assumed to not significantly influence the flow development over the suction surface of the wing as they are positioned at the air stagnation area between the pressure side of the wing and the wind-tunnel's upstream

wall. Nevertheless, their flow blockage effect might still be worth to be considered. Hence, their bodies are recommended to be implemented in the numerical simulation model as they are directly immersed in the freestream airflow, with special attention to the blowing connector. Additionally, despite not being directly immersed into the freestream airflow, flow blockage is caused by setup equipment such as the structure used to support the mass-slow regulator, and the total pressure probe. Hence, the model accuracy could be maximized by implementation of all the equipment which is to be used in the wind-tunnel setup.

- **Simulation of a full-scale ducted propeller:** Analyzing the blowing coefficient effect on the flow development at the midspan of a wing does not represent the flow condition in a ducted propeller accurately. The numerical analysis is expected to give the best match with a ducted propeller in case the separation point is evaluated at a 3D accurate ducted propeller geometry.

7.4. Experimental analysis

- **Larger wingspan:** The wind-tunnel results in this report are obtained by a wing of 564 mm in length so that it can fit with the two of 18 mm thick mounting plates within the height of the test-section. Suggested is that the study might further increase the accuracy of validating a 2D numerical study results by further minimizing the three-dimensionality of the flow over the wing's suction surface. This could be achieved by using a larger wing span of the model bringing the wingtip vortices and test-section's boundary layer development further away from the blowing slot region. This is expected to additionally improve the match of the conditions in the 2D numerical analysis.
- **Symmetric mounting design:** Using a hole through only one of the mounting plates such that 2D PIV flow visualization technique can be performed promotes asymmetry between the flow boundary layer at the top and bottom mounting plates, which is expected to influence the global development of the flow for the propeller-wing assembly. Hence, it is recommended that the future similar research prevents any potential mounting asymmetry for all performed wind-tunnel tests.
- **Uniform tip clearance:** Similar to the numerical analysis recommendation, performing the experimental tests on a full-scale ducted propeller would enable maximizing the accuracy of the blowing jet effectiveness due to symmetry in the tip clearance, and hence, achieving uniform loading of the propeller. Specially, this would allow the estimation of the captured mass-flow by the passive flow inlet more reasonable as the pressure jump could be assumed to be equal along its entire span rather than just a single location as in this project.
- **Thinner propeller-wing support structure:** To minimize flow blockage at the propeller-wing assembly, the mounting setup is recommended to be made as thin as possible while still being able to provide sufficient structural support during the tests. For instance, a good candidate would be to use carbon fiber material for the propeller drive support inside the test-section. It would allow the support structure to be sufficiently strong while having minimal frontal area leading to minimizing the drag of the structure.
- **Short passive flow channel:** The length of the air tube connecting the inlet and outlet of the passive flow channel has been selected such that it can be conveniently implemented in the test-setup so a concept of passive flow channel is tested. However, to maximize the recirculated mass-flow rate in the flow channel, it is recommended the length of the flow channel to be minimized such that the kinetic energy losses of the captured dynamic pressure within the channel are also minimized until the captured air reaches the blowing slot. This would therefore, maximize the blowing velocity and therefore, effectiveness of the passive flow control.
- **Lower angle of flow channel inlet:** The Coanda effectiveness of the flow channel inlet of capturing mass-flow from the propeller slipstream near the wing surface is expected to be improved by lowering the angle of the slot with respect to the local curvature of the wing. This would allow the mitigation of the adverse pressure gradients at the channel inlet, leading to better attachment of the flow to its walls, reducing the total pressure loss due to potential separation at the inlet. Another potential option for maximizing the effectiveness of the passive flow channel would be to implement a ram intake, which would not rely on Coanda effect to re-direct mass-flow in the channel. Instead, the inlet would be positioned normal to the wing surface such that it is directly immersed in the external (higher momentum) flow. A disadvantage of this method would be the separation region that the intake would create downstream of its body, which leads to an aerodynamic inlet shape optimization challenge.

- **Equal mass-flow injection along the blowing span:** As described in the document, the approximate mass-flow equalization using assumed velocity ratios based on recommended 1/7th power law is prone to high uncertainty for the equal mass-flow distribution between all the blowing holes along the span of the blowing connector. The accuracy of the impact of the blowing coefficient may be improved if the injected mass-flow does not vary along the slot's span. Hence, it is recommended a higher-fidelity mass-flow estimation methods such as CFD analysis of the connector design to be used such that the variation of the injected mass-flow to be prevented along the blowing span and potentially minimizing the unsteadiness of the velocity profile downstream the blowing slot.
- **Smaller tip clearance:** As indicated by the found literature, decreasing the tip clearance is expected to increase the propeller loading towards the tip. It is suggested that the implemented tip clearance to be as close to zero as long as vibrations concern of the propeller-wing assembly would allow it, preventing any physical interaction between the propeller and the wing. This way the pressure jump at the blade tip is expected to be maximized. This would potentially lead to an increase passive flow channel inlet velocity and therefore, the passive flow channel effectiveness in suppressing the flow separation.

References

[1] James Vaughan. *1966 ... Bell VTOL X-22*. Licensed under Creative Commons Attribution-NonCommercial-ShareAlike 2.0, `https://creativecommons.org/licenses/by-nc-sa/2.0/`. 2011. URL: `https://www.flickr.com/photos/x-ray_delta_one/5433031782/`.

[2] Vinayak Ramachandran Nambiar and Vassilios Pachidis. “Nacelle intake flow separation reduction at cruise condition using active flow control”. In: *Propulsion and Power Research* 11.3 (2022), pp. 337–352. ISSN: 2212-540X. DOI: `https://doi.org/10.1016/j.jppr.2022.07.005`. URL: `https://www.sciencedirect.com/science/article/pii/S2212540X2200061X`.

[3] L.L.M.Veldhuis. “Propeller Wing Aerodynamic Interference”. PhD thesis. Delft University of Technology, Month 2005. DOI: `DOIifavailable`. URL: `URL%20if%20online`.

[4] Snorri Gudmundsson. “Chapter 14 - The Anatomy of the Propeller”. In: *General Aviation Aircraft Design*. Ed. by Snorri Gudmundsson. Boston: Butterworth-Heinemann, 2014, pp. 581–659. ISBN: 978-0-12-397308-5. DOI: `https://doi.org/10.1016/B978-0-12-397308-5.00014-3`. URL: `https://www.sciencedirect.com/science/article/pii/B9780123973085000143`.

[5] N. van Arnhem. “Unconventional Propeller−Airframe Integration for Transport Aircraft Configurations”. PhD thesis. Delft University of Technology, Month 2022. DOI: `DOIifavailable`. URL: `URL%20if%20online`.

[6] Jason Pereira. “Hover and wind-tunnel testing of shrouded rotors for improved micro air vehicle design”. In: (Jan. 2008).

[7] T. Sinnige. “Aerodynamic and Aeroacoustic Interaction Effects for Tip-Mounted Propellers”. PhD thesis. Delft University of Technology, Month 2018. DOI: `DOIifavailable`. URL: `URL%20if%20online`.

[8] Snorri Gudmundsson. “Chapter 15 - Thrust Modeling for Propellers”. In: *General Aviation Aircraft Design (Second Edition)*. Ed. by Snorri Gudmundsson. Second Edition. Butterworth-Heinemann, 2022, pp. 597–656. ISBN: 978-0-12-818465-3. DOI: `https://doi.org/10.1016/B978-0-12-818465-3.00015-X`. URL: `https://www.sciencedirect.com/science/article/pii/B978012818465300015X`.

[9] H. F. Mourão Bento. “Aerodynamic interaction effects of circular and square ducted propellers”. MSc Thesis. Delft, The Netherlands: Delft University of Technology, May 2019.

[10] N.H.M. van den Dungen. “Synthesis of an Aircraft Featuring a Ducted-Fan Propulsive Empennage”. MSc Thesis. Delft, The Netherlands: Delft University of Technology, Apr. 2017.

[11] Delft University of Technology. *Flight Performance and Propulsion*. n.d. URL: `https://www.tudelft.nl/en/ae/organisation/departments/flow-physics-and-technology/flight-performance-propulsion/research/flight-performance-and-propulsion`.

[12] T. Zhang and G.N. Barakos. “Review on ducted fans for compound rotorcraft”. In: *The Aeronautical Journal* 124.1277 (2020), pp. 941–974. DOI: `10.1017/aer.2019.164`.

[13] “Investigation of Pneumatic Inlet and Diffuser Blowing on a Ducted Fan Propulsor in Static Thrust Operation”. In: *NASA Langley Research Center* (2003). URL: `https://ntrs.nasa.gov/citations/20040001424`.

[14] Anita I. Abrego and Robert W. Bulaga. “Performance Study of a Ducted Fan System”. In: *Ames Research Center* (Jan. 2002).

[15] Will E. Graf. “Effects of Duct Lip Shaping and Various Control Devices on the Hover and Forward Flight Performance of Ducted Fan UAVs”. Master of Science thesis. Blacksburg, Virginia: Faculty of Virginia Polytechnic Institute and State University, 2005.

[16] Michael Cerny and Christian Breitsamter. “A Comparison of Isolated and Ducted Fixed-Pitch Propellers under Non-Axial Inflow Conditions”. In: *Aerospace* 7.8 (2020). ISSN: 2226-4310. DOI: `10.3390/aerospace7080112`. URL: `https://www.mdpi.com/2226-4310/7/8/112`.

[17] Seyit Türkmen Koç et al. “Experimental Investigation of a Ducted Propeller”. In: *EUCASS association* (2011).

[18] Ali Akturk and Cengiz Camci. “Lip Separation and Inlet Flow Distortion Control in Ducted Fans Used in VTOL Systems”. In: June 2014. DOI: `10.1115/GT2014-26249`.

[19] Preston Martin and Chee Tung. “Performance and Flowfield Measurements on a 10-inch Ducted Rotor VTOL UAV”. In: *Army/NASA Rotorcrafi Division Aeroflightdynamics directorate, AVRDEC US Army Research, Development. and Engineering Command Ames Research Center* (2004).

[20] Kewei Xu, Yan Ren, and Gecheng Zha. “Separation Control by Co-Flow Wall Jet”. In: *AIAA AVIATION 2021 FORUM*. DOI: `10.2514/6.2021-2946`. eprint: `https://arc.aiaa.org/doi/pdf/10.2514/6.2021-2946`. URL: `https://arc.aiaa.org/doi/abs/10.2514/6.2021-2946`.

[21] M. Gad-el-Hak. *Flow Control, Passive, Active, and Reactive Flow Management*. Cambridge University Press, 2000. DOI: `10.1017/CBO9780511529535`.

[22] L. Prandtl. “The Mechanics of Viscous Fluids”. In: *Aerodynamic Theory*. Ed. by W. F. Durand. Vol. III. Berlin: J. Springer, 1935.

[23] Sufianu Aliu et al. “2 - Mechanisms of heat transfer and boundary layers”. In: *Applications of Heat, Mass and Fluid Boundary Layers*. Ed. by R.O. Fagbenle et al. Woodhead Publishing Series in Energy. Woodhead Publishing, 2020, pp. 23–53. ISBN: 978-0-12-817949-9. DOI: `https://doi.org/10.1016/B978-0-12-817949-9.00010-4`. URL: `https://www.sciencedirect.com/science/article/pii/B9780128179499000104`.

[24] Snorri Gudmundsson. “Chapter 8 - The Anatomy of the Airfoil”. In: *General Aviation Aircraft Design*. Ed. by Snorri Gudmundsson. Boston: Butterworth-Heinemann, 2014, pp. 235–297. ISBN: 978-0-12-397308-5. DOI: `https://doi.org/10.1016/B978-0-12-397308-5.00008-8`. URL: `https://www.sciencedirect.com/science/article/pii/B9780123973085000088`.

[25] Paul K. Chang. “Separation of flow”. In: *Journal of the Franklin Institute* 272.6 (1961), pp. 433–448. ISSN: 0016-0032. DOI: `https://doi.org/10.1016/0016-0032(61)90875-4`. URL: `https://www.sciencedirect.com/science/article/pii/0016003261908754`.

[26] Ali Akturk and Cengiz Camci. “Tip Clearance Investigation of a Ducted Fan Used in VTOL Unmanned Aerial Vehicles- Part I: Baseline Experiments and Computational Validation”. In: *Journal of Turbomachinery* 136 (May 2022), pp. 021004–1. DOI: `10.1115/1.402346`.

[27] Cengiz Camci and Ali Akturk. “TIP-LEAKAGE VORTEX MINIMIZATION IN DUCTED AXIAL FANS USING NOVEL PRESSURE SIDE TIP PLATFORM EXTENSIONS”. In: May 2022.

[28] Minhyoung RYU, Leesang CHO, and Jinsoo CHO. “The Effect of Tip Clearance on Performance of a Counter-Rotating Ducted Fan in a VTOL UAV”. In: *TRANSACTIONS OF THE JAPAN SOCIETY FOR AERONAUTICAL AND SPACE SCIENCES* 60.1 (2017), pp. 1–9. DOI: `10.2322/tjsass.60.1`.

[29] Choon-Man Jang, Masato Furukawa, and Masahiro Inoue. “Analysis of Vortical Flow Field in a Propeller Fan by LDV Measurements and LES—Part II: Unsteady Nature of Vortical Flow Structures Due to Tip Vortex Breakdown”. In: *Journal of Fluids Engineering-transactions of The Asme* 123 (2001), pp. 755–761. URL: `https://api.semanticscholar.org/CorpusID:123603905`.

[30] Ian N. Moyle. “Discussion: “Tip Leakage Flow in Axial Compressors” (Storer, J. A., and Cumpsty, N. A., 1991, ASME J. Turbomach., 113, pp. 252–259)”. In: *Journal of Turbomachinery-transactions of The Asme* 113 (1991), pp. 259–259. URL: `https://api.semanticscholar.org/CorpusID:120746795`.

[31] Seyed Mohsen Alavi Moghadam, Matthias Meinke, and Wolfgang Schröder. “Analysis of tip-leakage flow in an axial fan at varying tip-gap sizes and operating conditions”. In: *Computers Fluids* 183 (2019), pp. 107–129. ISSN: 0045-7930. DOI: `https://doi.org/10.1016/j.compfluid.2019.01.014`. URL: `https://www.sciencedirect.com/science/article/pii/S0045793019300088`.

[32] Reinier Goudswaard. “Aerodynamic performance of a small-scale ducted rotor in hover”. Master’s thesis. Delft University of Technology, 2021.

[33] Reinier J. Goudswaard, Daniele Ragni, and Woutijn J. Baars. “Effects of the rotor tip gap on the aerodynamic and aeroacoustic performance of a ducted rotor in hover”. In: *Aerospace Science and Technology* 155 (2024), p. 109734. ISSN: 1270-9638. DOI: `https://doi.org/10.1016/j.ast.2024.109734`. URL: `https://www.sciencedirect.com/science/article/pii/S1270963824008630`.

[34] Z. Li, Q. Wang, and T. Wang. “Analysis of Axial-Flow and Tilt Aerodynamic Characteristics of Ducted Propellers”. In: *Open Journal of Applied Sciences* 15 (2025), pp. 700–714. DOI: `10.4236/ojapps.2025.153045`. URL: `https://www.scirp.org/journal/paperinformation?paperid=141406`.

[35] Yu Hu et al. “Hovering efficiency optimization of ducted propeller with large blade tip clearance based on grooved duct configuration”. In: *Aerospace Science and Technology* 150 (2024), p. 109226. ISSN: 1270-9638. DOI: `https://doi.org/10.1016/j.ast.2024.109226`. URL: `https://www.sciencedirect.com/science/article/pii/S1270963824003572`.

[36] Piotr Lampart. “Tip leakage flows in turbines”. In: *TASK QUARTERLY* 10 (Jan. 2006), pp. 139–175.

[37] Cengiz Camci and Ali Akturk. “Tip Clearance Investigation of a Ducted Fan Used in VTOL UAVs, Part 2: Novel Treatments via Computational Design and Their Experimental Verification”. In: *Journal of Turbomachinery* 136 (Feb. 2014), p. 021005. DOI: `10.1115/1.4023469`.

[38] Larry A. Young. “Novel Tilting Ducted-Fan Aerial Vehicle Configurations”. In: *NASA Ames Research Center* (2023).

[39] V. Dighe et al. “Ducted wind turbines in yawed flow: a numerical study”. In: *Wind Energy Science* 6.5 (2021), pp. 1263–1275. DOI: `10.5194/wes-6-1263-2021`. URL: `https://wes.copernicus.org/articles/6/1263/2021/`.

[40] Ge-Cheng Zha, Wei Gao, and Craig D. Paxton. “Jet Effects on Coflow Jet Airfoil Performance”. In: *AIAA Journal* 45.6 (2007), pp. 1222–1231. DOI: `10.2514/1.23995`. eprint: `https://doi.org/10.2514/1.23995`. URL: `https://doi.org/10.2514/1.23995`.

[41] T. L. Chng et al. “Flow Control of an Airfoil via Injection and Suction”. In: *Journal of Aircraft* 46.1 (2009), pp. 291–300. DOI: `10.2514/1.38394`. eprint: `https://doi.org/10.2514/1.38394`. URL: `https://doi.org/10.2514/1.38394`.

[42] Ge-Cheng Zha et al. “High Performance Airfoil Using Co-Flow Jet Flow Control”. In: *43rd AIAA Aerospace Sciences Meeting and Exhibit*. DOI: `10.2514/6.2005-1260`. eprint: `https://arc.aiaa.org/doi/pdf/10.2514/6.2005-1260`. URL: `https://arc.aiaa.org/doi/abs/10.2514/6.2005-1260`.

[43] Brian Launder and W Rodi. “The Turbulent Wall Jet Measurements and Modeling”. In: *Annual Review of Fluid Mechanics* 15 (Nov. 2003), pp. 429–459. DOI: `10.1146/annurev.fl.15.010183.002241`.

[44] Ruochen Wang et al. “Effects of Key Parameters on Airfoil Aerodynamics Using Co-Flow Jet Active Flow Control”. In: *Aerospace* 9.11 (2022). ISSN: 2226-4310. DOI: `10.3390/aerospace9110649`. URL: `https://www.mdpi.com/2226-4310/9/11/649`.

[45] Aman Jindal et al. “Numerical Analysis of Pylon-Blowing Systems for Pusher-Propeller Applications”. In: *35th AIAA Applied Aerodynamics Conference*. DOI: `10.2514/6.2017-3908`. eprint: `https://arc.aiaa.org/doi/pdf/10.2514/6.2017-3908`. URL: `https://arc.aiaa.org/doi/abs/10.2514/6.2017-3908`.

[46] C. Wang and M. Sun. “Separation control on a thick airfoil with multiple slots blowing at small speeds”. In: *ACTA MECHANICA* (1999).

[47] Avraham Seifert et al. “Oscillatory Blowing: A Tool to Delay Boundary-Layer Separation”. In: *Aiaa Journal - AIAA J* 31 (Jan. 1993), pp. 2052–2060. DOI: `10.2514/3.49121`.

[48] Avraham Seifert, A. Darabi, and I. Wyganski. “Delay of airfoil stall by periodic excitation”. In: *Journal of Aircraft - J AIRCRAFT* 33 (July 1996), pp. 691–698. DOI: `10.2514/3.47003`.

[49] Junkyu Kim et al. “Numerical Investigation of Jet Angle Effect on Airfoil Stall Control”. In: *Applied Sciences* 9.15 (2019). ISSN: 2076-3417. DOI: `10.3390/app9152960`. URL: `https://www.mdpi.com/2076-3417/9/15/2960`.

[50] Claude G. Matalanis et al. “Combustion-Powered Actuation for Dynamic-Stall Suppression: High-Mach Simulations and Low-Mach Experiments”. In: *AIAA Journal* 53.8 (2015), pp. 2151–2163. DOI: `10.2514/1.J053641`. eprint: `https://doi.org/10.2514/1.J053641`. URL: `https://doi.org/10.2514/1.J053641`.

[51] Timothée Chabert et al. “Experimental detection of flow separation over a plain flap by wall shear stress analysis with and without steady blowing”. en. In: *Comptes Rendus. Mécanique* 342.6-7 (2014), pp. 389–402. DOI: `10.1016/j.crme.2014.01.013`.

[52] N. Ganesh, S. ARUNVINTHAN, and S. NADARAJA PILLAI. “Effect of surface blowing on aerodynamic characteristics of tubercled straight wing”. In: *Chinese Journal of Aeronautics* 32.5 (2019), pp. 1111–1120. ISSN: 1000-9361. DOI: `https://doi.org/10.1016/j.cja.2019.02.006`. URL: `https://www.sciencedirect.com/science/article/pii/S1000936119300950`.

[53] Chunmei Chen, Roman Seele, and Israel Wygnanski. “Separation and Circulation Control on an Elliptical Airfoil by Steady Blowing”. In: *AIAA Journal* 50.10 (2012), pp. 2235–2247. DOI: `10.2514/1.J051538`. eprint: `https://doi.org/10.2514/1.J051538`. URL: `https://doi.org/10.2514/1.J051538`.

[54] Hanns F. Müller-Vahl et al. “Control of Thick Airfoil, Deep Dynamic Stall Using Steady Blowing”. In: *AIAA Journal* 53.2 (2015), pp. 277–295. DOI: `10.2514/1.J053090`. eprint: `https://doi.org/10.2514/1.J053090`. URL: `https://doi.org/10.2514/1.J053090`.

[55] Ruochen Wang et al. “Effects of Key Parameters on Airfoil Aerodynamics Using Co-Flow Jet Active Flow Control”. In: *Aerospace* 9.11 (2022). ISSN: 2226-4310. DOI: `10.3390/aerospace9110649`. URL: `https://www.mdpi.com/2226-4310/9/11/649`.

[56] Jasper Tomas et al. “Numerical simulation of flow control by synthetic jet actuation”. In: *27th Congress of the International Council of the Aeronautical Sciences 2010, ICAS 2010* 2 (Jan. 2010), pp. 1278–1287.

[57] Guoqing Zhao and Qijun Zhao. “Parametric analyses for synthetic jet control on separation and stall over rotor airfoil”. In: *Chinese Journal of Aeronautics* 27.5 (2014), pp. 1051–1061. ISSN: 1000-9361. DOI: `https://doi.org/10.1016/j.cja.2014.03.023`. URL: `https://www.sciencedirect.com/science/article/pii/S1000936114000557`.

[58] Yash Raj et al. “The Coanda Effect Unveiled: Compressible and Viscous Flow Dynamics in Aerodynamics and Coaxial Jet Mixing”. In: *AIAA SCITECH 2025 Forum*. DOI: `10.2514/6.2025-0570`. eprint: `https://arc.aiaa.org/doi/pdf/10.2514/6.2025-0570`. URL: `https://arc.aiaa.org/doi/abs/10.2514/6.2025-0570`.

[59] Prabhu Kankatala and Galih Bangga. “Active Separation Control on Thick Wind Turbine Airfoils by Means of Steady and Unsteady Blowing”. In: *Advanced Theory and Simulations* 2.7 (2019), p. 1900077. DOI: `https://doi.org/10.1002/adts.201900077`. eprint: `https://advanced.onlinelibrary.wiley.com/doi/pdf/10.1002/adts.201900077`. URL: `https://advanced.onlinelibrary.wiley.com/doi/abs/10.1002/adts.201900077`.

[60] Kunal Puri et al. “Computations of Active Flow Control Via Steady Blowing Over a NACA-0018 Airfoil: Implicit LES and RANS Validated Against Experimental Data”. In: *2018 AIAA Aerospace Sciences Meeting*. DOI: `10.2514/6.2018-0792`. eprint: `https://arc.aiaa.org/doi/pdf/10.2514/6.2018-0792`. URL: `https://arc.aiaa.org/doi/abs/10.2514/6.2018-0792`.

[61] Claude G. Matalanis et al. “High-Speed Experiments on Combustion-Powered Actuation for Dynamic Stall Suppression”. In: *AIAA Journal* 55.9 (2017), pp. 3001–3015. DOI: `10.2514/1.J055700`. eprint: `https://doi.org/10.2514/1.J055700`. URL: `https://doi.org/10.2514/1.J055700`.

[62] Qingxi Li et al. “Design and Experimental Validation of Swirl Recovery Vanes for Propeller Propulsion Systems”. In: *AIAA Journal* 56.12 (2018), pp. 4719–4729. DOI: `10.2514/1.J057113`.

[63] Tom C. A. Stokkermans and Leo L. M. Veldhuis. “Propeller Performance at Large Angle of Attack Applicable to Compound Helicopters”. In: *AIAA Journal* 59.6 (2021), pp. 2183–2199. DOI: `10.2514/1.J059509`.

[64] *Clark Y (smoothed) Airfoil (clarkysm-il)*. `http://airfoiltools.com/airfoil/details?airfoil=clarkysm-il`. Accessed: 14 August 2025.

[65] *Eppler 193 Airfoil (e193-il)*. `http://airfoiltools.com/airfoil/details?airfoil=e193-il`. Accessed: 14 August 2025.

[66] *ARA-D 6% Airfoil (arad6-il)*. `http://airfoiltools.com/airfoil/details?airfoil=arad6-il`. Accessed: 14 August 2025.

[67] Emmanuel Branlard. *Wind Turbine Aerodynamics and Vorticity-Based Methods*. Vol. 7. Jan. 2017. ISBN: 978-3-319-55163-0. DOI: `10.1007/978-3-319-55164-7`.

[68] David Marten. “QBlade: A Modern Tool for the Aeroelastic Simulation of Wind Turbines”. PhD thesis. Oct. 2020. DOI: `10.14279/depositonce-10646`.

[69] *Blade section — QBlade Documentation*. 2025. URL: `https://docs.qblade.org/src/user/blade/blade.html`.

[70] Martin Hepperle. *JavaProp Users Guide*. Version: August 2018. MH AeroTools. 2018. URL: `https://www.mh-aerotools.de/airfoils/javaProp.htm`.

[71] J.J. van Egmond. "Passive Flow Separation Control for High Lift: An Experimental Investigation on a Novel Vortex Generator". Master's thesis. Delft, The Netherlands: Delft University of Technology, Dec. 2015.

[72] Neal Gallagher. *Savitzky-Golay Smoothing and Differentiation Filter*. Jan. 2020. DOI: `10.13140/RG.2.2.20339.50725`.

[73] S. Lu, J. Liu, and R. Hekkenberg. "Mesh properties for RANS simulations of airfoil-shaped profiles: A case study of rudder hydrodynamics". In: *Journal of Marine Science and Engineering* 9.10 (2021), Article 1062. DOI: `10.3390/jmse9101062`.

[74] Christopher T. Lee et al. "The Implementation of the Colored Abstract Simplicial Complex and Its Application to Mesh Generation". In: 45.3 (Aug. 2019). ISSN: 0098-3500. DOI: `10.1145/3321515`. URL: `https://doi.org/10.1145/3321515`.

[75] D.C. Wilcox. *Turbulence Modeling for CFD*. Turbulence Modeling for CFD v. 1. DCW Industries, 2006. ISBN: 9781928729082.

[76] Ramis Örlü. "Experimental studies in jet flows and zero pressure-gradient turbulent boundary layers". PhD thesis. May 2009.

[77] ANSYS Inc. *Defining an Effective Temperature*. n.d. URL: `https://www.afs.enea.it/project/neptunius/docs/fluent/html/ug/node294.htm`.

[78] Siddharth Suhas Kulkarni et al. "Fluid-structure interaction based optimisation in tidal turbines: A perspective review". In: *Journal of Ocean Engineering and Science* 7.5 (2022), pp. 449–461. ISSN: 2468-0133. DOI: `https://doi.org/10.1016/j.joes.2021.09.017`. URL: `https://www.sciencedirect.com/science/article/pii/S2468013321001005`.

[79] Mehdi Chamanara et al. "Effects of the Duct Angle and Propeller Location on the Hydrodynamic Characteristics of the Ducted Propeller". In: *Ship science amp; technology* 11.22 (Mar. 2018), pp. 41–48. DOI: `10.25043/19098642.162`. URL: `https://shipjournal.co/index.php/sst/article/view/162`.

[80] Kianoosh Yousefi, Reza Saleh, and Peyman Zahedi. "Numerical study of blowing and suction slot geometry optimization on NACA 0012 airfoil". In: *Journal of Mechanical Science and Technology* (May 2014). DOI: `10.1007/s12206-014-0119-1`.

[81] Kewei Xu, Yan Ren, and Gecheng Zha. "Numerical Analysis of Energy Expenditure for Co-Flow Wall Jet Separation Control". In: *AIAA SCITECH 2022 Forum*. DOI: `10.2514/6.2022-1547`. eprint: `https://arc.aiaa.org/doi/pdf/10.2514/6.2022-1547`. URL: `https://arc.aiaa.org/doi/abs/10.2514/6.2022-1547`.

[82] Esmaeel Fatahian et al. "Comparative study of flow separation control using suction and blowing over an airfoil with/without flap". In: *Sadhana* 44 (Nov. 2019), p. 220. DOI: `10.1007/s12046-019-1205-y`.

[83] Amgad Salama. "Velocity Profile Representation for Fully Developed Turbulent Flows in Pipes: A Modified Power Law". In: *Fluids* 6.10 (2021). ISSN: 2311-5521. DOI: `10.3390/fluids6100369`. URL: `https://www.mdpi.com/2311-5521/6/10/369`.

[84] Lawrence J. De Chant. "The venerable 1/7th power law turbulent velocity profile: a classical nonlinear boundary value problem solution and its relationship to stochastic processes". In: *Applied Mathematics and Computation* 161.2 (2005), pp. 463–474. ISSN: 0096-3003. DOI: `https://doi.org/10.1016/j.amc.2003.12.109`. URL: `https://www.sciencedirect.com/science/article/pii/S0096300304000050`.

[85] Chunhua Sheng and Qiuying Zhao. "Active Flow Control for Ducted Fans and Fan-In-Wing Configurations". US11485486B2. United States Patent. Nov. 2022. URL: `https://patents.google.com/patent/US11485486B2/en`.

[86] M. Serdar Genç, Ünver Kaynak, and Hüseyin Yapici. “Performance of transition model for predicting low Re aerofoil flows without/with single and simultaneous blowing and suction”. In: *European Journal of Mechanics - B/Fluids* 30.2 (2011), pp. 218–235. ISSN: 0997-7546. DOI: `https://doi.org/10.1016/j.euromechflu.2010.11.001`. URL: `https://www.sciencedirect.com/science/article/pii/S099775461000110X`.

[87] Bram Meijerink. “Separation reduction on a ducted propeller inlet with passive tangential blowing: Numerical analysis of tangential blowing with a bleed port on a ducted propeller”. Thesis committee: Prof. dr. ir. L.L.M. Veldhuis (supervisor), Dr. ir. T. Sinnige (examiner), Prof. dr. M. Kotsonis (chair). MA thesis. Delft, The Netherlands: Delft University of Technology, Sept. 2025. URL: `http://repository.tudelft.nl/`.

[88] R. Lindken and S. Burgmann. “14 - Laser-optical methods for transport studies in low temperature fuel cells”. In: *Polymer Electrolyte Membrane and Direct Methanol Fuel Cell Technology*. Ed. by Christoph Hartnig and Christina Roth. Vol. 2. Woodhead Publishing Series in Energy. Woodhead Publishing, 2012, pp. 425–461. ISBN: 978-1-84569-774-7. DOI: `https://doi.org/10.1533/9780857095480.3.424`. URL: `https://www.sciencedirect.com/science/article/pii/B9781845697747500141`.

[89] Amin Etminan et al. “Flow visualization: state-of-the-art development of micro-particle image velocimetry”. In: *Measurement Science and Technology* 33.9 (June 2022), p. 092002. DOI: `10.1088/1361-6501/ac75b0`. URL: `https://dx.doi.org/10.1088/1361-6501/ac75b0`.

[90] Luís Mendes, Alexandre Bernardino, and Rui M.L. Ferreira. “piv-image-generator: An image generating software package for planar PIV and Optical Flow benchmarking”. In: *SoftwareX* 12 (2020), p. 100537. ISSN: 2352-7110. DOI: `https://doi.org/10.1016/j.softx.2020.100537`. URL: `https://www.sciencedirect.com/science/article/pii/S2352711020300339`.

[91] Meng He et al. “Flow Characteristics and Parameter Influence of the Under-Expansion Jet on Circulation Control Airfoil”. In: *Energies* 16.9 (2023). ISSN: 1996-1073. DOI: `10.3390/en16093818`. URL: `https://www.mdpi.com/1996-1073/16/9/3818`.

[92] Yasuhiro Kamotani and Isaac Greber. *Experiments on Confined Turbulent Jets in Cross Flow*. Contractor Report NASA CR-2392. Case Western Reserve University, Division of Fluid, Thermal and Aerospace Sciences. Cleveland, OH: National Aeronautics and Space Administration, 1974. URL: `https://ntrs.nasa.gov/api/citations/19740010813/downloads/19740010813.pdf`.

A

Used airfoil coordinates: X400 Flap

This appendix provides the smoothened coordinates of the X400 flap airfoil used in the numerical analysis of this project. The coordinates are obtained using Savitzky-Golay filter discussed in section 5.1. Additionally, provided is the pressure distribution plot for each of the inspected filter widths used in the airfoil smoothening study.

A.1. Airfoil coordinates: X400 Flap; smoothened w = 11, o = 3

X	Y
1.000000	0.002800
0.989000	0.007092
0.976100	0.012551
0.961100	0.019077
0.943800	0.026469
0.924600	0.034525
0.903700	0.042956
0.881600	0.051668
0.858500	0.060447
0.834500	0.069161
0.809700	0.077783
0.784300	0.086336
0.758300	0.094835
0.732000	0.103225
0.705700	0.111413
0.679700	0.119327
0.654200	0.126900
0.629500	0.134041
0.604900	0.140666
0.580500	0.146767
0.556500	0.152341
0.532600	0.157400
0.508800	0.161963
0.485100	0.166003
0.461700	0.169502
0.438400	0.172498
0.415400	0.174951
0.392900	0.176816
0.370900	0.178071
0.349400	0.178702
0.328400	0.178692
0.307800	0.178018
0.287700	0.176685
0.268100	0.174710
0.249000	0.172097
0.230400	0.168864
0.212500	0.164976
0.195300	0.160433
0.178600	0.155244
0.162400	0.149412
0.146700	0.142973
0.131600	0.135955
0.117100	0.128458
0.103400	0.120558
0.090400	0.112363
0.078400	0.104013
0.067300	0.095617
0.057300	0.087313
0.048300	0.079191
0.040200	0.071358
0.033100	0.063867
0.027000	0.056739
0.021600	0.049986
0.016900	0.043586
0.013000	0.037509
0.009600	0.031717
0.006800	0.026164
0.004500	0.020834
0.002800	0.015691
0.001600	0.010745
0.000800	0.005954
0.000400	0.001295
0.000500	-0.003260
0.000900	-0.007710
0.001800	-0.012071
0.003000	-0.016328
0.004600	-0.020454
0.006700	-0.024438
0.009200	-0.028137
0.012200	-0.031509
0.015600	-0.034534
0.019400	-0.037122
0.023700	-0.039236
0.028400	-0.040837
0.033500	-0.041900
0.039100	-0.042481
0.045300	-0.042614
0.052200	-0.042383
0.060000	-0.041758
0.068900	-0.040831
0.079200	-0.039587
0.091300	-0.037948
0.105500	-0.035883
0.122500	-0.033326
0.142400	-0.030272
0.165200	-0.026791
0.190400	-0.022944
0.217300	-0.018891
0.245000	-0.014766
0.272900	-0.010710
0.300900	-0.006816
0.328400	-0.003156
0.355400	0.000245
0.382000	0.003405
0.408400	0.006328
0.434800	0.009029
0.461500	0.011528
0.488400	0.013814
0.515400	0.015876
0.542600	0.017700
0.569500	0.019276
0.596300	0.020599
0.623000	0.021641
0.649600	0.022397
0.676300	0.022869
0.702800	0.023054
0.729200	0.022946
0.755500	0.022531
0.781500	0.021795
0.807100	0.020745
0.832200	0.019374
0.856600	0.017688
0.880100	0.015656
0.902400	0.013315
0.923300	0.010706
0.942400	0.007922
0.959500	0.005054
0.974600	0.002180
0.987900	-0.000624
1.000000	-0.003200
1.000000	0.002800

A.2. XFOIL Cp distribution smoothening study

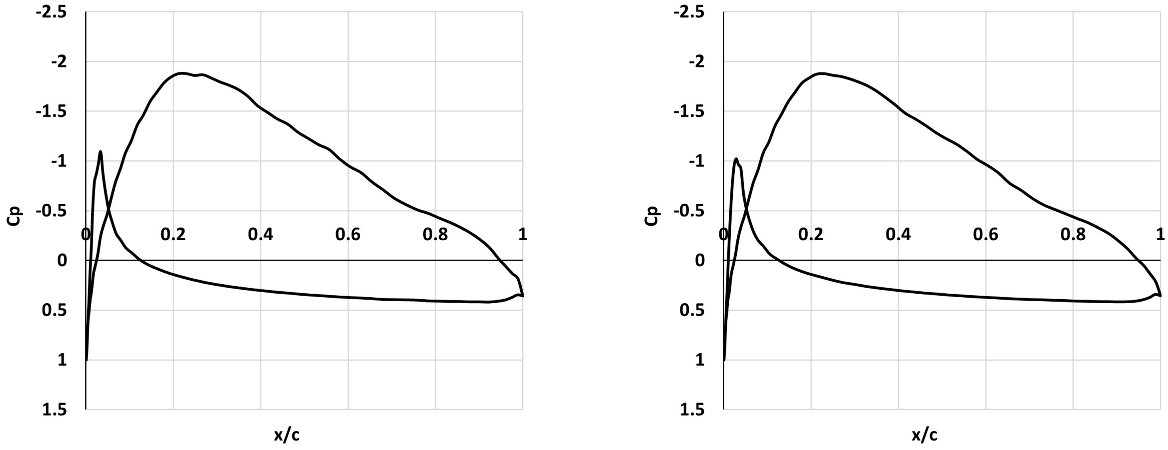

(a) w = 5, o =3 **(b)** w = 7, o =3

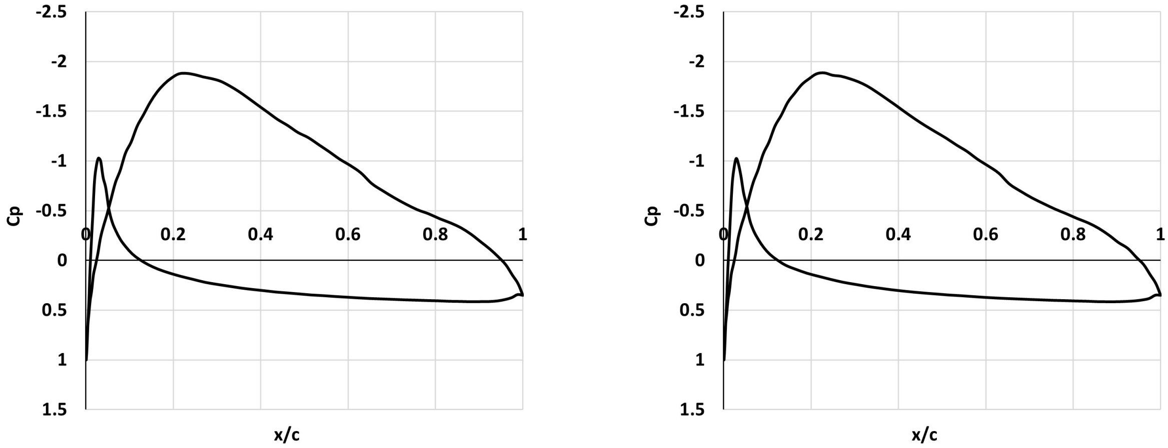

(c) w = 9, o =3 **(d)** w = 11, o =3

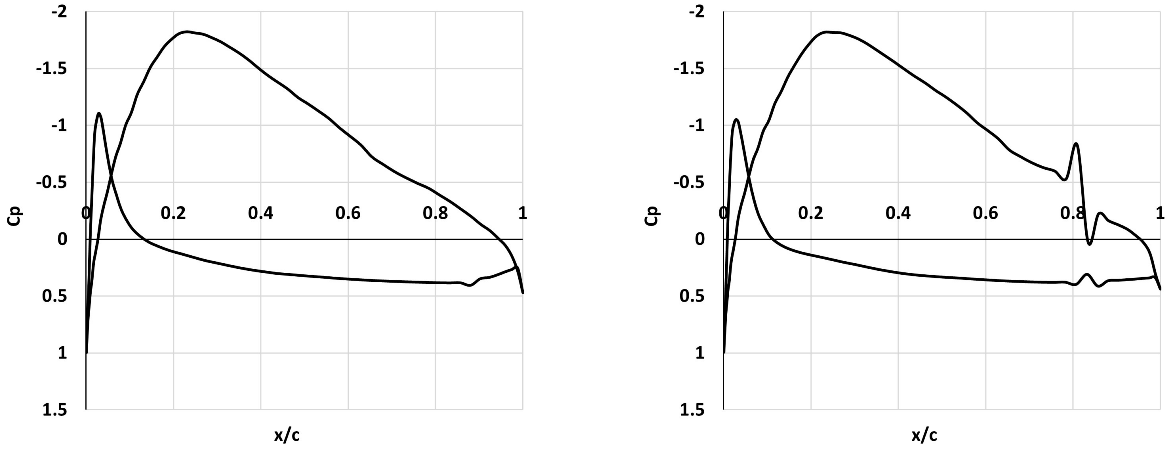

(e) w = 15, o =3 **(f)** w = 20, o =3

Figure A.1: Cp distribution comparison at different Savgol filter size

B

Appendix B: TUD-XPROP blade geometry

This appendix presents the chord and twist distributions of the TUD-XPROP propeller blade. The original distribution is shown in Table B.1, while the used distribution in this study is provided in Table B.2.

Table B.1: Original blade data with no pitch angle

r/R [-]	Chord [m]	Twist [°]
0.160	0.0325741	26.82
0.196	0.0321000	24.83
0.230	0.0316261	22.89
0.265	0.0311506	20.99
0.300	0.0306776	19.15
0.335	0.0302311	17.38
0.370	0.0298529	15.62
0.405	0.0295839	13.87
0.440	0.0294857	12.14
0.475	0.0295811	10.43
0.510	0.0298379	8.73
0.545	0.0301760	7.05
0.580	0.0305150	5.39
0.615	0.0307752	3.75
0.650	0.0309372	2.12
0.685	0.0310523	0.60
0.700	0.0311009	0.03
0.720	0.0311658	-0.73
0.755	0.0311599	-1.87
0.790	0.0307789	-2.91
0.825	0.0297761	-3.90
0.860	0.0280360	-4.80
0.895	0.0255175	-5.67
0.930	0.0222309	-6.53
0.965	0.0185338	-7.37
1.000	0.0138289	-8.00

Table B.2: Simplified blade data by JavaProp with applied 45 degrees pitch at 70% of the blade span

r/R [-]	c/R [-]	Twist [°]
0	Spinner	-
0.05	Spinner	-
0.1	Spinner	-
0.15	Spinner	-
0.2	Spinner	-
0.25	0.1543	66.8
0.3	0.151	64.2
0.35	0.148	61.6
0.4	0.1458	59.1
0.45	0.1452	56.7
0.5	0.1465	54.2
0.55	0.1487	51.8
0.6	0.1509	49.5
0.65	0.1522	47.1
0.7	0.1531	45
0.75	0.1534	43.3
0.8	0.1501	41.8
0.85	0.1404	40.5
0.9	0.1233	39.2
0.95	0.099	38
1	0.0681	37

C

CFD analysis: Additional material

This appendix provides additional data from the performed numerical analysis. The following sections present the velocity contours for the cases where the propeller is active and inactive, along with the coefficient of friction plots used to estimate the separation point location on the suction side of the wing.

C.1. Domain view: Velocity magnitude contours

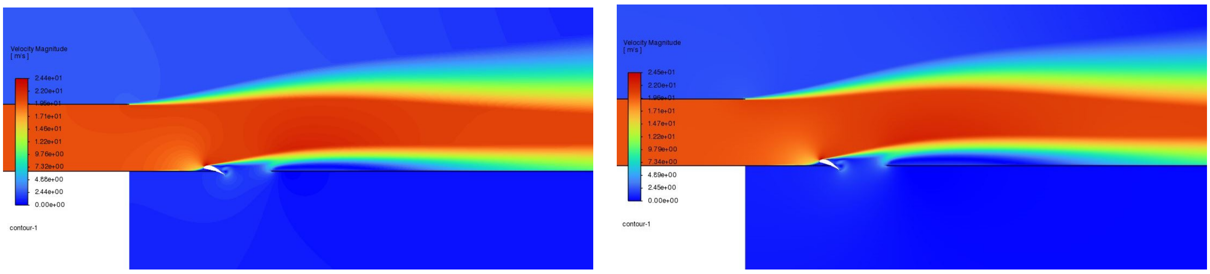

(a) 20 deg

(b) 25 deg

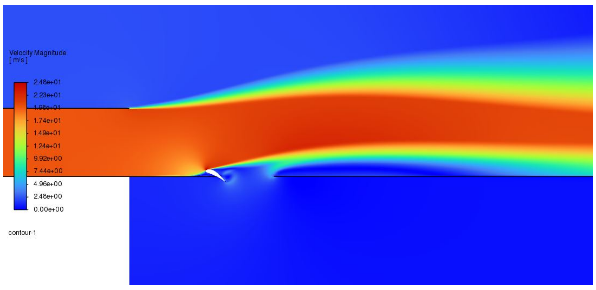

(c) 30 deg

Figure C.1: SST $k - \omega$: Velocity magnitude at different angles of attack with no upstream bleed, v_∞ = 20 m/s, propeller off

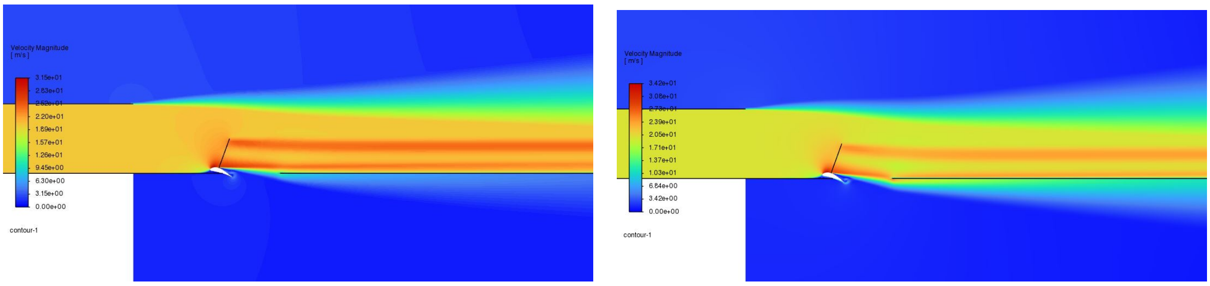

(a) No upstream bleed

(b) 25 mm

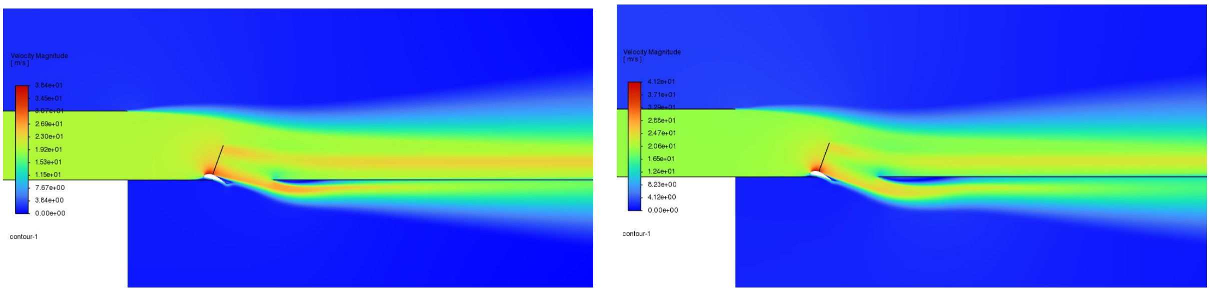

(c) 50 mm

(d) 75 mm

Figure C.2: SST $k - \omega$: Velocity contour of domain at AoA = 20 degrees and different upstream bleed sizes, v_∞ = 20 m/s, propeller on

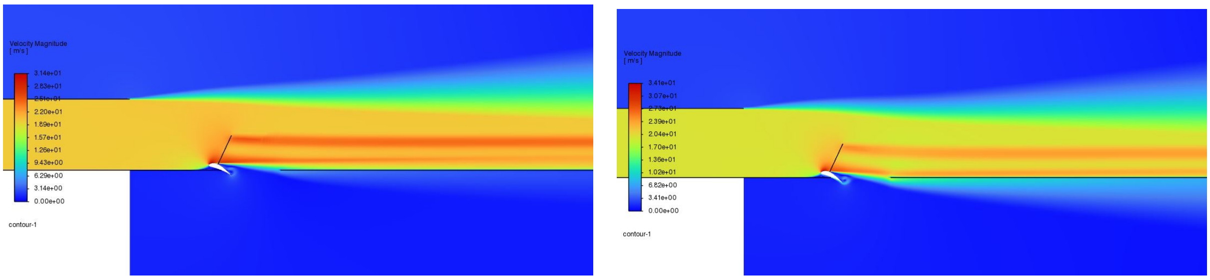

(a) No upstream bleed

(b) 25 mm

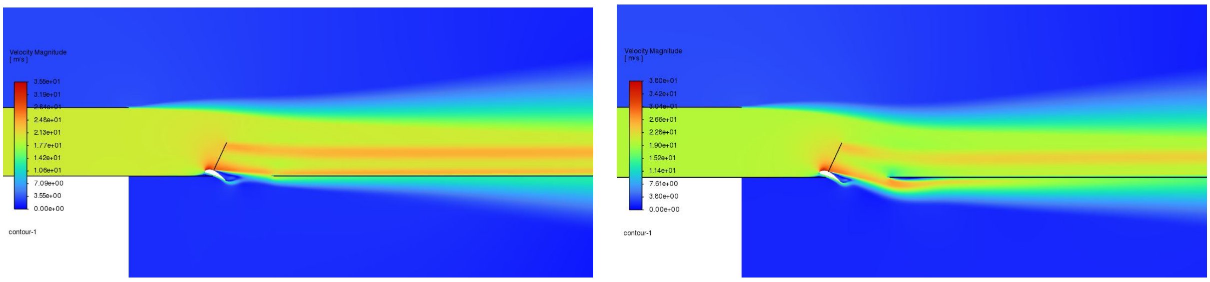

(c) 50 mm

(d) 75 mm

Figure C.3: SST $k - \omega$: Velocity contour of domain at AoA = 25 degrees and different upstream bleed sizes, v_∞ = 20 m/s, propeller on

C.2. Zoom-In view: Velocity magnitude contours

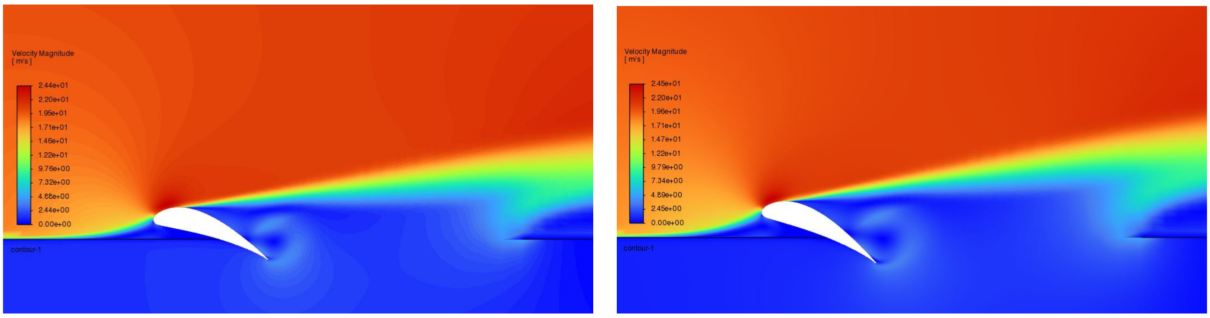

(a) 20 deg **(b)** 25 deg

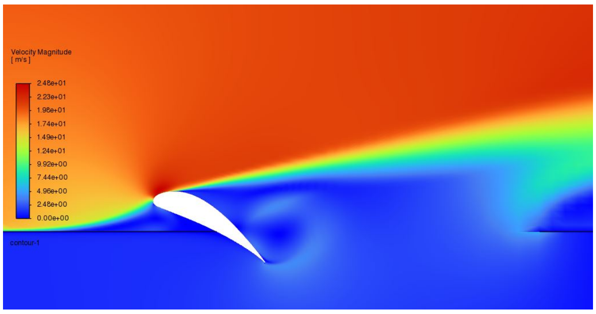

(c) 30 deg

Figure C.4: SST $k-\omega$: Velocity magnitude at different angles of attack with no upstream bleed, v_∞ = 20 m/s, propeller off

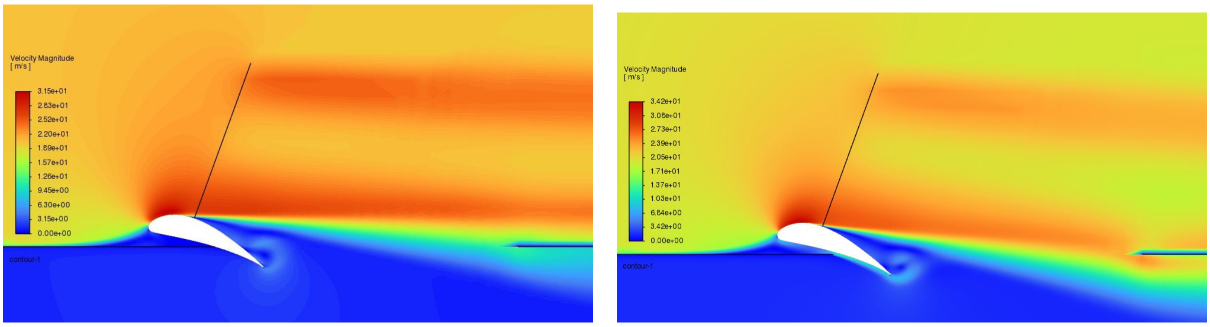

(a) No upstream bleed **(b)** 25 mm

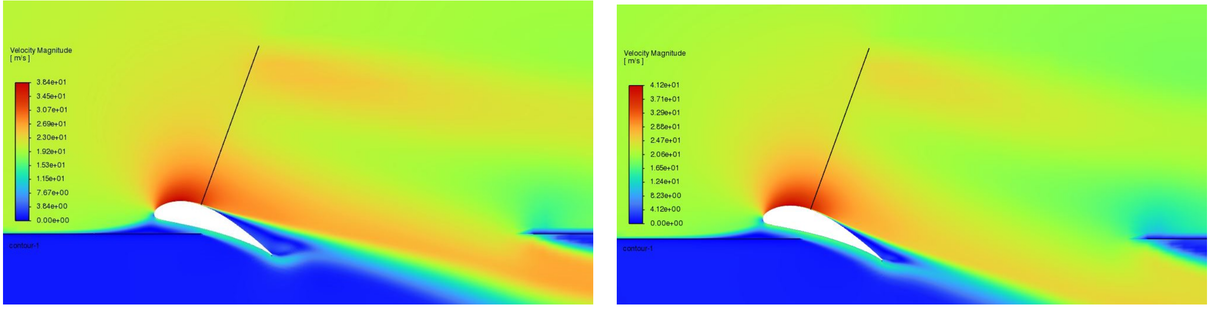

(c) 50 mm **(d)** 75 mm

Figure C.5: SST $k-\omega$: Velocity magnitude at AoA = 20 degrees and different upstream bleed sizes, v_∞ = 20 m/s, propeller on

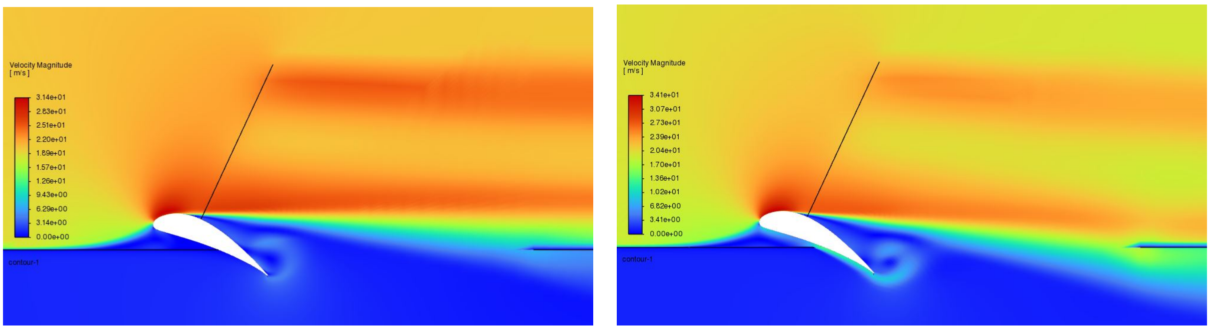

(a) No upstream bleed

(b) 25 mm

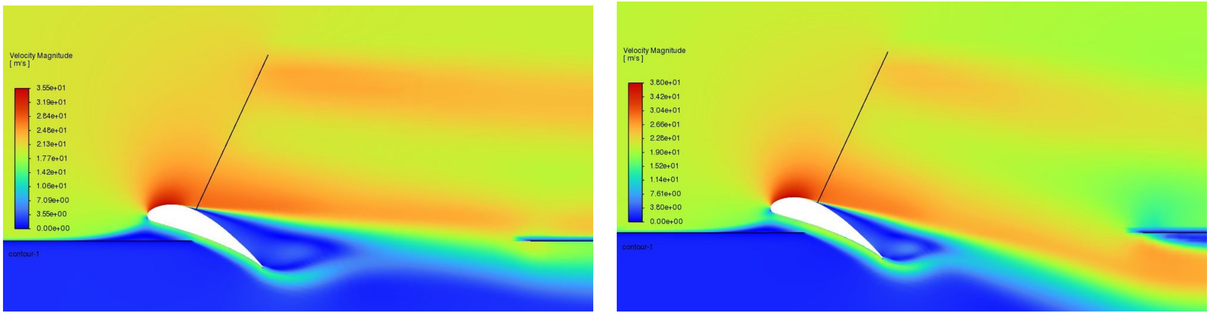

(c) 50 mm

(d) 75 mm

Figure C.6: SST $k-\omega$: Velocity contour at AoA = 25 degrees and different upstream bleed sizes, v_∞ = 20 m/s, propeller on

C.3. Coefficient of friction comparison for different upstream bleed sizes

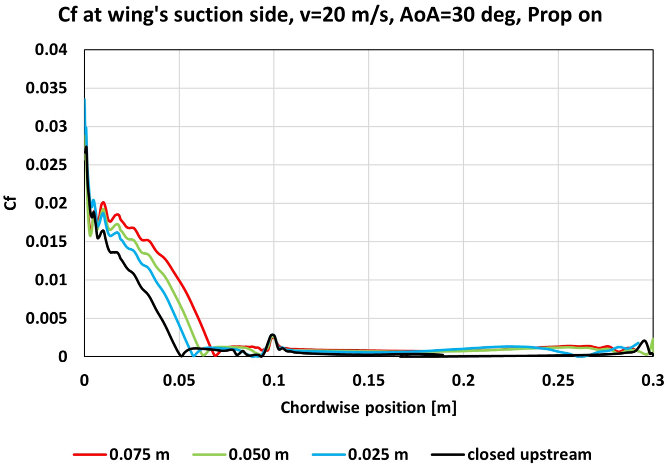

(a) AoA=30 degrees

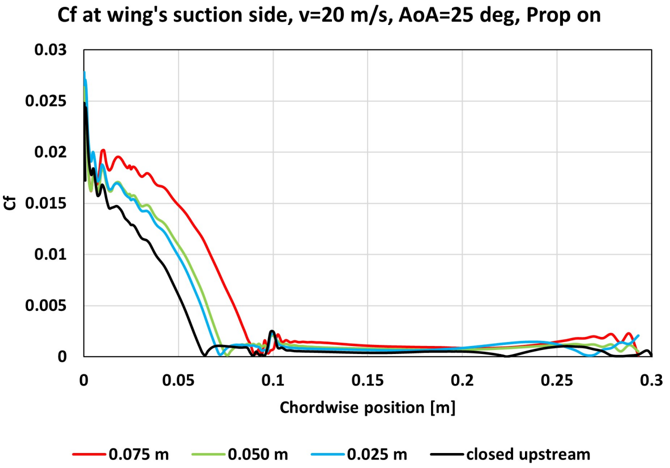

(b) AoA=25 degrees

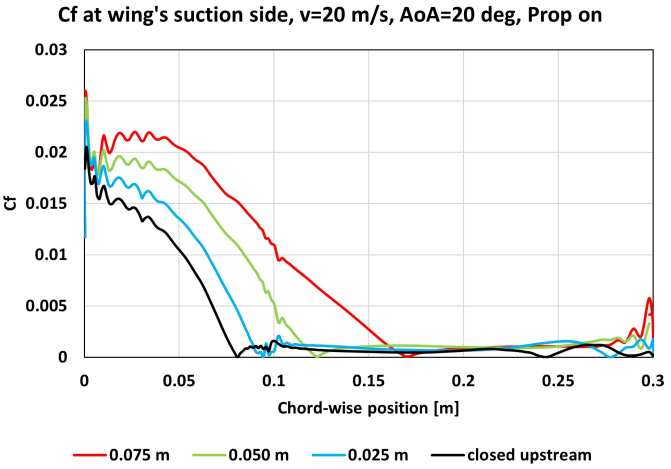

(c) AoA=20 degrees

Figure C.7: SST $k-\omega$: Coefficient of friction comparison at the suction side of the wing, v_∞ = 20 m/s, propeller on

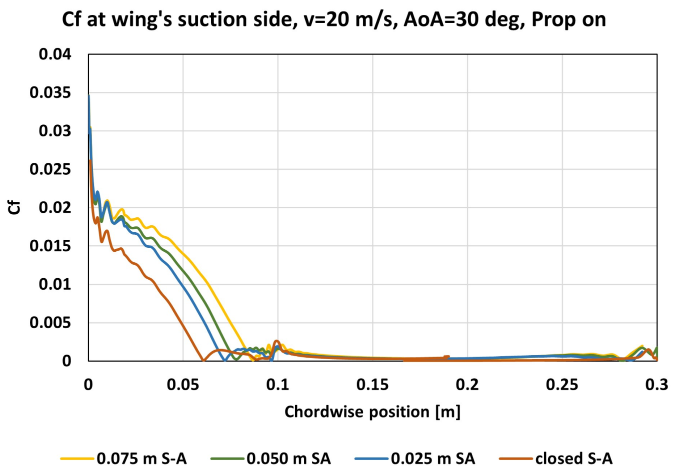

(a) AoA=30 degrees

(b) AoA=25 degrees

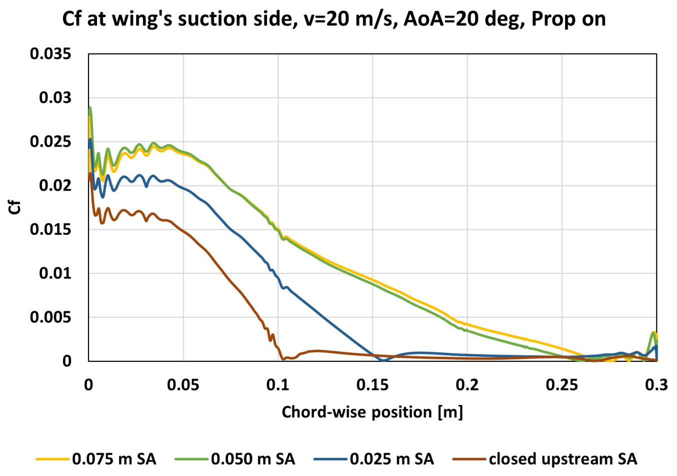

(c) AoA=20 degrees

Figure C.8: Spalart–Allmaras: Coefficient of friction comparison at the suction side of the wing, v_∞ = 20 m/s, propeller on

D

PIV: Additional results

This appendix provides additional data from the performed PIV analysis at freestream velocity of 10 m/s. The evaluated velocity profiles just upstream the propeller blade are shown in section D.1, while the resulting velocity fields in the selected region of interest can be found in section D.2.

D.1. Velocity profiles at just upstream the propeller blade at v_∞ = 10 m/s

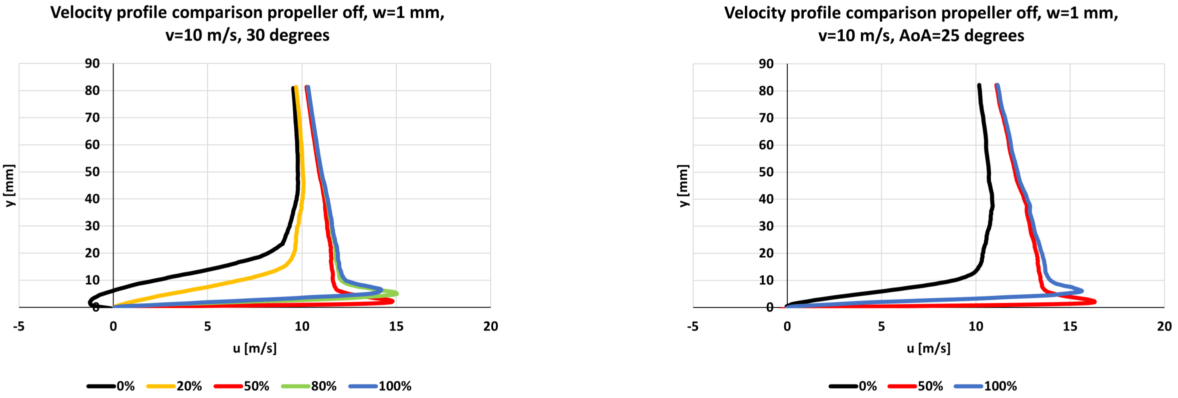

(a) AoA = 30 degrees

(b) AoA = 25 degrees

Figure D.1: PIV data: Velocity profile comparison just upstream the propeller blade location, v_∞ = 10 m/s, propeller off

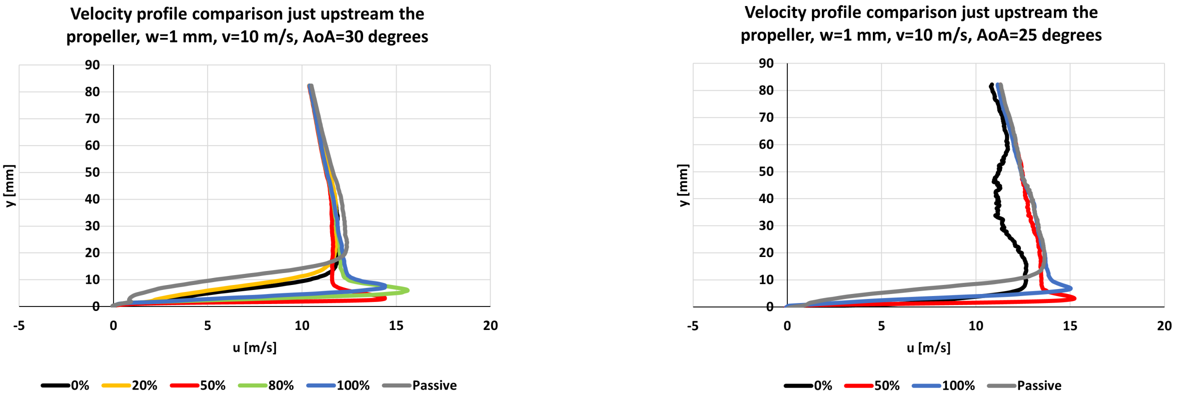

(a) AoA = 30 degrees

(b) AoA = 25 degrees

Figure D.2: PIV data: Velocity profile comparison just upstream the propeller blade location, v_∞ = 10 m/s, propeller on

D.2. Velocity fields: Propeller off at v_∞ = 10 m/s

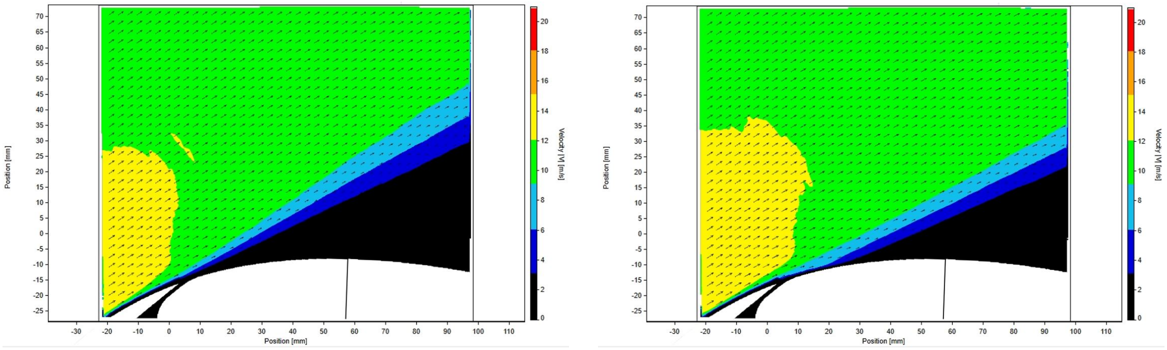

(a) 0% **(b)** 20% ($C_\mu = 0.69\%$)

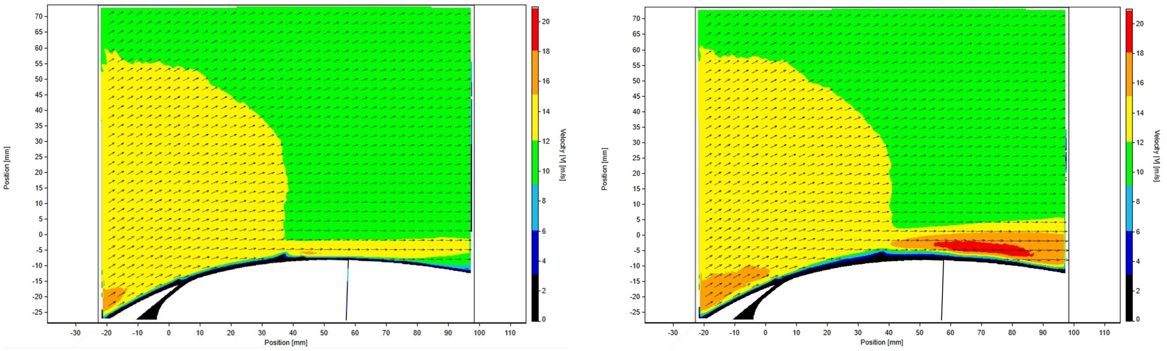

(c) 50% ($C_\mu = 4.29\%$) **(d)** 80% ($C_\mu = 10.99\%$)

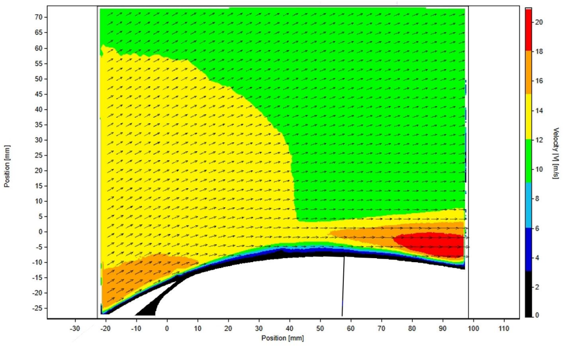

(e) 100% ($C_\mu = 17.17\%$)

Figure D.3: PIV data: Average velocity field for the tested blowing coefficients at AoA = 30 degrees, v_∞ = 10 m/s, propeller off

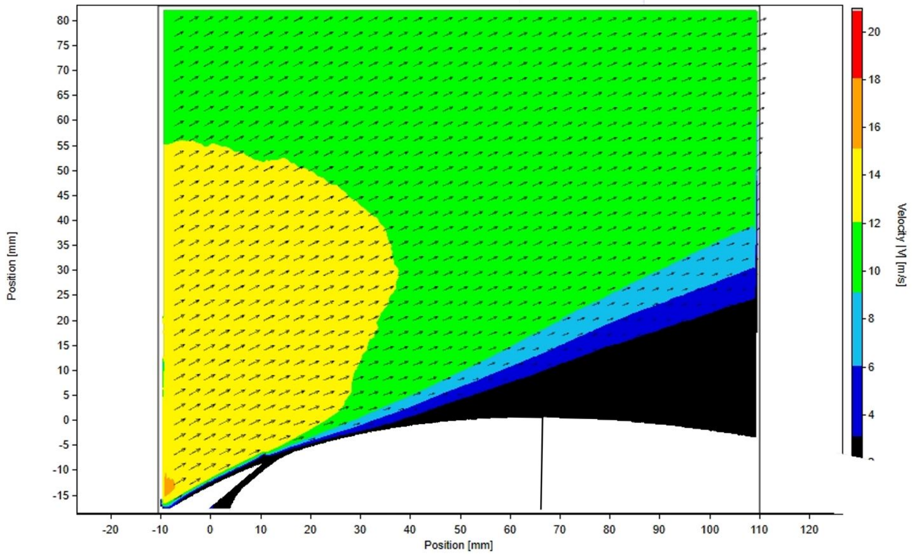

(a) 0%

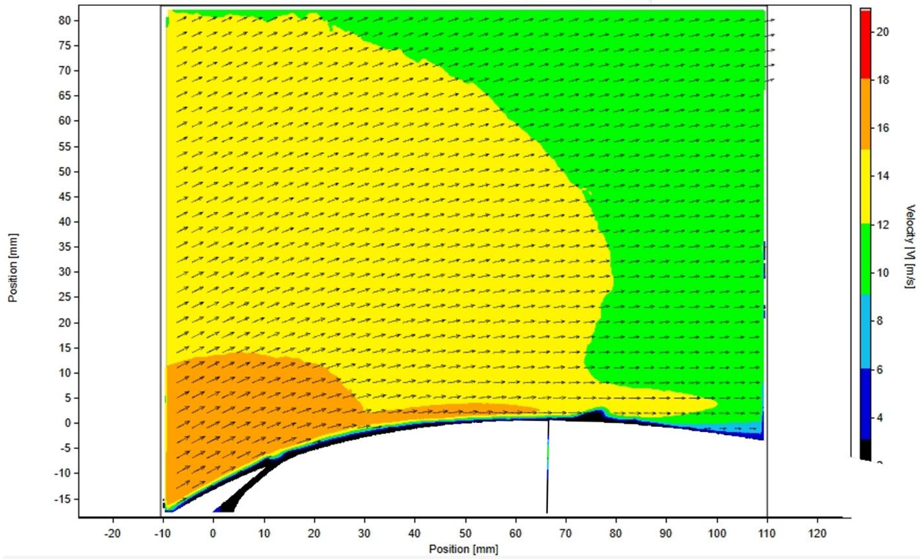

(b) 50% ($C_\mu = 4.29\%$)

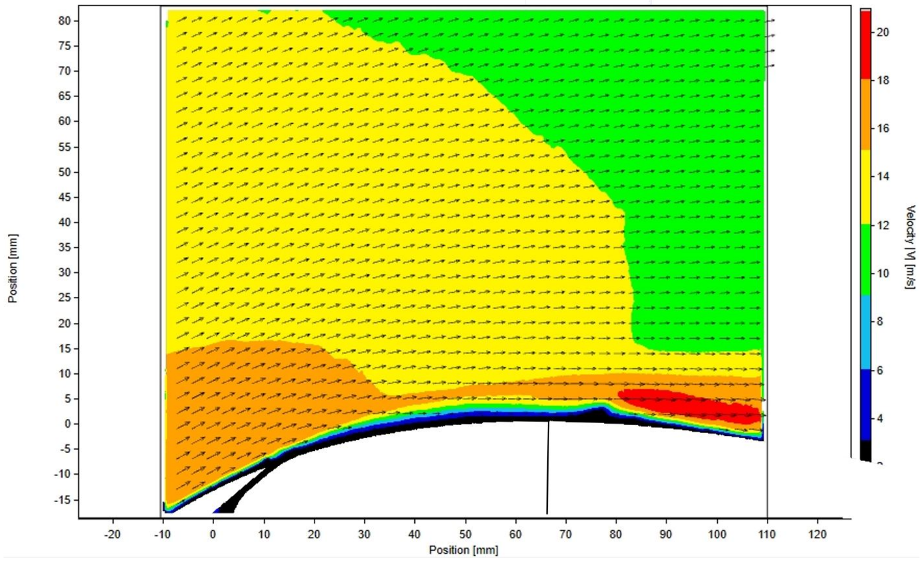

(c) 100% ($C_\mu = 17.17\%$)

Figure D.4: PIV data: Average velocity field for the tested blowing coefficients at AoA = 25 degrees, v_∞ = 10 m/s, propeller off

D.3. Velocity fields: Propeller on at v_∞ = 10 m/s

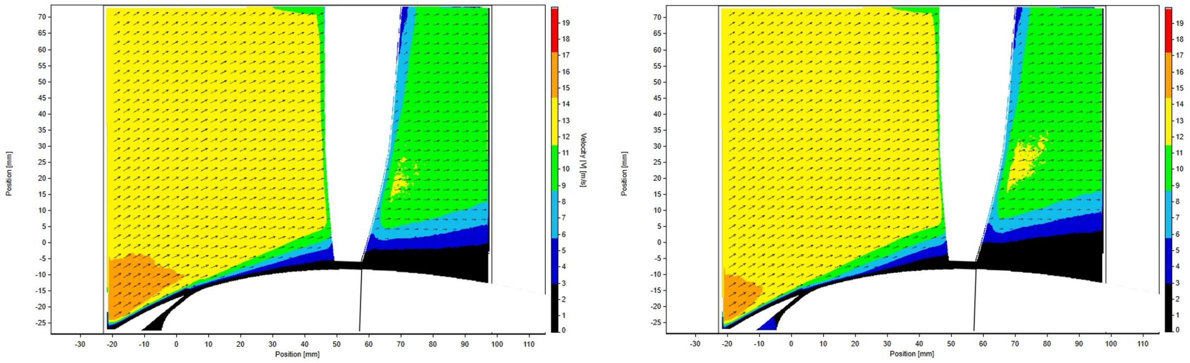

(a) 0% **(b)** 20% ($C_\mu = 0.69\%$)

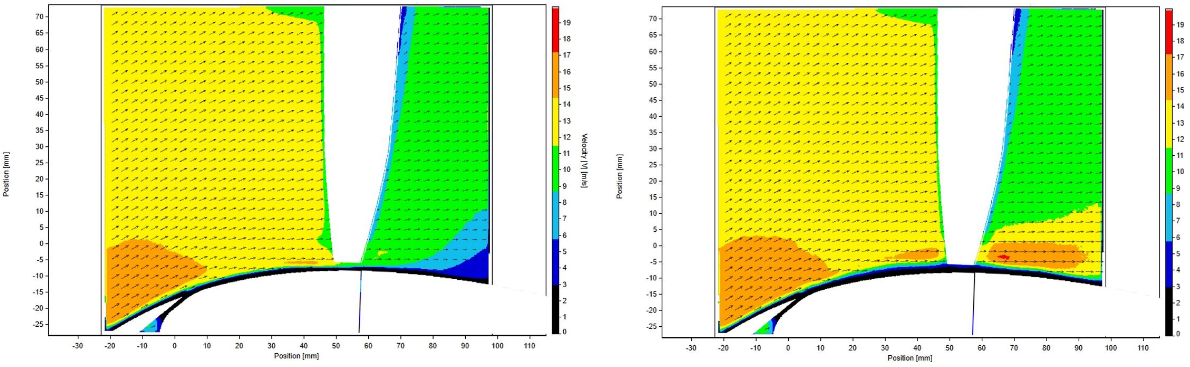

(c) 50% ($C_\mu = 4.29\%$) **(d)** 80% ($C_\mu = 10.99\%$)

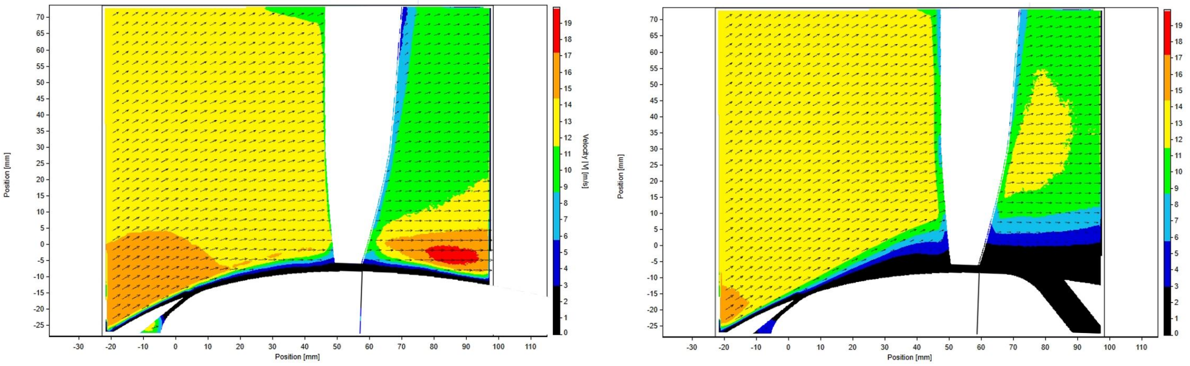

(e) 100% ($C_\mu = 17.17\%$) **(f)** Passive flow control

Figure D.5: PIV data: Average velocity field for the tested blowing coefficients at AoA = 30 degrees, v_∞ = 10 m/s, propeller on

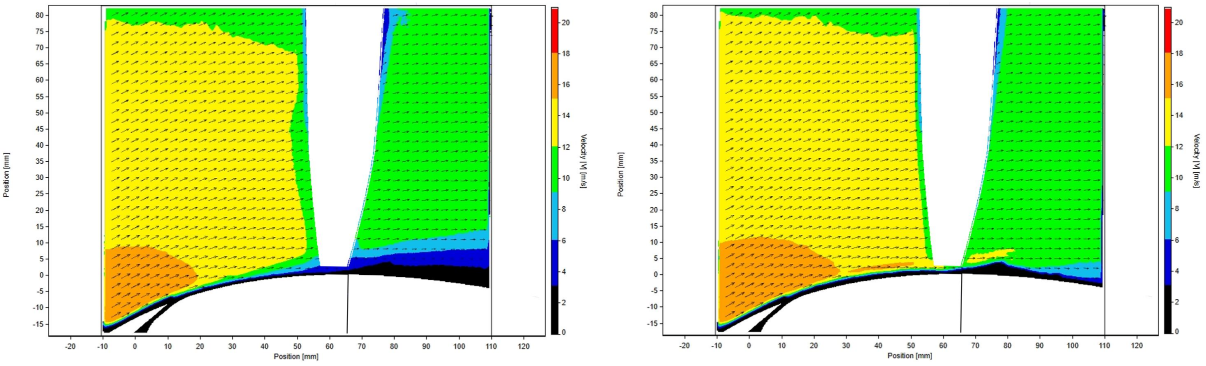

(a) 0% **(b)** 50% ($C_\mu = 4.29\%$)

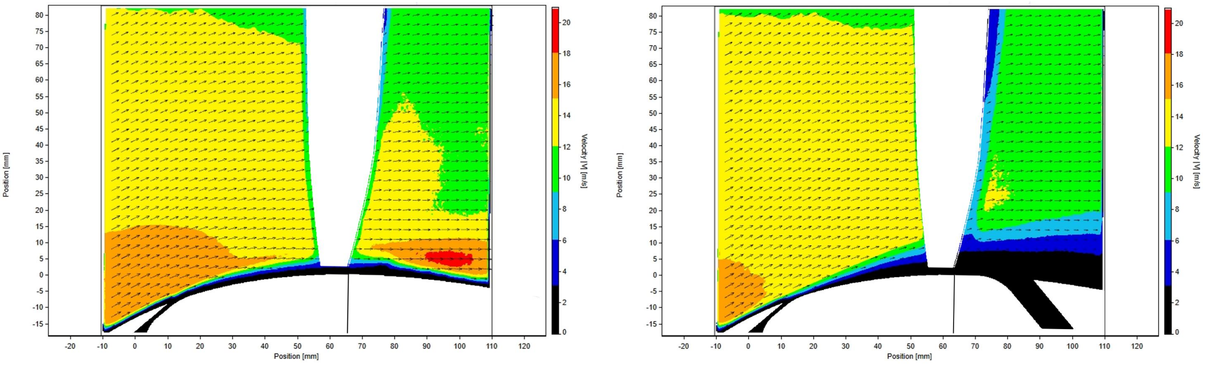

(c) 100% ($C_\mu = 17.17\%$) **(d)** Passive flow control

Figure D.6: PIV data: Average velocity field for the tested blowing coefficients at AoA = 25 degrees, v_∞ = 10 m/s, propeller on

E

Mass-flow estimation code

This appendix provides the used code for calculating the mass-flow through each of the six channels in the designed blowing connector, discussed in subsection 6.1.3. The code is written in Python language. The calculation is based on quarter-circle approach. The required total number of vanes is five in order to split the total mass-flow coming from the air supply tube in six channels. This results in only three vanes to be present in the quarter-circle domain due to symmetry. The code considers the central vane location as fixed, while the radial position of the remaining two vane positions can be varied. The code is as follows:

```python
import numpy as np
from scipy.integrate import quad

def quarter_circle(x, R):
    return np.sqrt(R**2 - x**2)

def compute_mass_flows(rho, x1, x2, R, thickness):
    half_thick = thickness / 2

    if not (0.5 < x1-half_thick < x1 + half_thick < x2 - half_thick < x2 + half_thick < R):
        raise ValueError("Check that the vanes do not overlap and all fit inside the quarter circle domain.")

    # areas
    area1, _ = quad(quarter_circle, 0.5, x1-half_thick, args=(R,))
    area2, _ = quad(quarter_circle, x1+half_thick, x2-half_thick, args=(R,))
    area3, _ = quad(quarter_circle, x2+half_thick, R, args=(R,))
    total = area1 + area2 + area3
    full  = np.pi * R**2 / 4

    # mass-flows
    mf1 = rho * area1 * 1e-6 * 10
    mf2 = rho * area2 * 1e-6 * 9.68
    mf3 = rho * area3 * 1e-6 * 8

    # prints
    print(f"Area 1: Area between central and middle vane: {area1:.3f} mm²")
    print(f"Area 2: Area between middle and farthest vane: {area2:.3f} mm²")
    print(f"Area 3: Area between farthest vane and tube radius: {area3:.3f} mm²")
    print(f"\nTotal flow area: {total:.3f} mm²")
    print(f"Expected full quarter circle area: {full:.3f} mm²")
    print(f"Flow area loss due to vertical vanes: {full-total:.3f} mm²")
    print(f"\nMass-flow Area 1 (10 m/s): {mf1:.6f} kg/s")
    print(f"Mass-flow Area 2 (9.68 m/s): {mf2:.6f} kg/s")
    print(f"Mass-flow Area 3 (8 m/s): {mf3:.6f} kg/s")

# Input variables
rho = 1.225     # density (kg/m³)
R = 8           # radius in mm
thickness = 1.0  # vane thickness (mm)
x1 = 2.235      # intermediate vane center (mm)
x2 = 4.635      # farthest vane center (mm)


compute_mass_flows(rho, x1, x2, R, thickness)
```

F

Technical drawings

This appendix provides 2D technical drawings about the used parts in the experimental setup. Included are the drawings of the used propeller, 3D-printed parts, and the machining details of the used existing wing model.

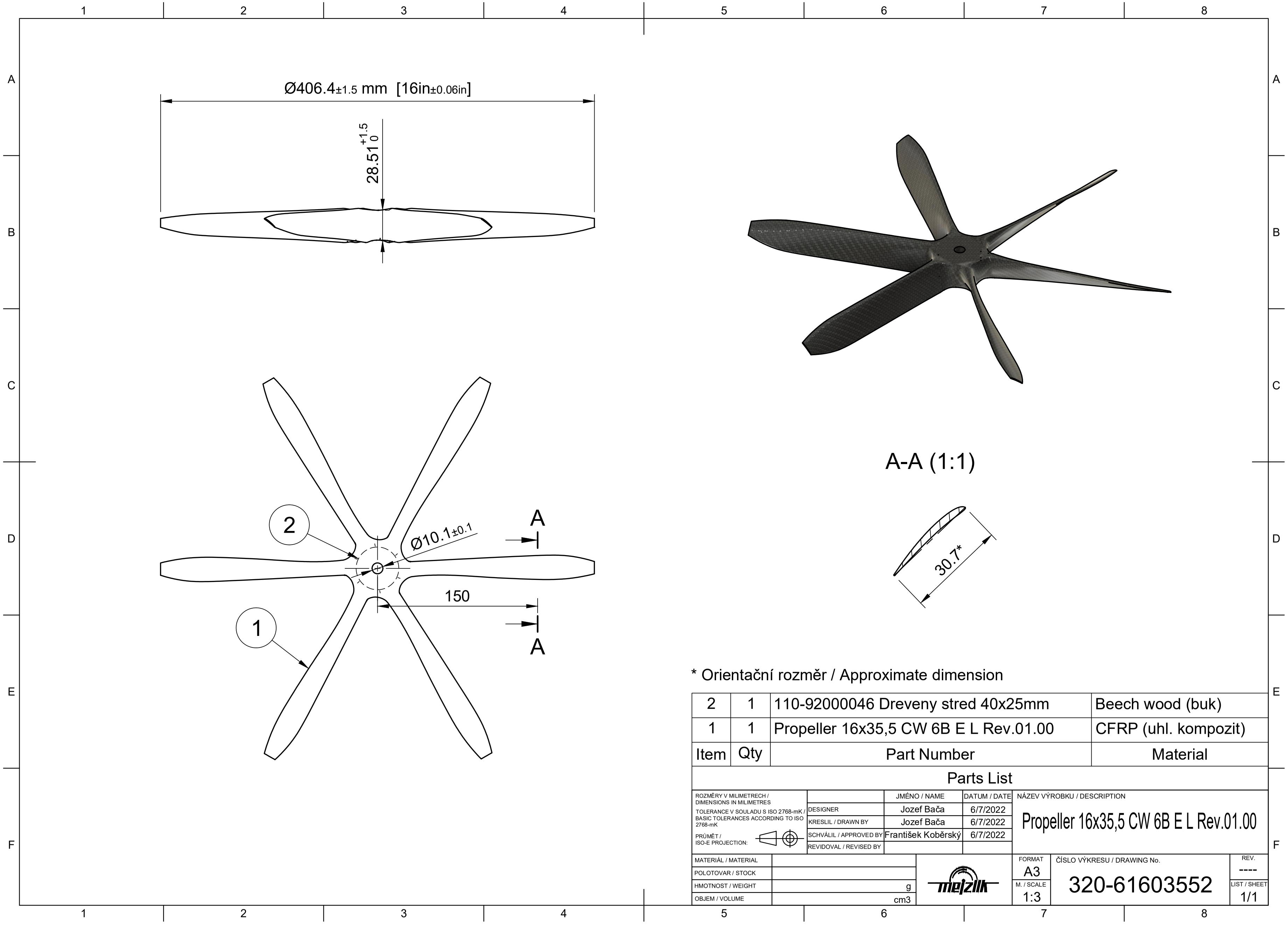

* Orientační rozměr / Approximate dimension

2	1	110-92000046 Dreveny stred 40x25mm	Beech wood (buk)
1	1	Propeller 16x35,5 CW 6B E L Rev.01.00	CFRP (uhl. kompozit)
Item	Qty	Part Number	Material

Parts List

Figure F.1: Technical drawing: TUD-XPROP

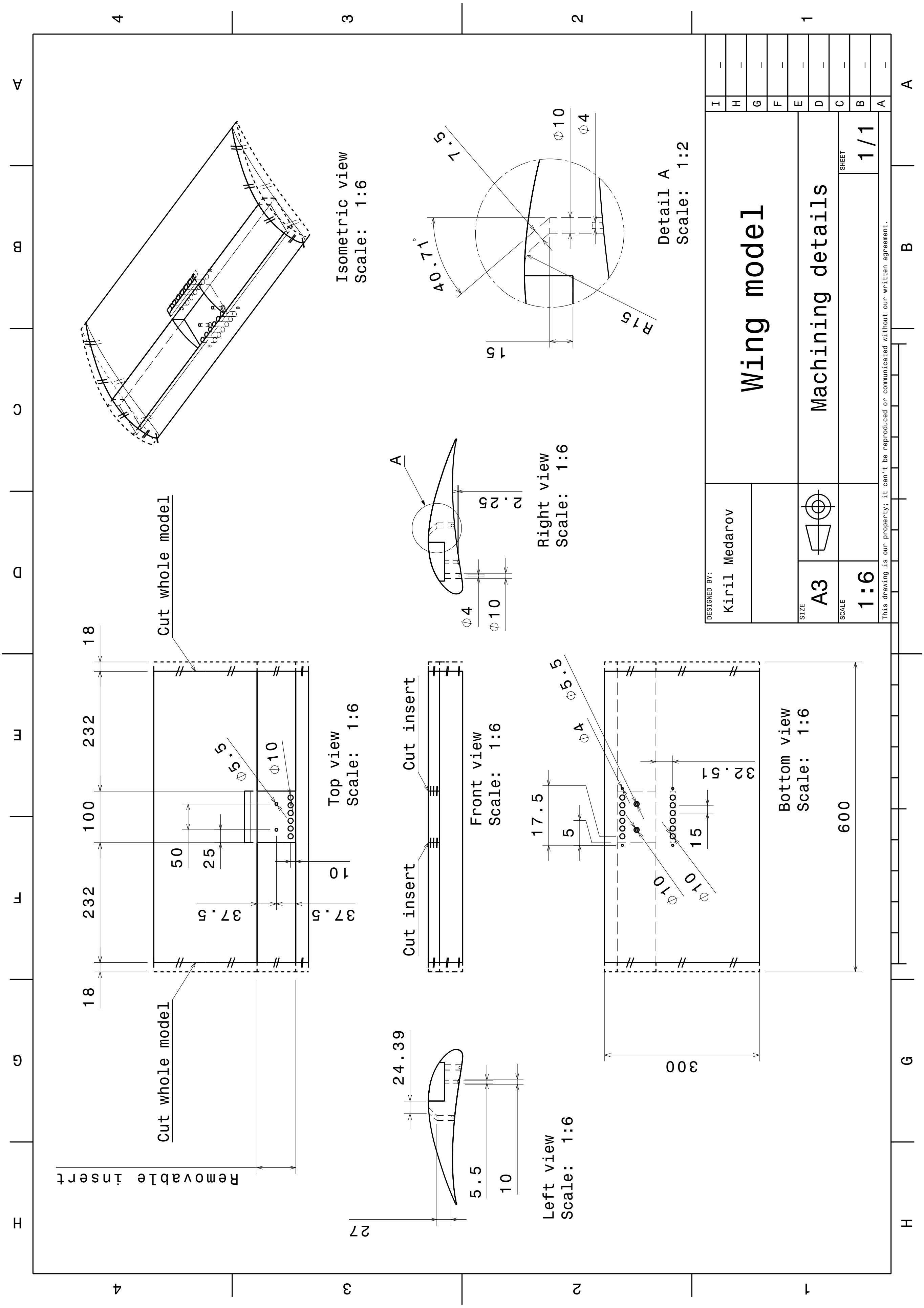

Figure F.2: Machining details of the existing wing model

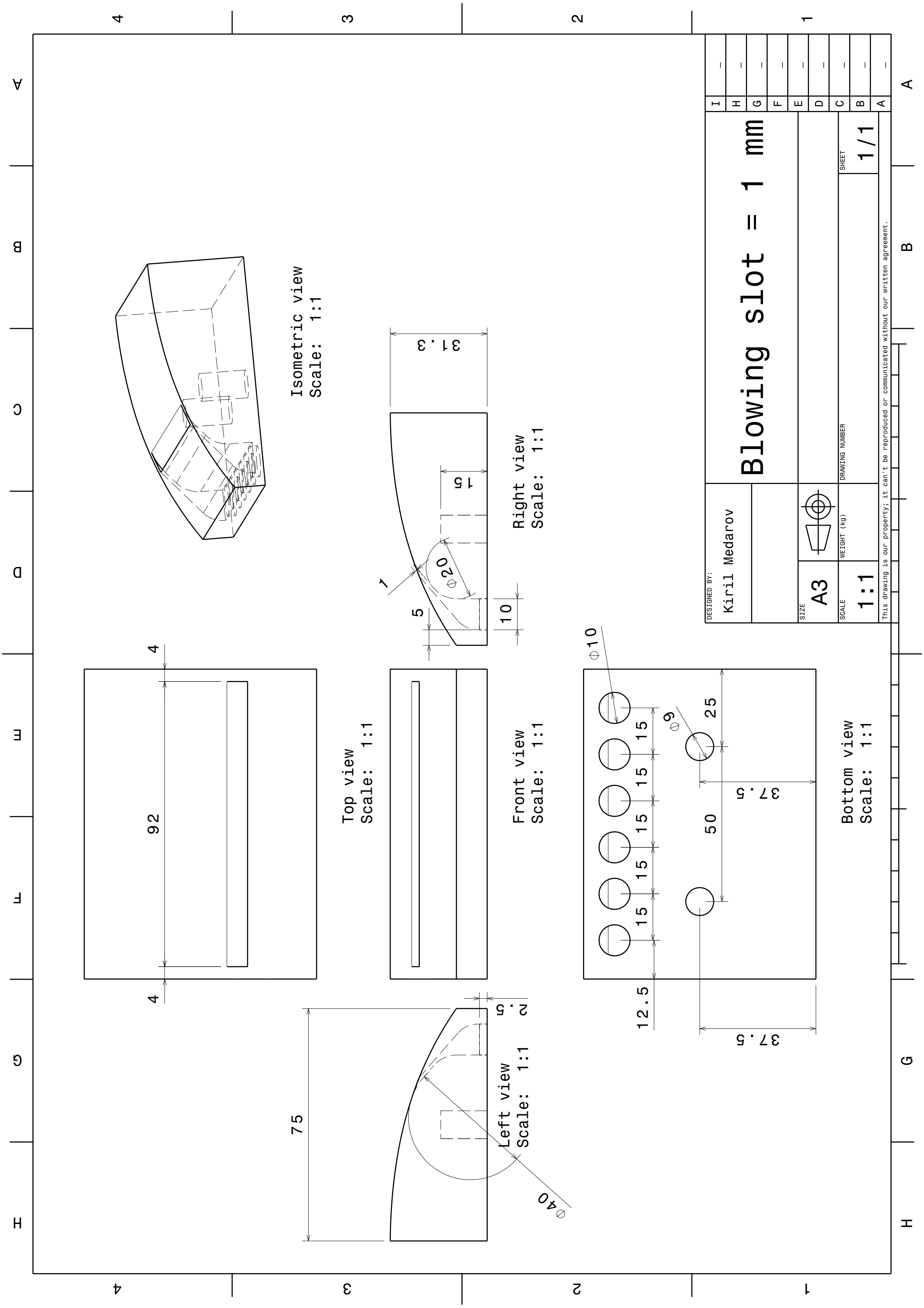

Figure F.3: Technical drawing: Blowing slot width = 1 mm

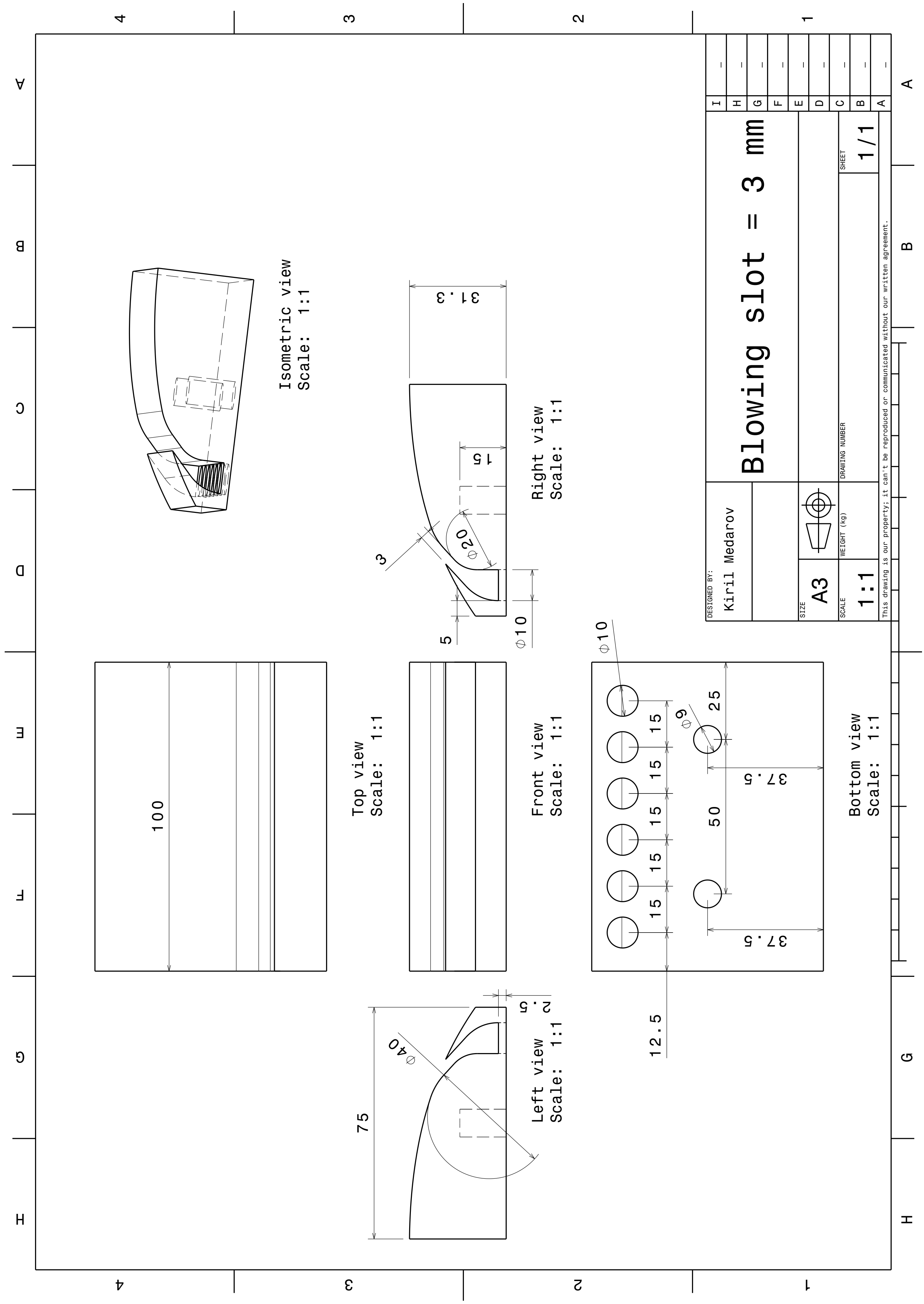

Figure F.4: Technical drawing: Blowing slot width = 3 mm

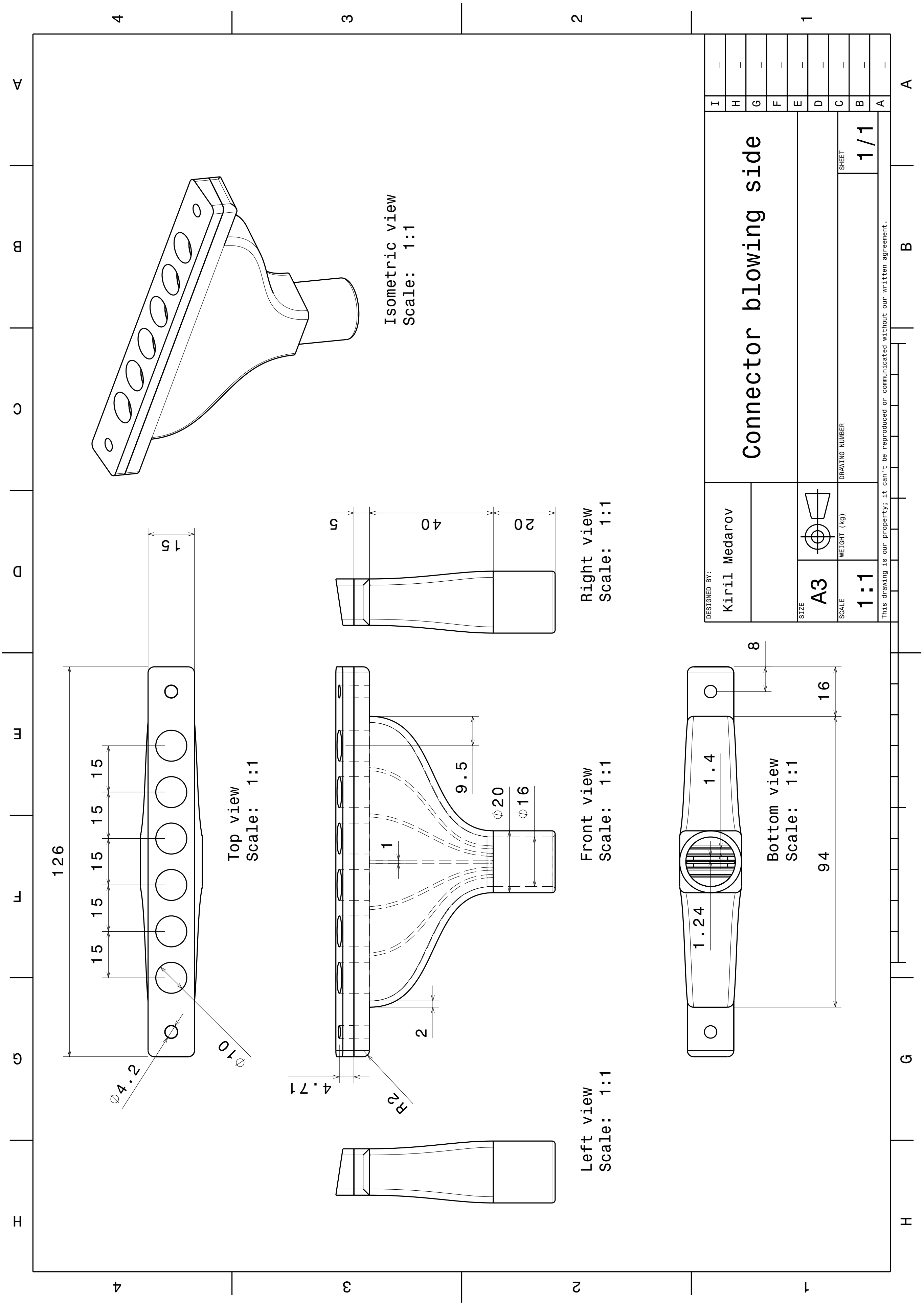

Figure F.5: Technical drawing: Connector blowing side

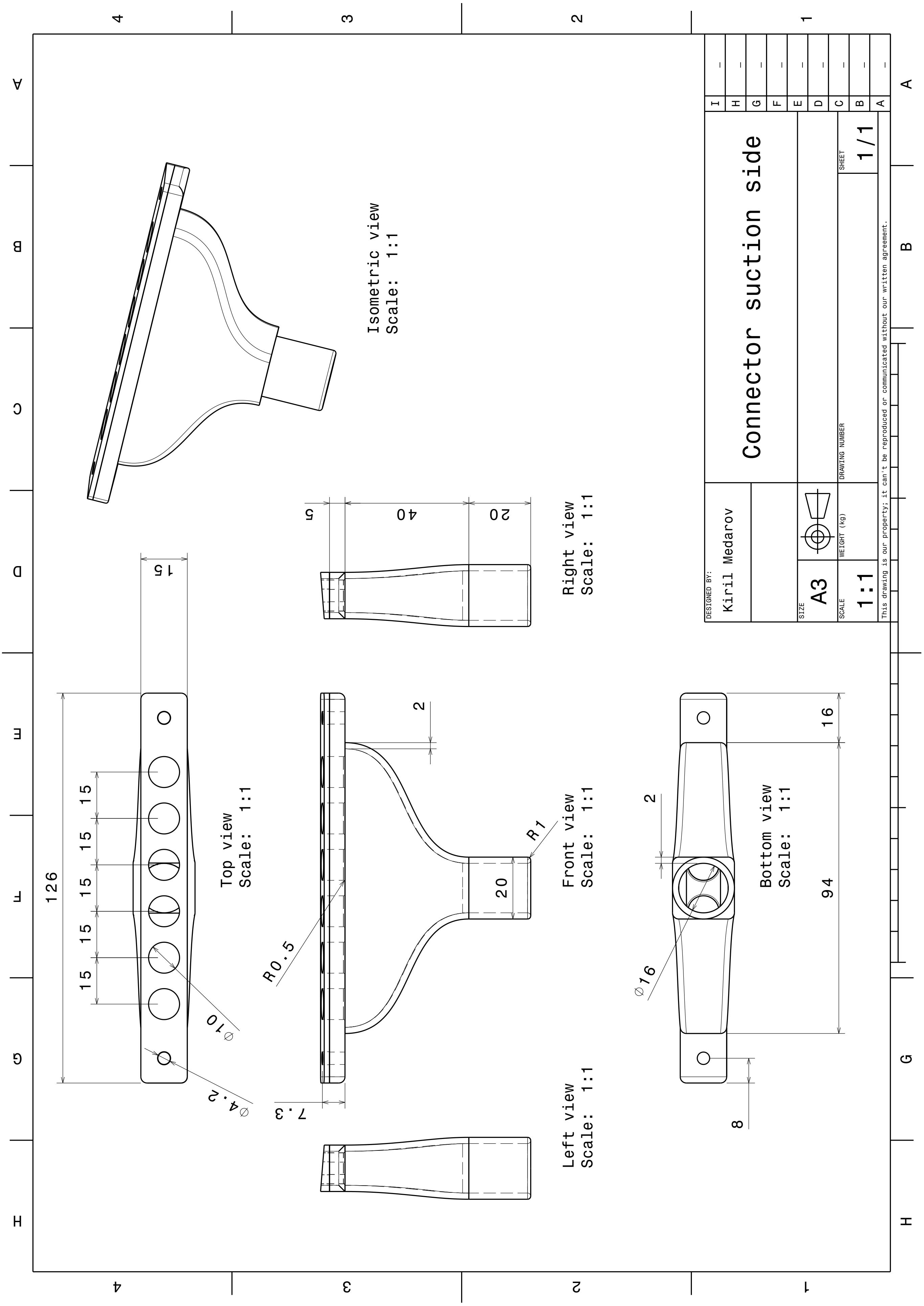

Figure F.6: Technical drawing: Connector suction side

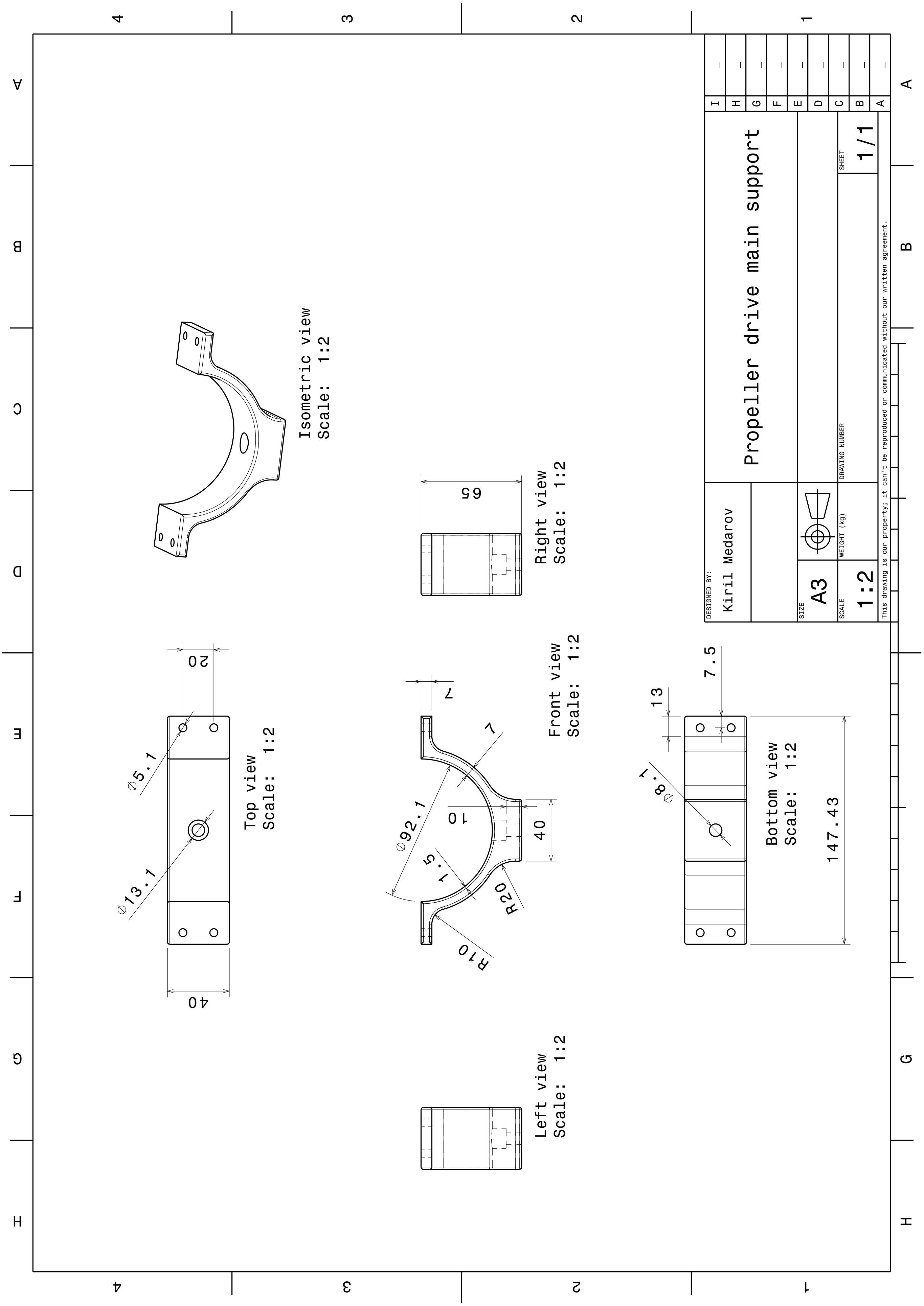

Figure F.7: Technical drawing: Propeller drive main support

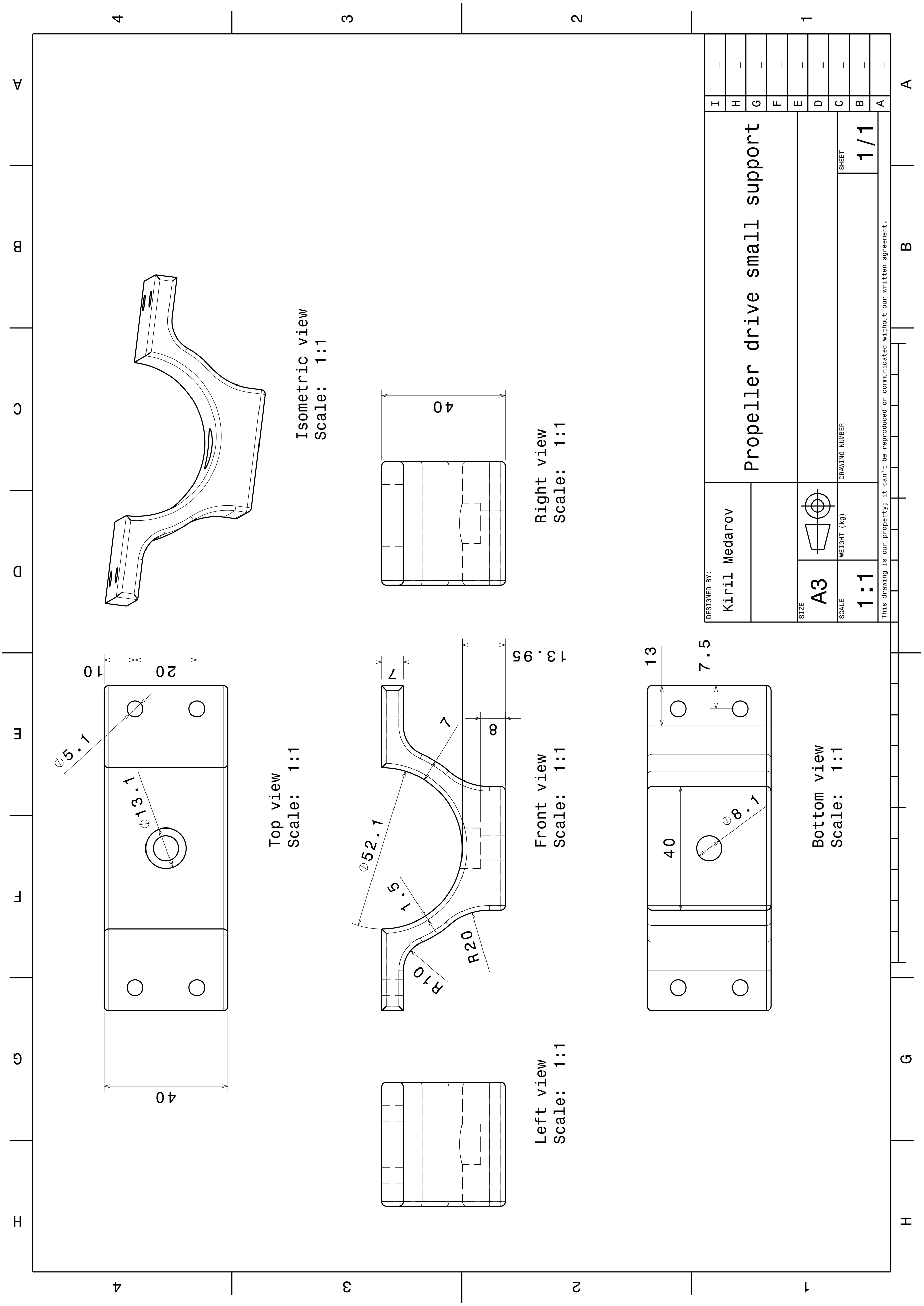

Figure F.8: Technical drawing: Propeller drive small support

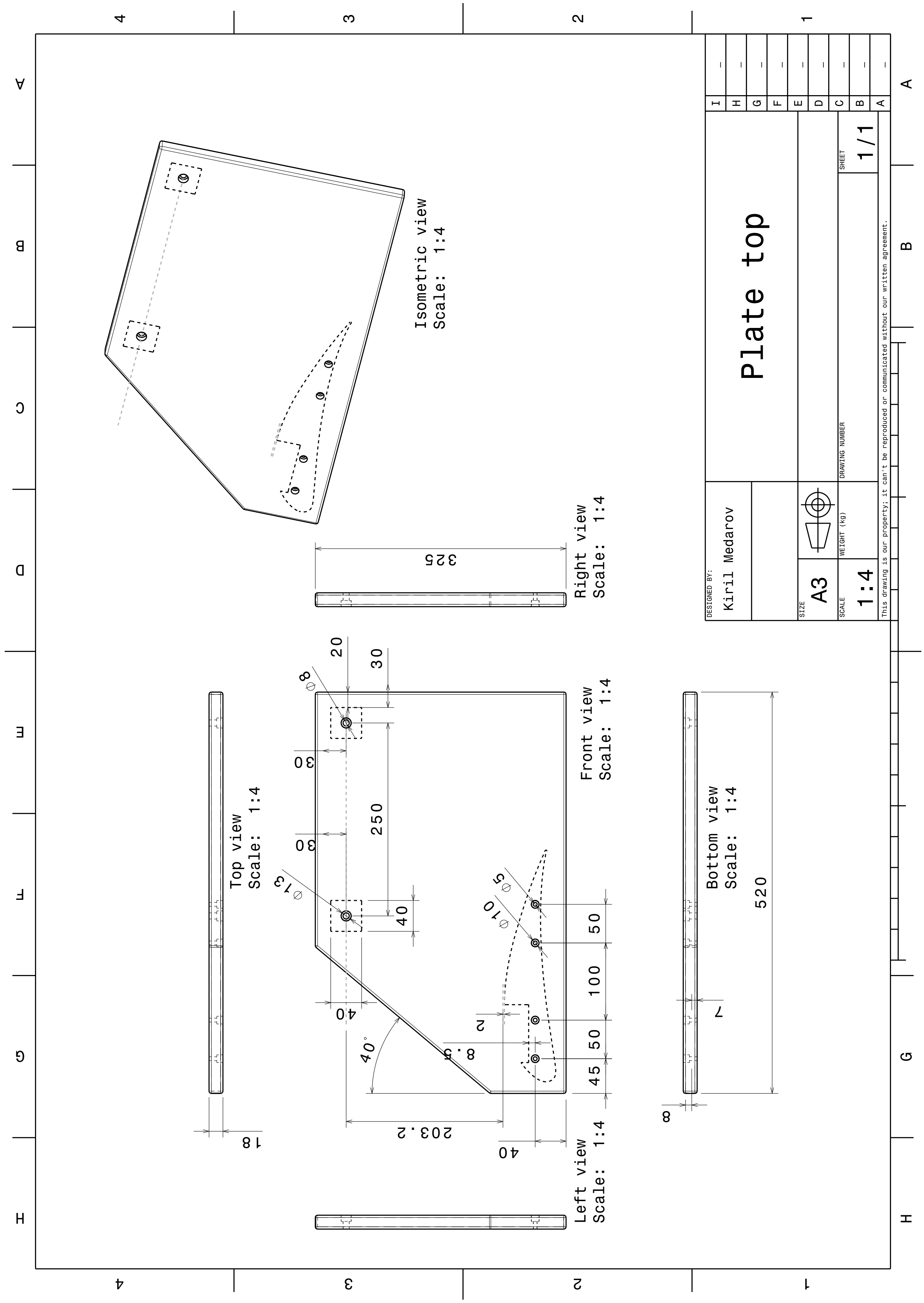

Figure F.9: Technical drawing: Propeller-wing assembly top mounting plate